LIUTEX ANALYSIS BY POD AND DMD IN TURBULENT FLOW

AFTER/ IN MICRO VORTEX GENERATOR

by

Xuan My Trieu

Presented to the Faculty of the Graduate School of

The University of Texas at Arlington in Partial Fulfillment

of the Requirements

for the Degree of

DOCTOR OF PHILOSOPHY

THE UNIVERSITY OF TEXAS AT ARLINGTON

December 2021

Acknowledgments

I would have not been able to achieve my Ph.D. degree without the guidance, patience, motivation, and help of my graduate advisor, Dr. Chaoqun Liu. I feel very fortunate to have such a goodhearted and knowledgeable advisor as Dr. Liu during my time at the University of Texas at Arlington.

Additionally, I want to thank my committee members: Dr. Guojun Liao, Dr. Hristo Kojouharov, and Dr. Wang Li, for their time. I also would like to thank Dr. Jianzhong Su, Dr. Tuncay Aktosun, and Dr. Andrzej Korzeniowski. I am thankful for the financial support from the Math Department as a Graduate Teaching Assistant and as a GAANN Fellow. Furthermore, I would like to express my gratefulness toward Dr. Jianming Liu, Dr. Yisheng Gao and Dr. Ronald Schailey. I am also grateful for my friends at UTA whom I spent much time studying and learning with.

Moreover, I would like to express my deep gratitude to Huong Truong, Hien Truc Trac, Leonard Lao, for their unconditional love, sacrifice, and care throughout so many years. Finally, achieving my goal would have been impossible without my lovely husband's, Vi Duy Tran, encouragement, understanding, and support during my Ph.D. program. And finally, thanks to my wonderful children, Stella Mai Tran and Ryan Huy Tran, who are my motivation to overcome all problems in life.

December 3, 2021

Table of Contents

List of Illustrations

List of Tables

Abstract

LIUTEX ANALYSIS BY POD AND DMD IN TURBULENT FLOW
AFTER/ IN MICRO VORTEX GENERATOR

Xuan My Trieu, Ph.D.

The University of Texas at Arlington, 2021

Supervising Professor: Chaoqun Liu

Although vortex has been studied more than one hundred year, we still have not had universally accepted definition. A few well-known vortex identification methods are introduced Q, Δ, λ_2, λ_{ci} criteria to identify coherent vortex structures the last three decades. A new Omega vortex identification method, which is defined as a ratio of the vorticity tensor norm squared over the sum of the vorticity tensor norm squared and deformation norm squared, was proposed in 2016. Two year later, the new vortex vector named Liutex (previously called Rotex) was proposed by Liu et al. with direction of local rotation axis (an eigenvector of velocity gradient tensor) and angular speed (magnitude of Liutex vector) while other identification methods could not give direction of rotation axis.

Micro-Vortex Generator (MVG) is a common device for turbulent flow separation control. In this paper, in order to better understand the mechanism of flow control by MVG, the flow data set obtained by an implicit implemented large eddy simulation (ILES) with fifth order WENO spatial discretization at $\mathrm{Ma} = 2.5$ and $\mathrm{Re}_\theta = 5760$ is analyzed in details by a proper orthogonal decomposition (POD) method.

In this dissertation, the POD method with 120 snapshots using both velocity (u, v, w) and Liutex vector $(L_x,\ L_y,\ L_z)$ directly as inputs is applied to analyze the vortex structure behind MVG. From the present study, the first a few POD modes are suitable for the explanation of the vortex structures after MVG. In addition, for the first time, the data loaded directly from Liutex vector instead of velocity are organized as the snapshot matrix and a correlation between the absolute strength of rotation (Liutex) and the cumulative rotation strength (Liutex magnitude) of rotation is discovered. The present result clearly shows the POD modes paring, which is a typical sign of Kevin- Helmholtz (K-H) instability. Furthermore, the mechanism of vortex ring generation caused by the K-H type instability is also presented.

Chapter 1
Introduction

Vortex exists everywhere in nature, but there is not yet a generally accepted definition for vortex. After the concept of vorticity filament was proposed by Helmholtz in 1858 [1], some people misunderstood the concept of vorticity and vortex. They believed that vortex is a vorticity tube and vorticity could be used to calculate the vortex's rotation. It is easy to find a counter example to confute such idea. Vorticity is different than zero in laminar flow, but there is no rotational motion because of dominant shear part. Therefore, vorticity cannot be used to calculate the rotation of a vortex and vortex is not vorticity tube. In their study about vorticity, Liu and his researchers found that vorticity includes a rotational part named Rotex/Liutex and a non-rotational part named anti-symmetric shear (S), namely $\omega = \nabla \times \mathrm{V} = \mathrm{R} + \mathrm{S}$ [2, 3]. Moreover, they defined vorticity gradient tensor by two parts: a rotational part (R) and a non-rotational part (NR), which is defined by $\nabla \mathrm{V} = \mathrm{R} + \mathrm{NR}$ [3]. $Q, \Delta, \lambda_2, \lambda_{ci}$ criteria are a few well-known vortex identification methods to identify coherent vortex structure, which have been developed during the last three decades. Liu and his researchers are members of the Vortex and Turbulence Research Team at University of Texas at Arlington, which focused on the expansion of a new generation of vortex identification method since 2014. As a result of their meticulous efforts, a new vortex identification method called Omega (Ω) announced by Liu et.al [4] in 2016.

Modified normalized Rortex/vortex identification method, $\tilde{\Omega}_R$ was proposed by Liu and Liu [5] to improve and solve bulging phenomenon on iso-surfaces of the normalized Rortex/vortex identification method (Ω_R) by Dong et al. [6]. Furthermore, $\tilde{\Omega}_R$ still maintained all advantages of the original Ω_R method. First, in the other vortex identification methods, we have to pick different threshold for each time step to properly capture vortex structure; on the other

hand, $\tilde{\Omega}_R = 0.52$ is quite robust to clearly visualize the vortex structures. Second, $\tilde{\Omega}_R$ is a normalized function with a range of 0 to 1, which is useful to do the correlation analysis in statistics. Third, $\tilde{\Omega}_R$ can capture both strong and weak vortices simultaneously. However, all of the second generation of vortex identification methods described above such as $Q, \Delta, \lambda_2, \lambda_{ci}$ criteria are scalar-based, strongly threshold-dependent and contaminated by shear.

Liutex (previously called Rortex) was proposed by Liu et al. [2] to present the local rigid rotational part (scalar, vector and tensor form) without shear contamination. Liutex is a novel mathematical vector definition pioneering the representation of the absolute rigid rotational strength of the fluid motion in vortex science and defined as $\vec{\mathrm{R}} = \mathrm{R}\vec{\mathrm{r}}$, where R is magnitude of Liutex vector (the rigid body angular speed) and $\vec{\mathrm{r}}$ is an eigenvector of velocity gradient tensor (local rotation axis) [7]. Wang et al. [8] derived an explicit formula to calculate the magnitude of Liutex:

$$\mathrm{R} = \vec{\omega} \cdot \vec{\mathrm{r}} - \sqrt{(\vec{\omega} \cdot \vec{\mathrm{r}})^2 - 4\lambda_{\mathrm{ci}}^2},$$

where $\vec{\omega}$ is the local vorticity vector, $\vec{r}$ a real eigenvector of velocity gradient tensor (local rotation axis), λ_{ci} an imaginary part of the complex eigenvalue of velocity gradient tensor, $\vec{\omega} \cdot \vec{\mathrm{r}}$ the magnitude of vorticity projected in the direction of $\vec{\mathrm{r}}$.

Kelvin-Helmholtz instability (KHI) originally studied by Hermann von Helmholtz in 1868 and Lord Kelvin in 1871. KHI is an instability at the interface between two parallel streams with different velocities and densities, but they are discontinuous at the interface between two fluids with the heavier fluid at the bottom and the lighter fluid at the top. We can easily find the KHI every place in the nature such as the wind blowing over water, motion of interstellar clouds and quantized vortices in quantum fluids.

Micro vortex generator (MVG) is a low-passive control device commonly used in aviation applications such as reducing drag, alleviating separation in turbulent flow, enhancing the quality of the velocity profile after shock wave and boundary layer interaction (SWBLI), etc. [9]. The other benefits of MVG include simple design, easy implementation, low cost and robust performance. Therefore, aerospace engineering researchers are interested in micro vortex generators (MVGs) hoping to alleviate the harmful effects by SWBLI.

Lumley introduced the proper orthogonal decomposition (POD) to study turbulent flow field in 1967 [10]. The POD was proposed independently by Kosambi (1943), Loeve (1945), Karhunen (1946), Pougachev (1953), and Obukhov (1954) (See Berkooz et al. in 1993 [11]). Proper orthogonal decomposition (POD), which is also known as the Karhunen-Loeve decomposition (KLD) [12], principal component analysis (PCA) after restricting to finite dimensions and truncating a few terms later [13], and the Hotelling transform [14]. The main goals of POD method are a common and efficient reduction by projecting the high dimensional space into the lower one and extraction by exposing appropriated structure hidden in data [15]. POD is also considered a great model of continuous second order processes. After applying the POD method, the user can keep the first few POD modes, which contain the most energy to analyze the data. Powerful computers were required for finding POD modes; thus, the POD method became popular only in the middle of 20^{th} century after the necessary computing power became more affordable. There are various applications of the POD method such as: image processing, signal analysis, data compression, modal analysis and modal order reduction. Liang et al. [16] summarized the POD method, proved the equivalent and showed the connection of three POD methods: KLD, PCA and singular value decomposition (SVD) in 2001. Wu et al. [17] explained that

there are two interpretations of POD. The first interpretation regards POD as the Karhunen-Loeve Decomposition (KLD). The second interpretation consists of the following three closely connected methods; KLD, the principal component analysis (PCA), and the singular value decomposition (SVD). In their research, the authors did apply some useful theorems to provide detailed proofs that both KLD and SVD are equivalent to PCA; and that the POD method is equivalent to all three methods (KLD, SVD, PCA). In article [18], Taira et al. did a great model analysis of the POD method in 2017. In their study, the application of POD to complex flow field was discussed using three related key approaches: the spatial POD method, the snapshot POD method and the SVD. Their research mentioned the advantages of POD including easy computation in both spatial and snapshot methods and elimination from the data of noise, which usually manifests as high-order POD modes. POD was used in the research of Kerschen et al. [19] for discovering several different useful applications that are beneficial in structural dynamics and ordering not only linear but also nonlinear systems reduction. On the other hand, Brevis et al. [20], for the flow visualization image pre-processing and post-processing, used POD to analyze coherent structures. In their study, the cost of POD in two-dimensional shallow flow in a cylinder is not very high and the characterization of coherent structure is not excessively complicated. A highly cited study of POD applied to internal combustion (IC) engine flows was done by Chen et al. [21] in 2012. The research explained clearly that the properties of POD and suggested some useful application for IC engine flows. Instead of using several POD modes to analyze the data, the authors only utilized mode 1 to accurately approximate the ensemble average and to determine the cyclic changes in Reynolds-averaged Navier–Stokes ensemble average. Richer and his research group also used POD method to examine the wake-dynamic coherence vortex structure of circular cylinder in

2018 [22]. In their study, the first six POD modes were used to study dynamic systems. Three pairs of POD modes were found in the paper. The slow-drift effect faintly modulated the first pair of POD modes. Besides, they also proposed the important model with a substantial influence on Reynolds stress to show how energy is transferred among different POD modes. The experimental study differences between streaky and non-streaky activities in overloaded channel flow with micro-bubbles using POD method was completed by Zhao, et at. [23] in 2019. The authors found that there was a significant strengthening of non-streaky turbulence and a decline of streaky ones. The other main purpose of applying POD method was to examine kinetic energy and analyze the coherent streak structure in turbulent flow field.

Schmid et al. introduced the dynamic mode decomposition (DMD) by using numerical and experimental data to extract dynamic mode and in 2010 [24]. He did determine the method on various flows such as: plane channel flow, on two-dimensional cavity flow, from wake flow behind a flexible membrane to the jet passing through two cylinder's flow. The primary goal of DMD in this study was used as the dimensional reduction method. He also proved DMD was a robust and consistent method. The utility of dynamic mode decomposition in Abu and Hyung' research is to analyze self-sustained oscillations in turbulent cavity flow at $Re_D = 3000\ and\ 12000$, with upstream turbulent of $Re_\theta = 670\ and\ 300$, respectively in 2011[25]. In the study, DMD algorithm was used to extract the wide range of structures. The viscous boundary layer was denoted by the thick incoming boundary layer structures while the cavity dynamics were represented by the thin incoming boundary layer which showed a leading peak in the spectrum. Number of scientists who are interesting in studying coherent structure is increasing in the recent decade. They tried to understand the complex and multi-scaled nature of turbulent

flows. Jorn Sesterhenn and Amir Shahirpour are a great example. They introduced the characteristic dynamic mode decomposition to approximate coherent structures with a reduced order model in space and time which included three topics: coherent structure, model, decomposition, and model reduction in 2019 [26].

After Babinsky et al. [27] conducted experiments on several different kind of microamps at Mach 2.5 in 2009, many scholars believed that the velocity profiles were getting fuller expressively as shown in figure 3 and boundary-layer thickness was reduced in comparison to the case with no microamps, which made the flow harder to be separated after putting MVG. The result of this study was confirmed by several researchers such as the Ghosh et al. [28] in 2010, Lee et al. [29] in 2012 and Wang et al. [30] in 2012.

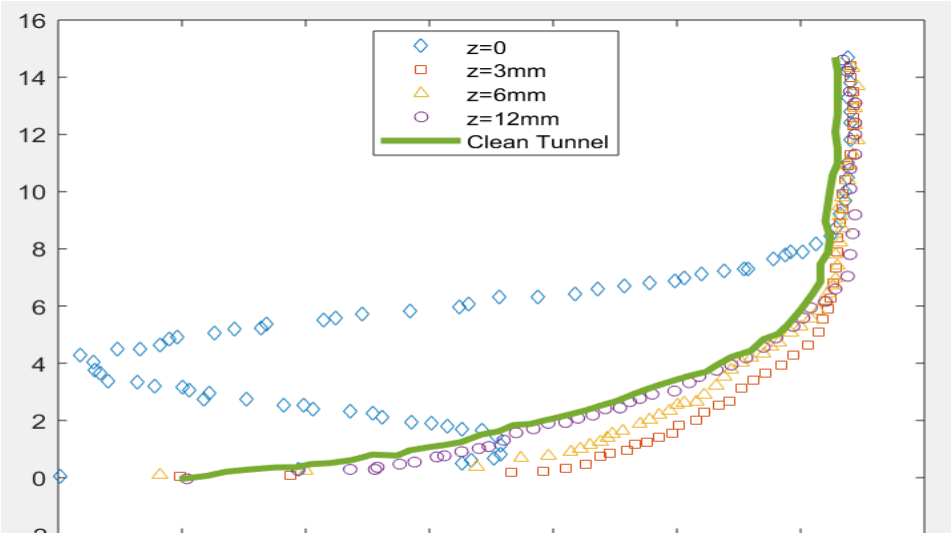

Figure 2. 1 Average velocity profile from Babinsky et al. [18]

However, the numerical simulation results for supersonic micro vortex generator at $Ma = 2.5$ and $Re_\theta = 1440$ of Li and Liu [31] revealed a quite new mechanism to compare with Babinsky's experimental result in 2011 [32]. Their first conclusion is that momentum deficit on streamwise direction behind MVG brought low-momentum from the bottom fluid up to the top

and high-momentum from the top descended to the bottom. Moreover, low and high-momentum went opposite direction which generated shear layer instability (K-H type instability). Then, shear layer formed K-H rings, which destroy the shock and reduce the separation bubble size. Their second conclusion is that the mechanism of vortex ring generation should be K-H type instability. A year later, Lu et al. [33] confirmed their conclusions through their MVG on high-speed flow experiment. Yan et al. [34, 35] also acknowledged that the mechanism of vortex ring generation should be K-H type instability. In several studies of Sun et al. about MVG [36], their results are also supporting Li and Liu theories.

The purpose of this research is to further check if the theory, that the vortex structure behind MVG is generated by K-H type instability, is correct or not. Moreover, POD method is applied to compare the results from loading data directly from Liutex vector (L_x, L_y, L_z) and loading from velocity (u, v, w) by using $\tilde{\Omega}_R$ method and Liutex iso-surface. Besides, DMD method is also used to analyze on the mechanism of separation reduction by MVG through shock vortex interaction by loading data directly from Liutex vector (L_x, L_y, L_z).

The dissertation is arranged as follows. Case set up and code validation are introduced in chapter 2. Chapter 3 provides vortex identification methods such as: Q, Δ, λ_{ci} criterion, λ_2 criterion, Omega, Liutex. Chapter 4 is mainly discussion on POD analysis of coherent structure in turbulent flow after MVG and coherent structure in the wake of MVG. DMD is described in chapter 5. The conclusions are made in the last section.

Chapter 2
Case Description and Code Validation

2.1 Governing equation

The data of flow field is obtained by an implicit implemented large eddy simulation. The governing equations are the nondimensional compressible Navier-Stokes equations in conservative form which read

$$\frac{\partial \vec{Q}}{\partial t}+\frac{\partial \vec{E}}{\partial x}+\frac{\partial \vec{F}}{\partial y}+\frac{\partial \vec{G}}{\partial z}=\frac{\partial \vec{E}_v}{\partial x}+\frac{\partial \vec{F}_v}{\partial y}+\frac{\partial \vec{G}_v}{\partial z} \tag{25}$$

where

$$\vec{Q}=\begin{bmatrix}\rho\\ \rho u\\ \rho v\\ \rho w\\ e\end{bmatrix}, \vec{E}=\begin{bmatrix}\rho u\\ \rho u^2+p\\ \rho uv\\ \rho uw\\ (e+p)u\end{bmatrix}, \vec{F}=\begin{bmatrix}\rho v\\ \rho vu\\ \rho v^2+p\\ \rho vw\\ (e+p)v\end{bmatrix}, \vec{F}=\begin{bmatrix}\rho w\\ \rho wu\\ \rho wv\\ \rho w^2+p\\ (e+p)w\end{bmatrix},$$

$$\vec{E}_v=\frac{1}{Re}\begin{bmatrix}0\\ \tau_{xx}\\ \tau_{xy}\\ \tau_{xz}\\ u\tau_{xx}+v\tau_{xy}+w\tau_{xz}+q_x\end{bmatrix}, \vec{F}_v=\frac{1}{Re}\begin{bmatrix}0\\ \tau_{yx}\\ \tau_{yy}\\ \tau_{yz}\\ u\tau_{yx}+v\tau_{yy}+w\tau_{yz}+q_y\end{bmatrix},$$

$$\vec{G}_v=\frac{1}{Re}\begin{bmatrix}0\\ \tau_{zx}\\ \tau_{zy}\\ \tau_{zz}\\ u\tau_{zx}+v\tau_{zy}+w\tau_{zz}+q_z\end{bmatrix},$$

$e=\frac{p}{\gamma-1}+\frac{1}{2}\rho(u^2+v^2+w^2), q_x=\frac{\mu}{(\gamma-1)M_\infty^2 Pr}\frac{\partial T}{\partial x}, q_y=\frac{\mu}{(\gamma-1)M_\infty^2 Pr}\frac{\partial T}{\partial y}, q_z=\frac{\mu}{(\gamma-1)M_\infty^2 Pr}\frac{\partial T}{\partial z}, p=\frac{1}{\gamma M_\infty^2}\rho T, Pr=0.72,$

$$\tau = \mu\begin{bmatrix} \frac{4}{3}\frac{\partial u}{\partial x} - \frac{2}{3}\left(\frac{\partial v}{\partial y} + \frac{\partial w}{\partial z}\right) & \frac{\partial u}{\partial y} + \frac{\partial v}{\partial x} & \frac{\partial u}{\partial z} + \frac{\partial w}{\partial x} \\ \frac{\partial u}{\partial y} + \frac{\partial v}{\partial x} & \frac{4}{3}\frac{\partial v}{\partial y} - \frac{2}{3}\left(\frac{\partial u}{\partial x} + \frac{\partial w}{\partial z}\right) & \frac{\partial v}{\partial z} + \frac{\partial w}{\partial y} \\ \frac{\partial u}{\partial z} + \frac{\partial w}{\partial x} & \frac{\partial v}{\partial z} + \frac{\partial w}{\partial y} & \frac{4}{3}\frac{\partial w}{\partial z} - \frac{2}{3}\left(\frac{\partial u}{\partial x} + \frac{\partial v}{\partial y}\right) \end{bmatrix}. \quad (26)$$

The viscous coefficient is calculated by Sutherland's law:

$$\mu = T^{3/2}\frac{1+C}{T+C},\ C = \frac{110.4}{T_\infty}. \quad (27)$$

The nondimensionalization of variables is given as follows:

$$x = \frac{\tilde{x}}{L},\ y = \frac{\tilde{y}}{L},\ z = \frac{\tilde{z}}{L},\ u = \frac{\tilde{u}}{U_\infty},\ v = \frac{\tilde{v}}{V_\infty},\ w = \frac{\tilde{w}}{W_\infty},\ T = \frac{\tilde{T}}{T_\infty},\ \mu = \frac{\tilde{\mu}}{\mu_\infty},\ k = \frac{\tilde{k}}{k_\infty},\ \rho = \frac{\tilde{\rho}}{\rho_\infty},\ p = \frac{\tilde{p}}{\rho_\infty U_\infty^2} \quad (28)$$

where the variables with the symbol "∼" represents the dimensional version.

Using the following coordinate transformation,

$$\xi = \xi(x, y, z),$$

$$\eta = \eta(x, y, z),$$

$$\zeta = \zeta(x, y, z),$$

the governing equations are transformed to the equations in the computational space as

$$\frac{\partial \vec{\hat{Q}}}{\partial t} + \frac{\partial \vec{\hat{E}}}{\partial x} + \frac{\partial \vec{\hat{F}}}{\partial y} + \frac{\partial \vec{\hat{G}}}{\partial z} = \frac{\partial \vec{\hat{E}}_v}{\partial x} + \frac{\partial \vec{\hat{F}}_v}{\partial y} + \frac{\partial \vec{\hat{G}}_v}{\partial z}$$

where

$$\vec{\hat{Q}} = J^{-1},$$

$$\vec{\hat{E}} = J^{-1}\left(\xi_x \vec{E} + \xi_y \vec{F} + \xi_z \vec{G}\right),$$

$$\vec{\hat{F}} = J^{-1}\left(\eta_x \vec{E} + \eta_y \vec{F} + \eta_z \vec{G}\right),$$

$$\vec{\hat{G}} = J^{-1}\left(\zeta_x \vec{E} + \zeta_y \vec{F} + \zeta_z \vec{G}\right),$$

$$\vec{\hat{E}}_v = J^{-1}\left(\xi_x \vec{E}_v + \xi_y \vec{F}_v + \xi_z \vec{G}_v\right),$$

$$\vec{\hat{F}}_v = J^{-1}\left(\eta_x \vec{E}_v + \eta_y \vec{F}_v + \eta_z \vec{G}_v\right),$$

$$\vec{\hat{G}}_v = J^{-1}\left(\zeta_x \vec{E}_v + \zeta_y \vec{F}_v + \zeta_z \vec{G}_v\right),$$

$$J^{-1} = \frac{\partial x}{\partial \xi}\frac{\partial y}{\partial \eta}\frac{\partial z}{\partial \zeta} + \frac{\partial x}{\partial \eta}\frac{\partial y}{\partial \zeta}\frac{\partial z}{\partial \xi} + \frac{\partial x}{\partial \zeta}\frac{\partial y}{\partial \xi}\frac{\partial z}{\partial \eta} - \frac{\partial x}{\partial \xi}\frac{\partial y}{\partial \zeta}\frac{\partial z}{\partial \eta} - \frac{\partial x}{\partial \eta}\frac{\partial y}{\partial \xi}\frac{\partial z}{\partial \zeta} - \frac{\partial x}{\partial \zeta}\frac{\partial y}{\partial \eta}\frac{\partial z}{\partial \xi}$$

2.2 Numerical Methods

We use the fifth order bandwidth-optimized WENO scheme and the implicitly LES method to solve the form of the Navier-Stokes equations at Mach=2.5 and $Re = 5760$.

One dimensional hyperbolic equation can be written as:

$$\frac{\partial u}{\partial t} + \frac{\partial f(u)}{x} = 0,$$

The semi-discretized equation can be written as:

$$\left(\frac{\partial u}{\partial t}\right)_j = -\frac{h_{j+\frac{1}{2}}}{\Delta x} + \frac{h_{j-\frac{1}{2}}}{\Delta x}$$

$$h_1^{+\prime} = \frac{1}{3} f_{j-2} - \frac{7}{6} f_{j-1} + \frac{11}{6} f_j,$$

$$h_2^{+\prime} = -\frac{1}{6}f_{j-1} + \frac{1}{3}f_j + \frac{5}{6}f_{j+1},$$

$$h_3^{+\prime} = \frac{1}{3}f_j + \frac{5}{6}f_{j+1} - \frac{1}{6}f_{j+2}$$

Where the superscript "+" is the positive flux after flux splitting,

The final non-linear weight scheme is:

$$h_{j+\frac{1}{2}}^{+} = w_1 h_1^{+\prime} + w_2 h_2^{+\prime} + w_3 h_3^{+\prime},$$

Where w_i: the WENO weights, IS_i: the smoothness indicators

$$w_i = \frac{b_i}{b_1 + b_2 + b_3}, b_i = \frac{a_i}{(IS_i + \varepsilon)^2}, (a_1, a_2, a_3) = (0.1, 0.6, 0.3),$$

$$IS_1 = \frac{13}{12}(f_{j-2} - 2f_{j-1} + f_j)^2 + \frac{1}{4}(f_{j-2} - 4f_{j-1} + 3f_j)^2,$$

$$IS_2 = \frac{13}{12}(f_{j-1} - 2f_j + f_{j+1})^2 + \frac{1}{4}(f_{j-1} - 4f_{j+1})^2,$$

$$IS_3 = \frac{13}{12}(f_j - 2f_{j+1} + f_{j+2})^2 + \frac{1}{4}(3f_j - 4f_{j+1} + f_{j+2})^2.$$

The scheme for the negative flux $h_{j+\frac{1}{2}}^{-}$ has the similar form to $h_{j+\frac{1}{2}}^{+}$ at point $x_{j+\frac{1}{2}}$.

For spatial discretization, the fifth-order bandwidth-optimized WENO scheme is used for the convective terms and the traditional fourth-order central scheme is utilized for the viscous terms. The explicit third-order TVD type Runge-Kutta scheme is adopted for the time integration. In the wall boundary, the adiabatic, zero-gradient of pressure and nonslipping condition is enforced. In the upper boundary, fixed-value condition with the free parameters is used. The

mirror-symmetry condition is used in the spanwise direction. The outflow boundary condition is specified as a kind of characteristic-based condition.

$$u^{(1)} = u^n + \Delta t L(u^n),$$

$$u^{(2)} = \frac{3}{4}u^n + \frac{1}{4}u^{(1)} + \frac{1}{4}\Delta t L\left(u^{(1)}\right),$$

$$u^{n+1} = \frac{3}{4}u^n + \frac{1}{4}u^{(2)} + \frac{2}{3}\Delta t L\left(u^{(2)}\right),$$

Where L is the differential operator which denotes the spatial derivatives,

$$L(u) = -\frac{\partial E(u)}{\partial x} - \frac{\partial F(u)}{\partial y} - \frac{\partial G(u)}{\partial z} + \frac{\partial E_v(u)}{\partial x} + \frac{\partial F_v(u)}{\partial y} + \frac{\partial G_v(u)}{\partial z}.$$

2.3 Case setup and code validation

The geometry of MVG is shown in figure 2.1 and the geometric parameters are specified following the experimental research performed by Babinsky et al. [27], with $h = 4, c = 7.2h, \alpha = 24^{\circ}, s = 7.5h$, where h is the height of MVG, c is the chord length and s is the distance between MVG. In this study $z = 0$ is the corner. Furthermore, the trailing edge declining angle 70° is con sidered to control the flow. For the mechanism of the vortex ring generation, a micro vortex generator at $Ma = 2.5$ and $Re_{\theta} = 5760$ is used. To solve the Navier-Stokes equations, in this research a large eddy simulation method with fifth order bandwidth-optimized WENO scheme [32] is applied. Figure 2.2 shows the schematic of a half grid system which is divided by three regions: fore-region, MVG region and ramp region. For the high resolution and the smooth transformation, there is a grid transition buffer lying between the two regions. Because the grid distribution is symmetric, there is only half of the gird system displayed. The grid system

$n_{streamwise} \times n_{spanwise} \times n_{normal} = 1600 \times 192 \times 137$ is chosen to be the grid of the system and $x, y\ and\ z$ be the spanwise, normal and streamwise direction respectively. In the wake region, uniform mesh is used along the streamwise and spanwise directions and non-uniform mesh is used along the normal direction. The grid and the geometry generation detailed explanation is in the previous researches [31, 37], so that they are not mentioned in this paper.

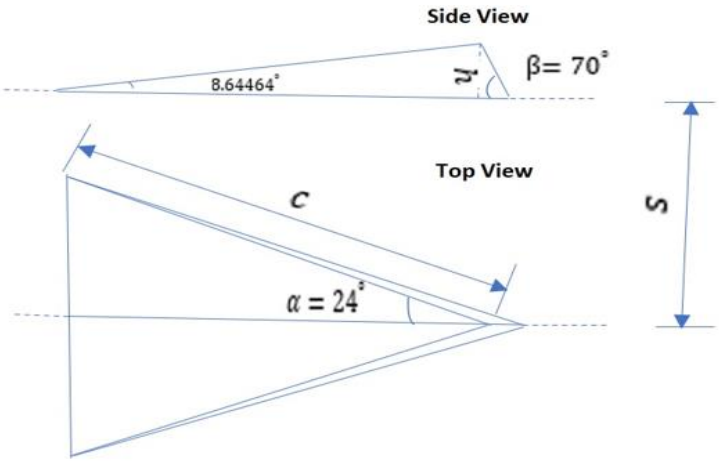

Figure 2. 2 The geometry of micro vortex generator

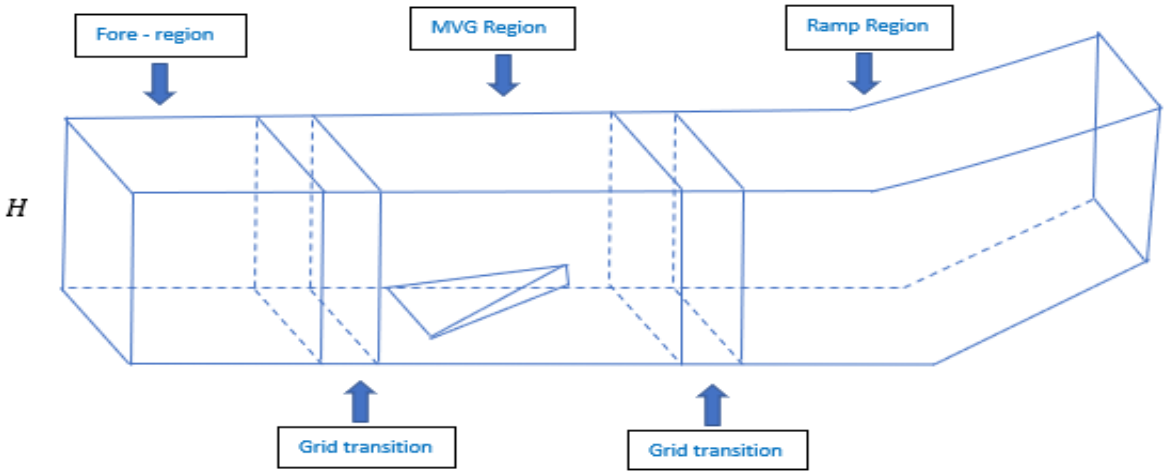

Figure 2. 3 The schematic of the half grid system

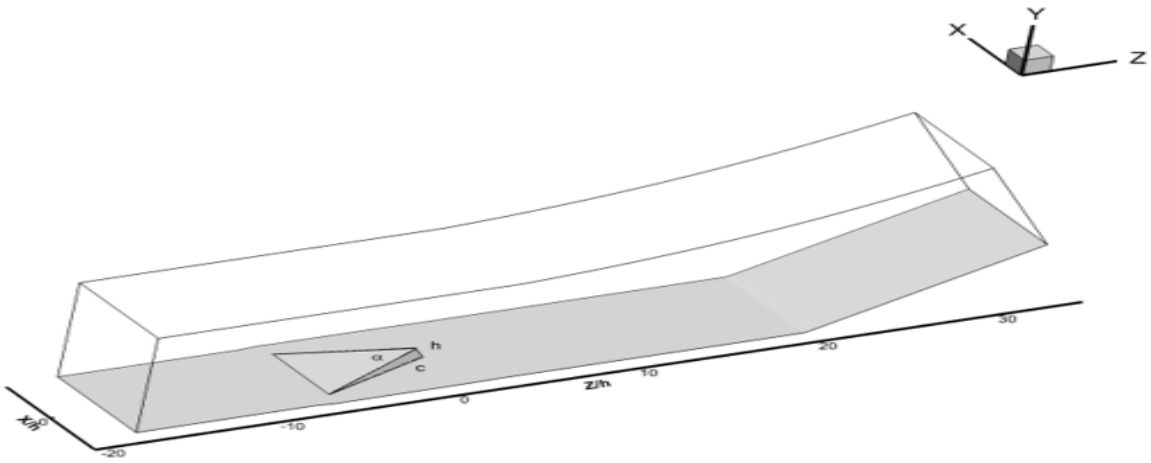

Figure 2.4 The configuration of the computational domain

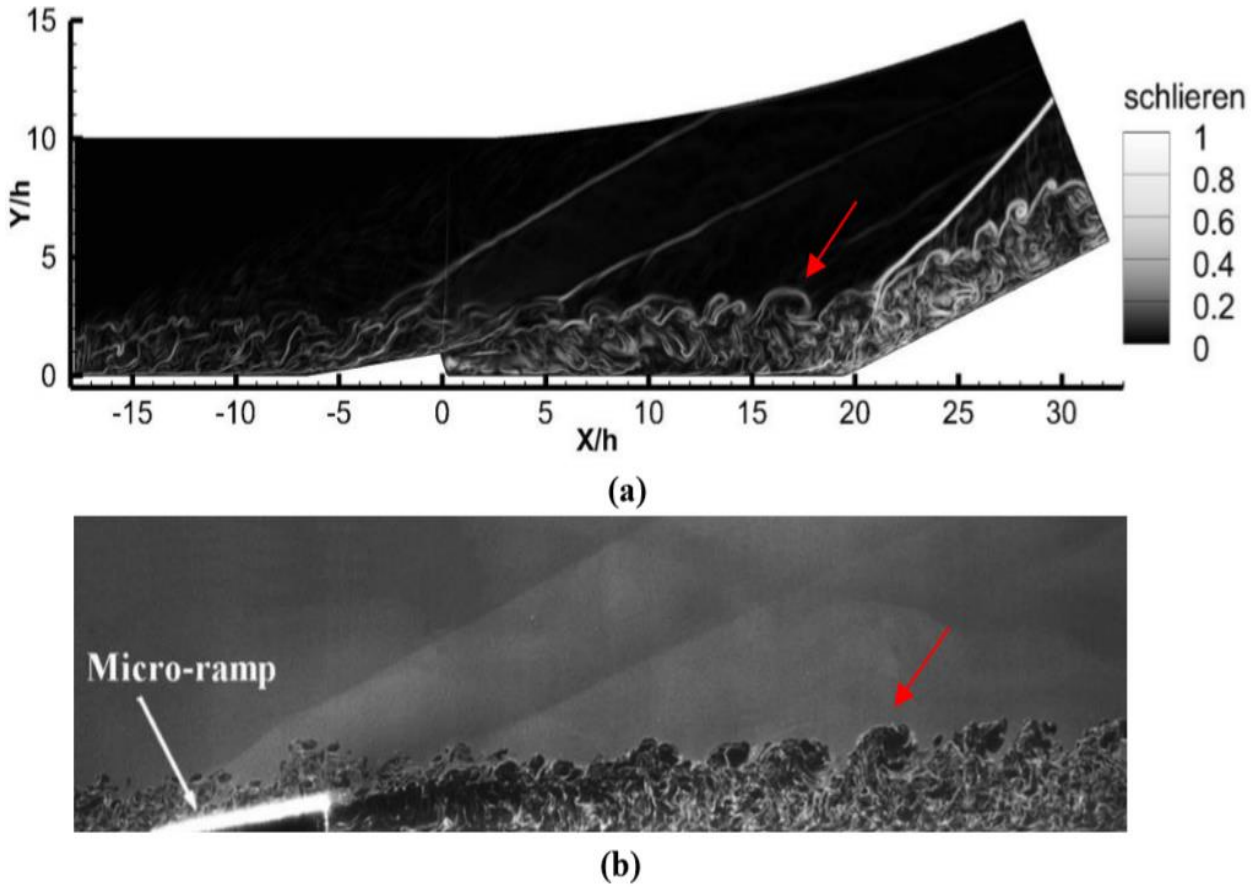

Figure 2. 5 Wake vortices structure behind MVG (a) the schlieren on the central plane given by our LES result (b) the NPLS image of Wang et al. [38]

The group of researchers at University of Texas at Arlington developed the LESUTA code to adopt in this study. The schlieren of turbulent compression ramp flow with MVG on the central plane depend on the LES result is showed in figure below. Wang et al [38] proposed the NPLS image of wake structures behind MVG in 2012 that shows in figure 2.4 NPLS suggests a new flow visualization bases on Rayleigh-scattering which contained from the supersonic flow at $Ma = 2.7$ and $Re_\theta = 5845$.

Table 2. 1 Initial and reference parameters of the turbulent flow

M_∞	Re_θ	T_∞	T_w	h	δ	U_∞	T
2.5	5760	288.15 K	300 K	4 mm	9.44 mm	850 m/s	$4.76 \times 10^{-6} s$

The parameters in table 2.1 are defined as:

M_∞= Mach number

Re_θ= Reynolds number based on momentum thickness

T_∞= free stream temperature

T_w= wall temperature

h= height of micro vortex generator

δ= local thickness of the turbulent boundary layer

U_∞= the freestream velocity

2.4 Kelvin-Helmholtz instability

Kelvin-Helmholtz instability was initially researched by Hermann von Helmholtz (1868) and Lord Kelvin (1871) [39]. K-H instability occurs when the high-speed zone (on the top) is descending to the bottom, while the low-speed zone (on the bottom) is ascending. Furthermore, they are going in opposite directions generating the shear layer as shown in figures 2.5 (a) and (b). The shear layer keeps rolling until it forms a pair of rotations as shown in figures 2.5 (c) and

(d). After becoming a pair, that pair of rotations keeps rolling together eventually mixing and becoming one rotation. However, it still has a pair of cores inside the rotation as shown in figures 2.5(e) and (f). Thus, pairing of vortices in two dimensions is the sign of K-H instability. On the other hand, in 3-D the K-H instability resemble rings circling around streamwise and spanwise on streamwise direction as shown in figure 2.6[40]. This instability occurs among others as well in the cloud, on the way of water and on Jupiter.

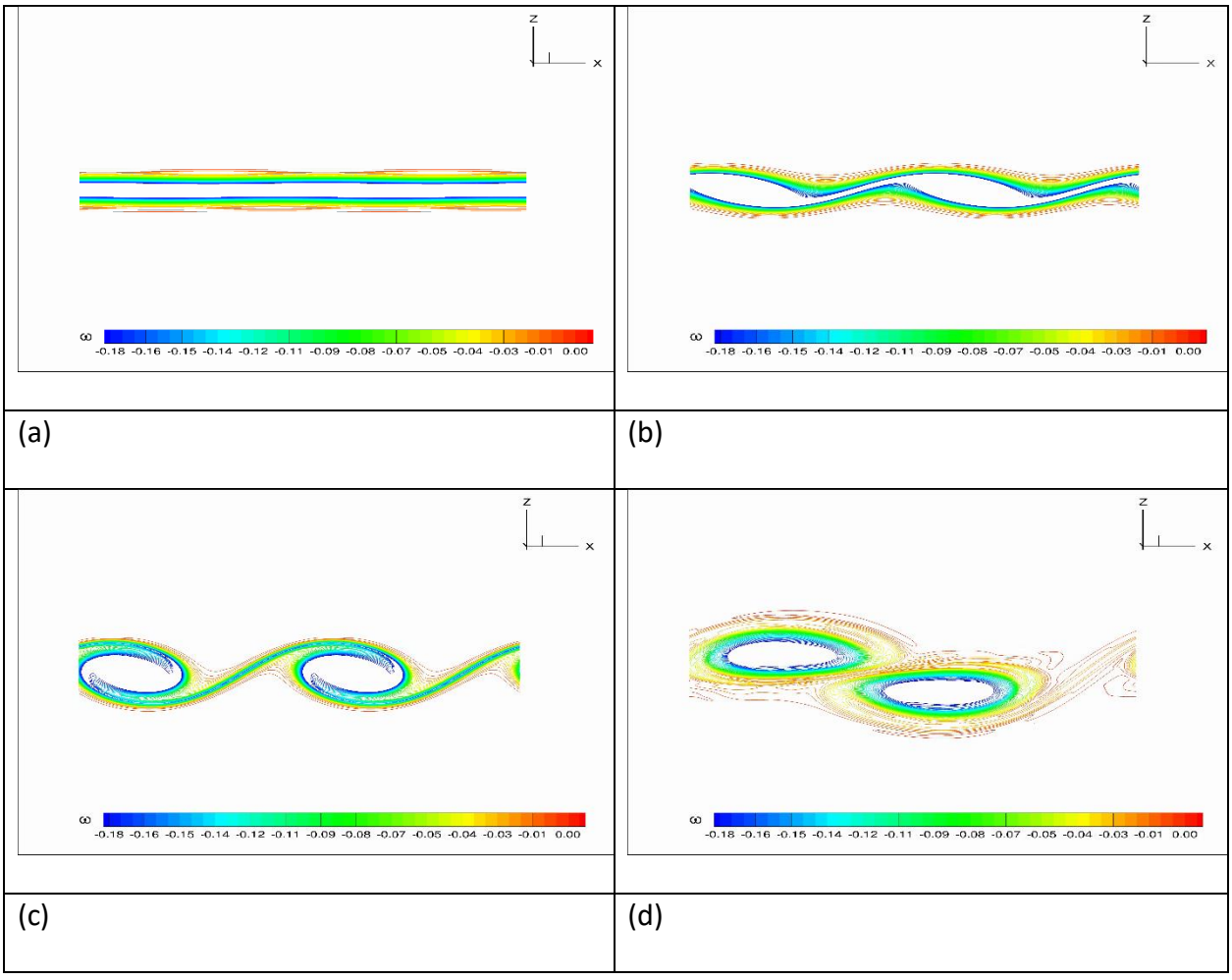

(a) (b)

(c) (d)

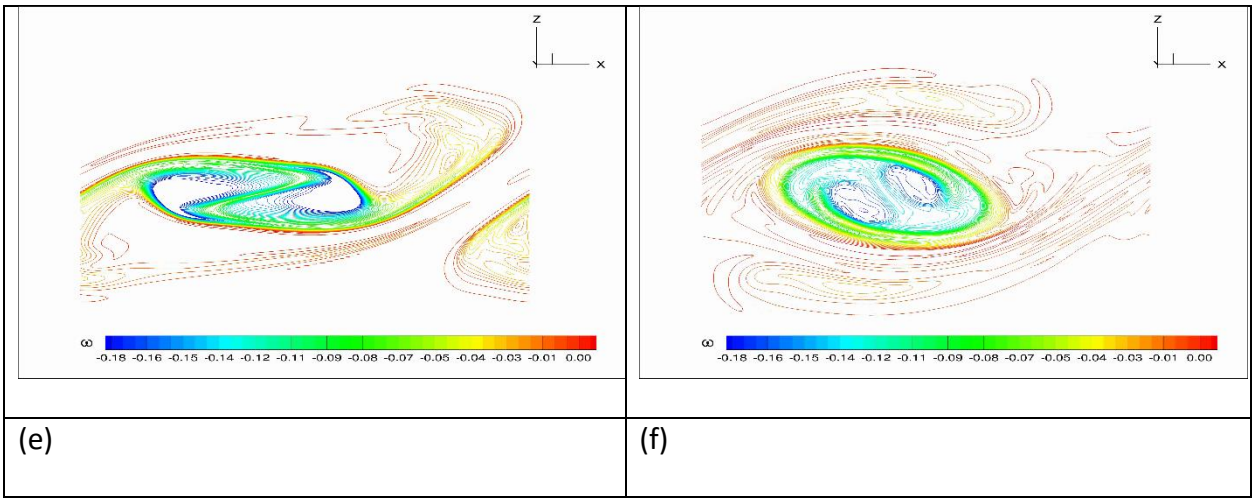

(e) (f)

Figure 2. 6 Numerical simulation in 2 dimensions on K-H instability.

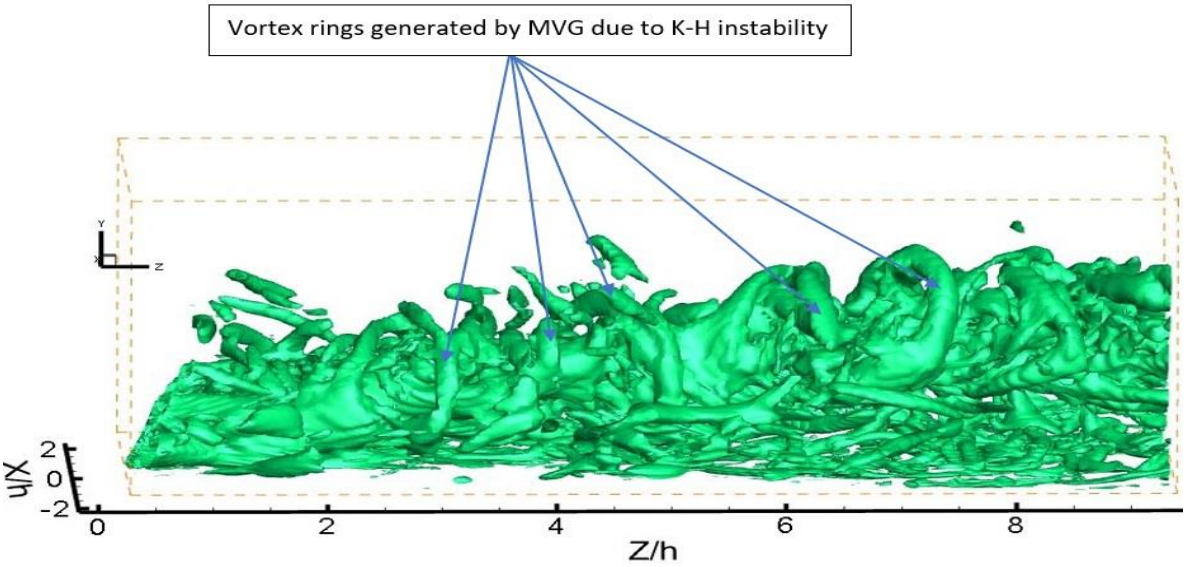

Figure 2. 7 Numerical simulation in 3-D on K-H type instability (iso-surface of $\tilde{\Omega}_R$ = 0.52)

Figure 2. 8 Kelvin-Helmholtz instability occurring on the cloud (source: Wikipedia)

Figure 2. 9 Kelvin-Helmholtz instability occurring on the wave of water (source: Wikipedia)

Figure 2. 10 Kelvin-Helmholtz instability occurring on the Jupiter (source: Wikipedia)

As shown in Figs. 2.10 and 2.11, images of vortex structure in MVG wake subzone show evidently that the head shape of K-H vortices is arc-shaped. It also illustrates that there are vortex rings generated by MVG attributable to K-H type instability. The vorticities are decomposed along the streamwise and spanwise; moreover, Kelvin-Helmholtz vortices lie on the top and circle around streamwise and spanwise vortices along the Z-direction (Z-direction is the streamwise direction). Kelvin-Helmholtz vortices are getting larger downstream than upstream are reflected by the growth of vortex pair spacing which is the same as the result of Sun's studies which is showed in figure 2.12 [36, 40].

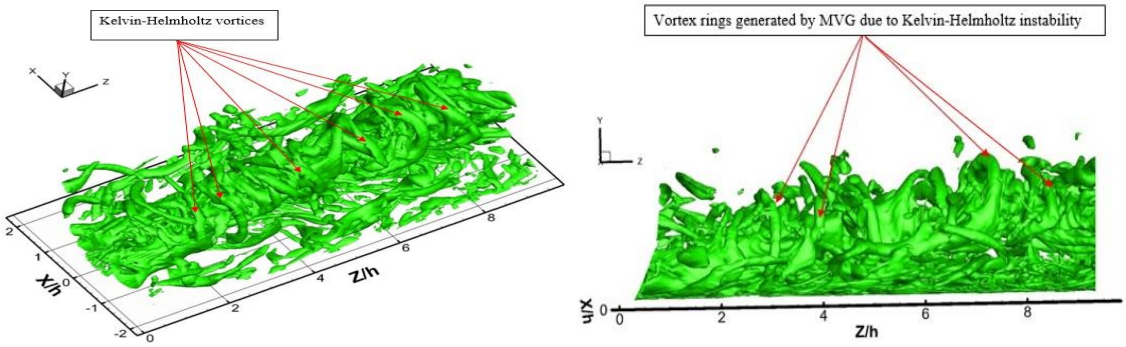

Top View Side view

Figure 2. 11 Subzone of vortex structures (iso-surface of $\tilde{\Omega}_R$ = 0.52) in MVG wake

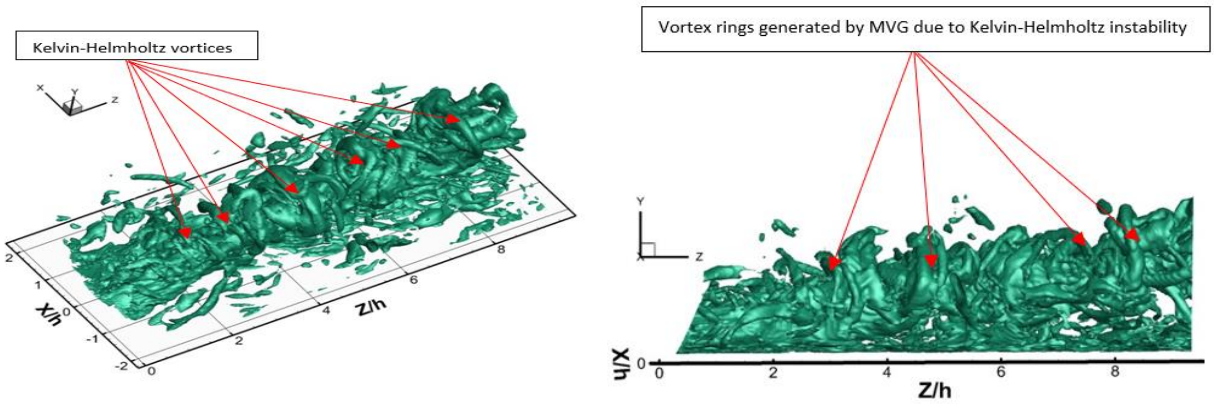

Top view Side view

Figure 2. 12 Subzone of vortex structures (iso-surface of Liutex =0.05) in MVG wake

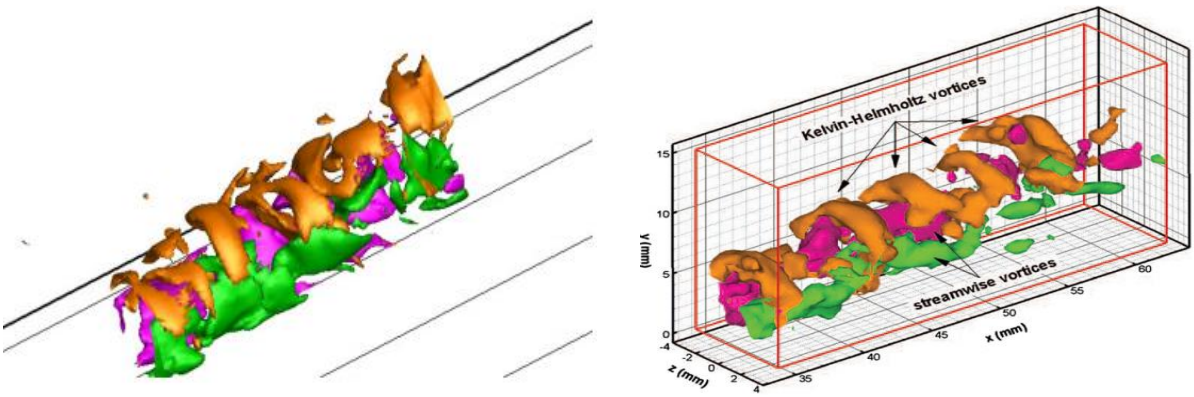

Figure 2. 13 Distribution of streamwise and spanwise vorticity from our LES (left) and from experiment by Sun et al. (right

2.5 Micro vortex generator (MVG)

There were several MVG studies in supersonic flow field advocating MVG as a powerful device to reduce the harmful separation by removing the shock [33, 35]. The original function of MVG was to improve performance of high lift wing flap configurations [33] which is showed in figure 2.13. Indeed, there have been several successful experiments in finding positive effects of applying MVG. Vortex generator (VG) can delay successfully flow separation in aviation applications with a height that is about 10-50% of boundary layer thickness. However, MVG is superior over VG in reducing flow separation in turbulent flow due to untoward pressure gradient [41] and shock-induced separation [42] with a height that is approximately $20 - 40\%$ of the boundary layer thickness. McCormick et al. [43] was the first in making an experimental comparison between MVG and passive cavity in a relatively low speed flow at $Mach\ 1.56 - 1.65\ in\ 1993$. The authors found that MVG is available device, which can suppress SWBLI and improve downstream boundary layer of the shock.

Figure 2. 14 An array of vortex generators on the aircraft wing for shock buffeting control (picture taken on B737-800, operated by Transavia airlines, flying from Barcelona to Amsterdam)

Chapter 3
Vortex Identification Methods

The velocity gradient tensor which is given velocity field v is defined as

$$\mathrm{G} \equiv \nabla v$$

And it can be written by two parts: symmetric and antisymmetric parts

$$G = S + \Omega$$

Where S is called the strain rate tensor,

Ω is called the angular rotation rate tensor,

$$S = \frac{1}{2}[G + G^T]$$

$$\Omega = \frac{1}{2}[G - G^{\mathrm{T}}]$$

The trajectory of the neighboring fluid particle is determined by solving the deferential equation:

$$\frac{dy}{dt} = Gy$$

Given the initial condition $y(0) = y_0$.The solution of this linear system of first-order ordinary differential equations (ODEs) is given by eigen decomposition:

$$GV = V\Lambda = \Lambda V$$

$$G\vec{v} = \lambda\vec{v}$$

$$G = V\Lambda V^{-1}$$

$$\vec{v} = [\overrightarrow{v_1}, \overrightarrow{v_2}, \overrightarrow{v_3}]$$

$$\Lambda = \begin{bmatrix} \lambda_1 & 0 & 0 \\ 0 & \lambda_2 & 0 \\ 0 & 0 & \lambda_3 \end{bmatrix}$$

$$\frac{dy}{dt} = Gy = V\Lambda V^{-1}y$$

$$V^{-1}\frac{dy}{dt} = \Lambda V^{-1}y$$

$$\frac{d(V^{-1}y)}{dt} = \Lambda(V^{-1}y)$$

$$\bar{y} = V^{-1}y$$

$$=> y = \bar{y}V$$

$$\frac{d\bar{y}}{dt} = \Lambda y = \begin{bmatrix} \lambda_1 & 0 & 0 \\ 0 & \lambda_2 & 0 \\ 0 & 0 & \lambda_3 \end{bmatrix} \begin{bmatrix} \bar{y}_1 \\ \bar{y}_2 \\ \bar{y}_3 \end{bmatrix}$$

$$\frac{d\bar{y}_1}{dt} = \lambda_1\bar{y}_1, \frac{d\bar{y}_2}{dt} = \lambda_2\bar{y}_2, \frac{d\bar{y}_3}{dt} = \lambda_3\bar{y}_3$$

$$y(t) = v_1\, e^{\lambda_1 t}c_1 + v_2\, e^{\lambda_2 t}c_2 + v_3\, e^{\lambda_3 t}c_3$$

Where $G\ is\ a\ 3 \times 3$ matrix and c_1, c_2, c_3 are constants,

The first option is if three eigen values are real, the point is a node. The second option is that we have one real eigen value and other two are the complex eigen values which are complex

conjugates, in which case the point is called a focus, and the neighboring trajectories are closed or spiraling streamlines indicating a vortex.

$$Vc = y_0 => c = V^{-1}y_0$$

General solution:

$$y(t) = Vexp(\Lambda t)c = Vexp(\Lambda t)V^{-1}y_0$$

The characteristic equation $\det(G - \lambda I) = 0$

$\lambda^3 + P\lambda^2 + Q\lambda + R = 0$ (1)

$$P = -trG = -\nabla.v$$

$$Q = \frac{1}{2}\left([trG]^2 - tr(G^2)\right) = \frac{1}{2}([trG]^2 + \|\Omega\|^2 - \|S\|^2)$$

$$R = -detG = \frac{1}{3}(-P^3 + 3PQ - tr(G^3))$$

All norms are taken as Frobenius norm $\|A\| = [\sum_{i,j} A_{ij}^2]^{\frac{1}{2}}$.

3.1 Q criterion

The Q criterion is one of the most popular vortex identification method proposed by Hunt [44]. Q is defined as the residual of the vorticity tensor norm squared subtract from the strain-rate tensor norm squared.

$$Q = \frac{1}{2}(\|B\|_F^2 - \|A\|_F^2) = \frac{1}{2}(\|\Omega\|^2 - \|S\|^2)$$

Where A is the symmetric part of the velocity gradient tensor,

B is the antisymmetric part of the velocity gradient tensor,

$$A = \frac{1}{2}(\nabla v + \nabla v^T) = \begin{bmatrix} \frac{\partial u}{\partial x} & \frac{1}{2}\left(\frac{\partial u}{\partial y} + \frac{\partial v}{\partial x}\right) & \frac{1}{2}\left(\frac{\partial u}{\partial z} + \frac{\partial w}{\partial x}\right) \\ \frac{1}{2}\left(\frac{\partial v}{\partial x} + \frac{\partial u}{\partial y}\right) & \frac{\partial v}{\partial y} & \frac{1}{2}\left(\frac{\partial v}{\partial z} + \frac{\partial w}{\partial y}\right) \\ \frac{1}{2}\left(\frac{\partial w}{\partial x} + \frac{\partial u}{\partial z}\right) & \frac{1}{2}\left(\frac{\partial w}{\partial y} + \frac{\partial v}{\partial z}\right) & \frac{\partial w}{\partial z} \end{bmatrix}$$

$$B = \frac{1}{2}(\nabla v - \nabla v^T) = \begin{bmatrix} 0 & \frac{1}{2}\left(\frac{\partial u}{\partial y} - \frac{\partial v}{\partial x}\right) & \frac{1}{2}\left(\frac{\partial u}{\partial z} - \frac{\partial w}{\partial x}\right) \\ \frac{1}{2}\left(\frac{\partial v}{\partial x} - \frac{\partial u}{\partial y}\right) & 0 & \frac{1}{2}\left(\frac{\partial v}{\partial z} - \frac{\partial w}{\partial y}\right) \\ \frac{1}{2}\left(\frac{\partial w}{\partial x} - \frac{\partial u}{\partial z}\right) & \frac{1}{2}\left(\frac{\partial w}{\partial y} - \frac{\partial v}{\partial z}\right) & 0 \end{bmatrix}$$

We use Frobenius norm $\|.\|_F^2$ to represent. A region with $Q > 0$ can be thought as a vortex and a second condition, which requires the pressure in the vortical region to be lower than the ambient pressure, is often omitted. However, a threshold $Q_{threshold}$ have to be a positive number that is used to define the region with $Q > Q_{threshold}$ as a vortex in practice. If $Q_{threshold}$ is too small positive number that will create more noise.

3.2 Δ criterion

Chong's critical point theory is defined a vortex core to be the region where ∇v has complex eigen values [45]. In a non-rotating reference frame translating with a fluid particle, the instantaneous streamline patter which applied Taylor series expansion of local velocity to a linear order is governed by the eigenvalues of ∇v. For both compressible and incompressible flows, these streamlines are closed or spiraling if tow of the eigenvalues form a complex conjugate pair. In at that instant flow, the usage of instantaneous streamline implies assuming the velocity field to be frozen at that instant in time. Determining whether the values are real or complex is an

important thing, which is governed by the discriminant of (1) the characteristic equation for the velocity gradient tensor ∇v:

$$\Delta = (\tilde{Q}/3)^3 + (\tilde{R}/2)^2$$

$$\tilde{Q} = Q - \frac{P^2}{3}$$

$$\tilde{R} = R + \frac{2P^3}{27} - PQ/3$$

If $\Delta \leq 0$, we have three eigenvalues of ∇v is real. Otherwise, if $\Delta > 0$, there is one real eigenvalue and two conjugate complex eigenvalues after that we have a point is inside a vortex. For incompressible flow, $\nabla . v = -P = 0 => \tilde{Q} = Q, \tilde{R} = R \; and \; \Delta = (Q/3)^3 + (R/2)^2$

If $Q > 0 => \Delta > 0$, which means that the point with $Q > 0$ is inside a vortex. However, of $Q < 0$, since $(R/2)^2 \; is \; always > 0$, it is possible that $\Delta > 0$. Thus, a point $Q < 0$ is still possible to be inside a vortex, based on Δ criterion. This implies the inconsistence between the Q and Δ criteria.

3.3 λ_{ci} criterion

$\lambda_{ci} criterion$ is extension of Δ criterion. It reads,

$$\lambda_{ci} > \lambda_{ci,thresh}$$

In theory, $\lambda_{ci,thresh} = 0$; however, in practice, $\lambda_{ci,thresh}$ is some small positive number.

According to Zhou [46], λ_{ci} is called the swirling strength of the vortex because in a swirling flor the period of orbit of a fluid particle is $2\pi/\lambda_{ci}$.

$$\frac{dy}{dt} = Gy$$

$$y = Vc$$

$GV = V\Lambda = \Lambda V => VGV^{-1} = \Lambda$

$$G = V\Lambda V^{-1}$$

$$\frac{dVc}{dt} = GVc$$

$$V\frac{dc}{dt} = GVc$$

$\frac{dc}{dt} = V^{-1}GVc$=$\Lambda c$

Where $G\ is\ a\ 3 \times 3$ matrix and when G has a real eigenpair (λ_r, V_r), complex conjugate eigen pairs $(\lambda_{cr} \pm i\lambda_{ci}, V_{cr} \pm iV_{ci})$.

$$G = \begin{bmatrix} | & | & | \\ V_r & V_r + iV_{ci} & V_{cr} - iV_{ci} \\ | & | & | \end{bmatrix} \begin{bmatrix} \lambda_r & 0 & 0 \\ 0 & \lambda_{cr} + i\lambda_{ci} & 0 \\ 0 & 0 & \lambda_{cr} - i\lambda_{ci} \end{bmatrix} \begin{bmatrix} | & | & | \\ V_r & V_r + iV_{ci} & V_{cr} - iV_{ci} \\ | & | & | \end{bmatrix}^{-1}$$

$$G = \begin{bmatrix} | & | & | \\ V_r & V_{cr} & V_{ci} \\ | & | & | \end{bmatrix} \begin{bmatrix} \lambda_r & 0 & 0 \\ 0 & \lambda_{cr} & \lambda_{ci} \\ 0 & -\lambda_{ci} & \lambda_{cr} \end{bmatrix} \begin{bmatrix} | & | & | \\ V_r & V_{cr} & V_{ci} \\ | & | & | \end{bmatrix}^{-1}$$

$$G\begin{bmatrix} \vec{V}_r & \vec{V}_{cr} & \vec{V}_{ci} \end{bmatrix} = \begin{bmatrix} \vec{V}_r & \vec{V}_{cr} & \vec{V}_{ci} \end{bmatrix} \begin{bmatrix} \lambda_r & 0 & 0 \\ 0 & \lambda_{cr} & \lambda_{ci} \\ 0 & -\lambda_{ci} & \lambda_{cr} \end{bmatrix}$$

$$\begin{bmatrix} G\vec{V}_r & G\vec{V}_{cr} & G\vec{V}_{ci} \end{bmatrix} = \begin{bmatrix} \vec{V}_r\lambda_r & \vec{V}_{cr}\lambda_{cr} - \vec{V}_{ci}\lambda_{ci} & \vec{V}_{cr}\lambda_{ci} + \vec{V}_{ci}\lambda_{cr} \end{bmatrix}$$

$$G\vec{V}_r = \lambda_r\vec{V}_r$$

$$G\left(\vec{V}_{cr} + i\vec{V}_{ci}\right) = (\lambda_{cr} + i\lambda_{ci})(\vec{V}_{cr} + i\vec{V}_{ci})$$

$$G\left(\vec{V}_{cr} + i\vec{V}_{ci}\right) = \lambda_{cr}\vec{V}_{cr} + i\lambda_{ci}\vec{V}_{ci} + i\lambda_{ci}\vec{V}_{cr} - \lambda_{ci}\vec{V}_{ci}$$

$$\left(G\vec{V}_{cr} + iG\vec{V}_{ci}\right) = (\lambda_{cr}\vec{V}_{cr} - \lambda_{ci}\vec{V}_{ci}) + i(\lambda_{ci}\vec{V}_{ci} + \lambda_{ci}\vec{V}_{cr})$$

$$\begin{bmatrix}\dot{c_1}\\ \dot{c_2}\\ \dot{c_3}\end{bmatrix} = \begin{bmatrix}\lambda_r & 0 & 0\\ 0 & \lambda_{cr} & \lambda_{ci}\\ 0 & -\lambda_{ci} & \lambda_{cr}\end{bmatrix}\begin{bmatrix}c_1\\ c_2\\ c_3\end{bmatrix}$$

Which has the solution:

$$c_1(t) = c_1\lambda_r = c_1(0)e^{\lambda_r t}$$

$$\begin{bmatrix}\dot{c_2}\\ \dot{c_3}\end{bmatrix} = \begin{bmatrix}\lambda_{cr} & \lambda_{ci}\\ -\lambda_{ci} & \lambda_{cr}\end{bmatrix}\begin{bmatrix}c_2\\ c_3\end{bmatrix} \leftrightarrow \begin{bmatrix}\lambda_{cr}c_2 + & c_3\lambda_{ci}\\ -\lambda_{ci}c_2 + & c_3\lambda_{cr}\end{bmatrix}$$

$$c_2(t) = [c_2(0)\cos(\lambda_{ci}t) + c_3(0)\sin(\lambda_{ci}t)]\, e^{\lambda_{cr}t}$$

$$c_3(t) = [c_3(0)\cos(\lambda_{ci}t) - c_2(0)\sin(\lambda_{ci}t)]\, e^{\lambda_{cr}t}$$

Where t is the time-like parameter and the constant $c_1(0), c_2(0), c_3(0)$ are determined by the initial conditions.

3.4 λ_2 criterion

$$\lambda_2 < 0$$

Where λ_2 is defined to be the second-largest eigenvalue of $\Omega^2 + S^2$

This criterion is based on the notion that a local pressure minimum in plane fails to identify vortices under strong unsteady and viscous effects. By ignoring the unsteady and viscous effects, the symmetric part of gradient of the incompressible Navier-Stokes equation can be defined as

$$A^2 + B^2 = -\nabla(\nabla p)/p$$

Where p is the pressure,

To capture the region of local pressure minimum in a plane, Jeong and Hussain [47] define vortex core as a connected region with two negative eigenvalues of the tensor $A^2 + B^2$. If eigenvalues $\lambda_1 \geq \lambda_2 \geq \lambda_3$ of tensor $A^2 + B^2$, it requires that $\lambda_2 < 0$. In general, λ_2 cannot be expressed as the eigenvalues of the velocity gradient tensor. If eigenvectors are orthonormal, λ_2 can be exclusively determined by the eigenvalues.

3.5 Omega

Before Ω–method is proposed, most of people have believed that the vorticity cannot be generated or destroyed within the interior of fluids, and it is transported inside the flow by advection and diffusion [4]. Because of the great value of the physical meaning and properties of vorticity in investigating vortices dominant flows, several researchers have tried to use vorticity magnitude to conclude coherent structures and identify vortex cores in turbulent flows. For the vortex identification, there are quite a few popular methods in the Eulerian frame for the last three decades, for example Q criterion by Hunt in 1988, the λ_2 criterion by Joeng and Hussan in 1995 and the λ_{ci} criterion by Zhou et al.in 1999, etc. Based on the ideas that vorticity overtakes deformation in vortex, a new vortex identification Ω– method called is introduced by Liu et al. [4] in 2016. Ω is well-defined as a ratio of vorticity tensor norm squared over the sum of vorticity tensor norm squared and deformation in tensor norm squared.

There are many advantages of Ω–method compared to other methods like Q- criterion and λ_2-method [4]:

1. The Ω–method is able to capture vortex well and it is very easy to perform.

2. The physical meaning of Ω–method is clear while the interpretation of the iso-surface values of Q and λ_2 are not clear.

3. If Q and λ_2 iso-surface visualization required somehow arbitrary to capture the vortex structure, Ω is quite universal and does not need much adjustment in different cases. Besides, if we choose iso-surface $\Omega = 0.52$ which can capture the vortices properly in all cases at different time steps.

4. Ω–method can capture both strong and weak vortices well simultaneously while improper Q and λ_2 threshold just capture the strong vortices, and the weak ones are lost or the weak vortices are captured and the strong ones are smeared.

5. $\Omega = 0.52$ is a quantity to approximately define the vortex boundary.

The length and velocity must be used in the non-dimension form to calculate Ω. For the direct numerical simulation, Liu found the vorticity direction is quite different from the vortex rotation direction in general 3-D vortical flow. The idea of vorticity is splitting into two parts: a vortical part and non-vortical part. Besides, a parameter Ω is introduced to represent the ratio of vortical vorticity over the whole vorticity inside a vortex core.

$$\nabla V = \frac{1}{2}(\nabla V + \nabla V^T) + \frac{1}{2}(\nabla V - \nabla V^T) = A + B$$

Where A is symmetric and also represent deformation,

B is anti-symmetric and represent whole vorticity.

The square of Frobenius norm of A and B is defined by:

$$a = trace(A^T A) = \sum_{i=1}^{3}\sum_{j=1}^{3}(A_{ij})^2$$

$$b = trace(B^T B) = \sum_{i=1}^{3}\sum_{j=1}^{3}(B_{ij})^2$$

Ω is defined as a ratio of the vorticity tensor norm squared over the sum of the vorticity tensor norm squared and deformation norm squared [4]:

$$\Omega = \frac{\|B\|_F^2}{\|A\|_F^2 + \|B\|_F^2} = \frac{b}{a+b}$$

Where $a = \|A\|_F^2$, $b = \|B\|_F^2$, $\|.\|_F$ is the Frobenius norm.

In numerical computation, we have to add a small positive parameter ε to avoid non-physical noises.

$$\Omega = \frac{b}{a+b+\varepsilon}$$

An estimate of ratio Ω is introduced which shows vortex is formed when the vorticity is strong but deformation is weak:

$$\Omega = \frac{b}{a+b}$$

Where a, b are positive numbers,

However, in our group research we choose to add ε which is a small positive number to avoid division by zero in the denominator. Note that the length and velocity must be used in the nondimensional form to calculate Ω. If not, ε have to be a large number depending on the length and velocity dimension. First, the value of Ω need to be between zero and one $0 \leq \Omega \leq 1$.

Second, in terms of a 2D rigid-body vortex with a uniform angular velocity ϕ, the velocity field is given as $V = (-\phi y, \phi x)$. If $a = 0, \Omega = 1$

$$\Omega = \frac{(\nabla \times V.R)^2}{\|\nabla \times V\|_2^2.\|R\|_2^2} \approx \frac{b}{a+b}$$

This means when vorticity is aligned with rotation, the deformation is small and vortex is really an area where projection of vorticity in the rotation axial is about the same. For Omega method, we have to use a parameter larger than 0.52. We always use $\Omega = 0.51$ or $\Omega = 0.52$ to fix the threshold. However, the Omega method is insensitive to moderate threshold change. This is one of the advantages of Omega method over other vortex identification method. For the LES case of shock and boundary layer interaction and the DNS case of flow transition, if we use $\Omega = 0.52 - 0.6$, vortex structure identified by the Omega method are very similar. In our research, we decide to use $\Omega = 0.52$ because it is reliable and it can present the periphery of vortices for many different cases. This conclusion has been confirmed by a lot of Omega users in practice. If we select $\Omega = 0.52$ is only empirical number for approximation of vortex boundaries and higher threshold, such as $\Omega = 0.8\ or\ 0.9$, ect., may be needed if the vortex cores will be tracked. However, the shape of vortex structures will be merely thinner or fatter with the moderate change of the threshold [6].

3.6 Liutex

The new vortex vector named Rotex was proposed by Liu et al. [2] with direction of local rotation axis (an eigenvector of velocity gradient tensor) and angular speed (magnitude of Liutex vector) while other identification methods could not give direction of rotation axis. Liutex

represents the absolute rotational strength, which is unique and precise. The name, Rortex was changed to Liutex in December 2018 [2].

$$\vec{\mathrm{R}} = \mathrm{R}\vec{\mathrm{r}}$$

Where R: magnitude of Liutex vector (angular speed of rigid rotation),

$\vec{\mathrm{r}}$: an eigenvector of velocity gradient tensor (direction of the rigid rotation axis),

For physics formula, definition of velocity gradient tensor is defined as:

$$d\vec{v} = \nabla\vec{v} \cdot d\vec{r}$$

For mathematic formula, definition of velocity gradient tensor is defined as:

$$d\vec{v} = \alpha . d\vec{r}$$

From these equations above, we have:

$$d\vec{v} = \nabla\vec{v} . \vec{r} = \lambda_r \vec{r}$$

We use r, λ_r to substitute dr, α to highlight that are real eigenvector and real eigenvalue of the velocity gradient tensor.

$$\nabla\vec{v} . \vec{r} = \lambda_r \vec{r}$$

Where $\vec{v} = [u, v, w]^T$ is the velocity vector,

After getting direction of the rigid rotational axis, we will find the exact angular speed of the rigid rotation (called magnitude of Liutex). Choosing direction of the local rotation axis Z is the direction of Rortex/Liutex and the rotational strength of the local fluid rotation is the magnitude of Rortex/Liutex. Thus, XY plane will perpendicular to Z plan. Next, we will do transformation matrix from xyz plane to XYZ plane by applying Transformation Matrix formula. If we pick u, v, w and w be velocity components along $x, y \; and \; z$ axes, then we will pick $U, V \; and \; W$ be velocity components along the new $X, Y \; and \; Z$ axes.

$$\nabla\vec{\boldsymbol{v}} = \begin{bmatrix} \frac{\partial u}{\partial x} & \frac{\partial u}{\partial y} & \frac{\partial u}{\partial z} \\ \frac{\partial v}{\partial x} & \frac{\partial v}{\partial y} & \frac{\partial v}{\partial z} \\ \frac{\partial w}{\partial x} & \frac{\partial w}{\partial y} & \frac{\partial w}{\partial z} \end{bmatrix}$$

$$\nabla\vec{\boldsymbol{V}} = \begin{bmatrix} \frac{\partial U}{\partial X} & \frac{\partial U}{\partial Y} & 0 \\ \frac{\partial V}{\partial X} & \frac{\partial V}{\partial Y} & 0 \\ \frac{\partial W}{\partial X} & \frac{\partial W}{\partial Y} & \frac{\partial W}{\partial Z} \end{bmatrix}$$

Second, Q rotation is obtained to find the rotation strength.

$$\nabla\vec{\boldsymbol{V}} = \boldsymbol{Q}\nabla\vec{\boldsymbol{v}}\boldsymbol{Q}^{\mathrm{T}} = \begin{bmatrix} \frac{\partial U}{\partial X} & \frac{\partial U}{\partial Y} & 0 \\ \frac{\partial V}{\partial X} & \frac{\partial V}{\partial Y} & 0 \\ \frac{\partial W}{\partial X} & \frac{\partial W}{\partial Y} & \frac{\partial W}{\partial Z} \end{bmatrix} \text{with } \boldsymbol{Q}^{\mathrm{T}} = \boldsymbol{Q}^{-1} \text{ and } \boldsymbol{Q} \text{ is rotation matrix}$$

$$\boldsymbol{Q} = \begin{bmatrix} cos\phi + \gamma_x^2(1-cos\phi) & \gamma_y\gamma_x(1-cos\phi) + \gamma_z sin\phi & \gamma_z\gamma_x(1-cos\phi) - \gamma_y sin\phi \\ \gamma_x\gamma_y(1-cos\phi) - \gamma_z sin\phi & cos\phi + \gamma_y^2(1-cos\phi) & \gamma_y\gamma_z(1-cos\phi) + \gamma_x sin\phi \\ \gamma_x\gamma_y(1-cos\phi) + \gamma_z sin\phi & \gamma_z\gamma_y(1-cos\phi) - \gamma_x sin\phi & cos\phi + \gamma_z^2(1-cos\phi) \end{bmatrix}$$

$$\phi = \mathrm{acos}\,(c)$$

$$c = \begin{bmatrix} 0 \\ 0 \\ 1 \end{bmatrix} \cdot \vec{r}$$

Once the local rotation axis Z is obtained, the rotation strength is determined in the XY plane perpendicular to the local rotation axis Z. This can be achieved by a second coordinate rotation in the XY plane. When the XYZ-frame is rotated around the $Z - axis$ by an angle θ, the velocity gradient tensor will become

$$\nabla\vec{\boldsymbol{V}}_\theta = \boldsymbol{P}\nabla\vec{\boldsymbol{V}}\boldsymbol{P}^{-1}$$

$$\begin{bmatrix} \frac{\partial U}{\partial X}|\theta & \frac{\partial U}{\partial Y}|\theta & 0 \\ \frac{\partial V}{\partial X}|\theta & \frac{\partial V}{\partial Y}|\theta & 0 \\ \frac{\partial W}{\partial X}|\theta & \frac{\partial W}{\partial Y}|\theta & \frac{\partial W}{\partial Z}|\theta \end{bmatrix} = \begin{bmatrix} cos\theta & sin\theta & 0 \\ -sin\theta & cos\theta & 0 \\ 0 & 0 & 1 \end{bmatrix} \begin{bmatrix} \frac{\partial U}{\partial X} & \frac{\partial U}{\partial Y} & 0 \\ \frac{\partial V}{\partial X} & \frac{\partial V}{\partial Y} & 0 \\ \frac{\partial W}{\partial X} & \frac{\partial W}{\partial Y} & \frac{\partial W}{\partial Z} \end{bmatrix} \begin{bmatrix} cos\theta & -sin\theta & 0 \\ sin\theta & cos\theta & 0 \\ 0 & 0 & 1 \end{bmatrix}$$

$$\begin{bmatrix} \frac{\partial U}{\partial X}|\theta & \frac{\partial U}{\partial Y}|\theta & 0 \\ \frac{\partial V}{\partial X}|\theta & \frac{\partial V}{\partial Y}|\theta & 0 \\ \frac{\partial W}{\partial X}|\theta & \frac{\partial W}{\partial Y}|\theta & \frac{\partial W}{\partial Z}|\theta \end{bmatrix}$$

$$= \begin{bmatrix} \frac{\partial U}{\partial X}cos^2\theta + \frac{\partial U}{\partial Y}sin\theta cos\theta + \frac{\partial V}{\partial X}sin\theta cos\theta + \frac{\partial V}{\partial Y}sin^2\theta & -\frac{\partial U}{\partial X}sin\theta cos\theta + \frac{\partial U}{\partial Y}cos^2\theta - \frac{\partial V}{\partial X}sin^2\theta + \frac{\partial V}{\partial Y}sin\theta cos\theta & 0 \\ -\frac{\partial U}{\partial X}sin\theta cos\theta - \frac{\partial U}{\partial Y}sin^2\theta + \frac{\partial V}{\partial X}cos^2\theta + \frac{\partial V}{\partial Y}sin\theta cos\theta & \frac{\partial U}{\partial X}sin^2\theta - \frac{\partial U}{\partial Y}sin\theta cos\theta - \frac{\partial V}{\partial X}sin\theta cos\theta + \frac{\partial V}{\partial Y}sin\theta cos^2\theta & 0 \\ \frac{\partial W}{\partial X}cos\theta + \frac{\partial W}{\partial Y}sin\theta & -\frac{\partial W}{\partial X}sin\theta + \frac{\partial W}{\partial Y}cos\theta & \frac{\partial W}{\partial Z} \end{bmatrix}$$

Where $\boldsymbol{P}$ is the rotation matrix around the Z -axis and can be written as:

$$\boldsymbol{P} = \begin{bmatrix} cos\theta & sin\theta & 0 \\ -sin\theta & cos\theta & 0 \\ 0 & 0 & 1 \end{bmatrix}, \boldsymbol{P}^{-1} = \boldsymbol{P}^T = \begin{bmatrix} cos\theta & -sin\theta & 0 \\ sin\theta & cos\theta & 0 \\ 0 & 0 & 1 \end{bmatrix}$$

So, we have

$$\frac{\partial U}{\partial Y}|_\theta = \alpha si\, n(2\theta + \varphi) - \beta$$

$$\frac{\partial V}{\partial X}|_\theta = \alpha si\, n(2\theta + \varphi) + \beta$$

$$\frac{\partial U}{\partial X}|_\theta = -\alpha \cos(2\theta + \varphi) + \frac{1}{2}\left(\frac{\partial U}{\partial X} + \frac{\partial V}{\partial Y}\right)$$

$$\frac{\partial V}{\partial Y}|_\theta = \alpha \cos(2\theta + \varphi) + \frac{1}{2}\left(\frac{\partial U}{\partial X} + \frac{\partial V}{\partial Y}\right)$$

Where $\alpha = \frac{1}{2}\sqrt{\left(\frac{\partial V}{\partial Y} - \frac{\partial U}{\partial X}\right)^2 + \left(\frac{\partial V}{\partial X} + \frac{\partial U}{\partial Y}\right)^2}$, and $\alpha > 0$

$$\beta = \frac{1}{2}\left(\frac{\partial V}{\partial X} - \frac{\partial U}{\partial Y}\right)$$

$$\varphi = \begin{cases} arctan\left(\dfrac{\frac{\partial V}{\partial X} + \frac{\partial U}{\partial Y}}{\frac{\partial V}{\partial Y} - \frac{\partial U}{\partial X}}\right), & \dfrac{\partial V}{\partial Y} - \dfrac{\partial U}{\partial X} \neq 0 \\ \dfrac{\pi}{2}, & \dfrac{\partial V}{\partial Y} - \dfrac{\partial U}{\partial X} = 0, \dfrac{\partial V}{\partial X} + \dfrac{\partial U}{\partial Y} > 0 \\ -\dfrac{\pi}{2}, & \dfrac{\partial V}{\partial Y} - \dfrac{\partial U}{\partial X} = 0, \dfrac{\partial V}{\partial X} + \dfrac{\partial U}{\partial Y} < 0 \end{cases}$$

(Note: If $\frac{\partial V}{\partial Y} - \frac{\partial U}{\partial X} = 0, \frac{\partial V}{\partial X} + \frac{\partial U}{\partial Y} = 0, \frac{\partial V}{\partial X} = \beta, \frac{\partial U}{\partial Y} = -\beta$ for any θ, thus φ is not needed.)

$$\frac{\partial U}{\partial X}|\theta = \frac{\partial U}{\partial X}cos^2\,\theta + \frac{\partial U}{\partial Y}sin\theta cos\theta + \frac{\partial V}{\partial X}sin\theta cos\theta + \frac{\partial V}{\partial Y}sin^2\theta$$

$$\frac{\partial U}{\partial X}|\theta = \frac{\partial U}{\partial X}cos^2\,\theta + \frac{\partial U}{\partial Y}sin\theta cos\theta + \frac{\partial V}{\partial X}sin\theta cos\theta + \frac{\partial V}{\partial Y}(1 - cos^2\theta)$$

$$\frac{\partial U}{\partial X}|\theta = -\left(-\frac{\partial U}{\partial X} + \frac{\partial V}{\partial Y}\right)cos^2\,\theta + \frac{sin2\theta}{2}\left(\frac{\partial V}{\partial X} + \frac{\partial U}{\partial Y}\right) + \frac{\partial V}{\partial Y}$$

$$\frac{\partial U}{\partial X}|\theta = -\left(\sqrt{A^2 + B^2}cos\varphi\right)cos^2\,\theta + \frac{sin2\theta}{2}\left(\sqrt{A^2 + B^2}sin\varphi\right) + \frac{\partial V}{\partial Y}$$

$$\frac{\partial U}{\partial X}|\theta = -\frac{1}{2}\sqrt{A^2 + B^2}(2cos^2\,\theta\cos\varphi - \sin2\theta sin\varphi) + \frac{\partial V}{\partial Y}$$

$$\frac{\partial U}{\partial X}|\theta = -\frac{1}{2}\sqrt{A^2 + B^2}(2cos^2\,\theta\cos\varphi - \sin2\theta sin\varphi - \cos\varphi + \cos\varphi) + \frac{\partial V}{\partial Y}$$

$$\frac{\partial U}{\partial X}|\theta = -\frac{1}{2}\sqrt{A^2 + B^2}((2cos^2\,\theta - 1)\cos\varphi - \sin2\theta sin\varphi + \cos\varphi) + \frac{\partial V}{\partial Y}$$

$$\frac{\partial U}{\partial X}|\theta = -\frac{1}{2}\sqrt{A^2 + B^2}(cos2\theta\,\cos\varphi - \sin2\theta sin\varphi + \cos\varphi) + \frac{\partial V}{\partial Y}$$

$$\frac{\partial U}{\partial X}|\theta = -\frac{1}{2}\sqrt{A^2 + B^2}(\cos\,(2\theta + \varphi) + \cos\varphi) + \frac{\partial V}{\partial Y}$$

$$\frac{\partial U}{\partial X}|\theta = -\frac{1}{2}\sqrt{A^2+B^2}\cos(2\theta+\varphi) - \frac{1}{2}\mathrm{A} + \frac{\partial V}{\partial Y}$$

$$\frac{\partial U}{\partial X}|\theta = -\frac{1}{2}\sqrt{A^2+B^2}\cos(2\theta+\varphi) - \frac{1}{2}\left(-\frac{\partial U}{\partial X} + \frac{\partial V}{\partial Y}\right) + \frac{\partial V}{\partial Y}$$

$$\frac{\partial U}{\partial X}|\theta = -\frac{1}{2}\sqrt{A^2+B^2}\cos(2\theta+\varphi) + \frac{1}{2}\left(\frac{\partial U}{\partial X} + \frac{\partial V}{\partial Y}\right)$$

$$\frac{\partial U}{\partial X}|\theta = -\alpha\cos(2\theta+\varphi) + \frac{1}{2}\left(\frac{\partial U}{\partial X} + \frac{\partial V}{\partial Y}\right)$$

$$\frac{\partial V}{\partial Y}|\theta = \frac{\partial U}{\partial X}sin^2\,\theta - \frac{\partial U}{\partial Y}sin\theta cos\theta - \frac{\partial V}{\partial X}sin\theta cos\theta + \frac{\partial V}{\partial Y}sin\theta cos^2\theta$$

$$\frac{\partial V}{\partial Y}|\theta = \frac{\partial U}{\partial X}(1-cos^2\,\theta) - \frac{\partial U}{\partial Y}sin\theta cos\theta - \frac{\partial V}{\partial X}sin\theta cos\theta + \frac{\partial V}{\partial Y}sin\theta cos^2\theta$$

$$\frac{\partial V}{\partial Y}|\theta = \left(-\frac{\partial U}{\partial X} + \frac{\partial V}{\partial Y}\right)cos^2\,\theta - \frac{sin2\theta}{2}\left(\frac{\partial V}{\partial X} + \frac{\partial U}{\partial Y}\right) + \frac{\partial U}{\partial X}$$

$$\frac{\partial V}{\partial Y}|\theta = -\left(\sqrt{A^2+B^2}cos\varphi\right)cos^2\,\theta - \frac{sin2\theta}{2}\left(\sqrt{A^2+B^2}sin\varphi\right) + \frac{\partial U}{\partial X}$$

$$\frac{\partial U}{\partial X}|\theta = -\frac{1}{2}\sqrt{A^2+B^2}(2cos^2\,\theta\cos\varphi - \sin2\theta sin\varphi) + \frac{\partial U}{\partial X}$$

$$\frac{\partial V}{\partial Y}|\theta = \frac{1}{2}\sqrt{A^2+B^2}(2cos^2\,\theta\cos\varphi - \sin2\theta sin\varphi - \cos\varphi + \cos\varphi) + \frac{\partial U}{\partial X}$$

$$\frac{\partial V}{\partial Y}|\theta = \frac{1}{2}\sqrt{A^2+B^2}((2cos^2\,\theta - 1)\cos\varphi - \sin2\theta sin\varphi + \cos\varphi) + \frac{\partial U}{\partial X}$$

$$\frac{\partial V}{\partial Y}|\theta = \frac{1}{2}\sqrt{A^2+B^2}(cos2\theta\,\cos\varphi - \sin2\theta sin\varphi + \cos\varphi) + \frac{\partial U}{\partial X}$$

$$\frac{\partial V}{\partial Y}|\theta = \frac{1}{2}\sqrt{A^2 + B^2}(\cos(2\theta + \varphi) + \cos\varphi) + \frac{\partial U}{\partial X}$$

$$\frac{\partial V}{\partial Y}|\theta = \frac{1}{2}\sqrt{A^2 + B^2}\cos(2\theta + \varphi) + \frac{1}{2}\mathrm{A} + \frac{\partial U}{\partial X}$$

$$\frac{\partial V}{\partial Y}|\theta = \frac{1}{2}\sqrt{A^2 + B^2}\cos(2\theta + \varphi) + \frac{1}{2}\left(-\frac{\partial U}{\partial X} + \frac{\partial V}{\partial Y}\right) + \frac{\partial U}{\partial X}$$

$$\frac{\partial V}{\partial Y}|\theta = \frac{1}{2}\sqrt{A^2 + B^2}\cos(2\theta + \varphi) + \frac{1}{2}\left(\frac{\partial U}{\partial X} + \frac{\partial V}{\partial Y}\right)$$

$$\frac{\partial V}{\partial Y}|\theta = \alpha\cos(2\theta + \varphi) + \frac{1}{2}\left(\frac{\partial U}{\partial X} + \frac{\partial V}{\partial Y}\right)$$

$$\frac{\partial U}{\partial Y}|\theta = -\frac{\partial U}{\partial X}sin\theta cos\theta + \frac{\partial U}{\partial Y}cos^2\theta - \frac{\partial V}{\partial X}sin^2\theta + \frac{\partial V}{\partial Y}sin\theta cos\theta$$

$$\frac{\partial U}{\partial Y}|\theta = -\frac{\partial U}{\partial X}sin\theta cos\theta + \frac{\partial U}{\partial Y}(1 - sin^2\theta) - \frac{\partial V}{\partial X}sin^2\theta + \frac{\partial V}{\partial Y}sin\theta cos\theta$$

$$\frac{\partial U}{\partial Y}|\theta = -\left(\frac{\partial U}{\partial Y} + \frac{\partial V}{\partial X}\right)sin^2\,\theta + \frac{sin2\theta}{2}\left(-\frac{\partial U}{\partial X} + \frac{\partial V}{\partial Y}\right) + \frac{\partial U}{\partial Y}$$

$$\frac{\partial U}{\partial Y}|\theta = -\left(\sqrt{A^2 + B^2}cos\varphi\right)sin^2\,\theta - \frac{sin2\theta}{2}\left(\sqrt{A^2 + B^2}cos\varphi\right) + \frac{\partial U}{\partial Y}$$

$$\frac{\partial U}{\partial Y}|\theta = \frac{1}{2}\sqrt{A^2 + B^2}(2cos^2\,\theta\cos\varphi - \sin2\theta sin\varphi) + \frac{\partial U}{\partial Y}$$

$$\frac{\partial U}{\partial Y}|\theta = \frac{1}{2}\sqrt{A^2 + B^2}(2cos^2\,\theta\cos\varphi - \sin2\theta sin\varphi - \sin\varphi + \sin\varphi) + \frac{\partial U}{\partial Y}$$

$$\frac{\partial U}{\partial Y}|\theta = \frac{1}{2}\sqrt{A^2 + B^2}((-2sin^2\,\theta + 1)\sin\varphi - \sin2\theta cos\varphi - sin\varphi) + \frac{\partial U}{\partial Y}$$

$$\frac{\partial U}{\partial Y}|\theta = \frac{1}{2}\sqrt{A^2+B^2}(sin2\theta\cos\varphi + \cos2\theta sin\varphi - sin\varphi) + \frac{\partial U}{\partial Y}$$

$$\frac{\partial U}{\partial Y}|\theta = \frac{1}{2}\sqrt{A^2+B^2}(\sin(2\theta+\varphi) - sin\varphi) + \frac{\partial U}{\partial Y}$$

$$\frac{\partial U}{\partial Y}|\theta = \frac{1}{2}\sqrt{A^2+B^2}\sin(2\theta+\varphi) - \frac{1}{2}\mathrm{B} + \frac{\partial U}{\partial Y}$$

$$\frac{\partial U}{\partial Y}|\theta = \frac{1}{2}\sqrt{A^2+B^2}\sin(2\theta+\varphi) - \frac{1}{2}\left(\frac{\partial U}{\partial Y} + \frac{\partial V}{\partial X}\right) + \frac{\partial U}{\partial Y}$$

$$\frac{\partial U}{\partial Y}|\theta = \frac{1}{2}\sqrt{A^2+B^2}\sin(2\theta+\varphi) - \frac{1}{2}\left(\frac{\partial V}{\partial X} - \frac{\partial U}{\partial Y}\right)$$

$$\frac{\partial U}{\partial Y}|\theta = \alpha\sin(2\theta+\varphi) - \beta$$

$$\frac{\partial V}{\partial X}|\theta = -\frac{\partial U}{\partial X}sin\theta cos\theta - \frac{\partial U}{\partial Y}sin^2\theta + \frac{\partial V}{\partial X}cos^2\theta + \frac{\partial V}{\partial Y}sin\theta cos\theta$$

$$\frac{\partial V}{\partial X}|\theta = -\frac{\partial U}{\partial X}sin\theta cos\theta - \frac{\partial U}{\partial Y}sin^2\theta + \frac{\partial V}{\partial X}(1 - sin^2\theta) + \frac{\partial V}{\partial Y}sin\theta cos\theta$$

$$\frac{\partial V}{\partial X}|\theta = -\left(\frac{\partial U}{\partial Y} + \frac{\partial V}{\partial X}\right)sin^2\,\theta + \frac{sin2\theta}{2}\left(-\frac{\partial U}{\partial X} + \frac{\partial V}{\partial Y}\right) + \frac{\partial V}{\partial X}$$

$$\frac{\partial V}{\partial X}|\theta = -\left(\sqrt{A^2+B^2}sin\varphi\right)sin^2\,\theta + \frac{sin2\theta}{2}\left(\sqrt{A^2+B^2}cos\varphi\right) + \frac{\partial V}{\partial X}$$

$$\frac{\partial V}{\partial X}|\theta = \frac{1}{2}\sqrt{A^2+B^2}(-2sin^2\,\theta\sin\varphi + \sin2\theta cos\varphi) + \frac{\partial V}{\partial X}$$

$$\frac{\partial V}{\partial X}|\theta = \frac{1}{2}\sqrt{A^2+B^2}(-2sin^2\,\theta\sin\varphi + \sin2\theta cos\varphi - \sin\varphi + \sin\varphi) + \frac{\partial V}{\partial X}$$

$$\frac{\partial V}{\partial X}|\theta = \frac{1}{2}\sqrt{A^2+B^2}((-2sin^2\,\theta+1)\sin\varphi + \sin 2\theta cos\varphi - sin\varphi) + \frac{\partial V}{\partial X}$$

$$\frac{\partial V}{\partial X}|\theta = \frac{1}{2}\sqrt{A^2+B^2}(cos2\theta\,\sin\varphi + \sin 2\theta cos\varphi - sin\varphi) + \frac{\partial V}{\partial X}$$

$$\frac{\partial V}{\partial X}|\theta = \frac{1}{2}\sqrt{A^2+B^2}(\sin(2\theta+\varphi) - sin\varphi) + \frac{\partial V}{\partial X}$$

$$\frac{\partial V}{\partial X}|\theta = \frac{1}{2}\sqrt{A^2+B^2}\sin(2\theta+\varphi) - \frac{1}{2}\mathrm{B} + \frac{\partial V}{\partial X}$$

$$\frac{\partial V}{\partial X}|\theta = \frac{1}{2}\sqrt{A^2+B^2}\sin(2\theta+\varphi) - \frac{1}{2}\left(\frac{\partial U}{\partial Y} + \frac{\partial V}{\partial X}\right) + \frac{\partial V}{\partial X}$$

$$\frac{\partial V}{\partial X}|\theta = \frac{1}{2}\sqrt{A^2+B^2}\sin(2\theta+\varphi) + \frac{1}{2}\left(\frac{\partial V}{\partial X} - \frac{\partial U}{\partial Y}\right)$$

$$\frac{\partial V}{\partial X}|\theta = \alpha\sin(2\theta+\varphi) + \beta$$

$$g_{Z\theta} = -\frac{\partial V}{\partial X}|_\theta \frac{\partial U}{\partial Y}|_\theta = \beta^2 - \alpha^2\sin^2(2\theta+\varphi) > 0$$

In order to satisfy this condition for all θ, we must require $\beta^2 > \alpha^2$

$$\frac{\partial U}{\partial Y}|\theta = \alpha\sin(2\theta+\varphi) - \beta = \alpha - \beta$$

$$\frac{\partial V}{\partial X}|\theta = \alpha\sin(2\theta+\varphi) + \beta = \alpha + \beta$$

$$\frac{\partial U}{\partial X}|\theta = -\alpha\cos(2\theta+\varphi) + \frac{1}{2}\left(\frac{\partial U}{\partial X} + \frac{\partial V}{\partial Y}\right)$$

Finally, the rotational strength of Liutex is defined as:

$$\mathrm{R} = \begin{cases} 2(\beta - \alpha), & \beta^2 > \alpha^2 \\ 0, & \beta^2 \leq \alpha^2 \end{cases}$$

Wang et al. [8] created an explicit formula to calculate the magnitude of Liutex:

$$\mathrm{R} = \vec{\omega}.\vec{\mathrm{r}} - \sqrt{(\vec{\omega}.\vec{\mathrm{r}})^2 - 4\lambda_{\mathrm{ci}}^2},$$

Where $\sqrt{(\vec{\omega}.\vec{\mathrm{r}})^2 - 4\lambda_{\mathrm{ci}}^2}$ is the pure shear part,

$\vec{\omega}$ is local vorticity vector,

$\vec{r}$ is an eigenvector of velocity gradient tensor (local rotation axis),

λ_{ci} is an imaginary part of the complex eigenvalue of velocity gradient tensor,

$\vec{\omega}.\vec{\mathrm{r}}$ is magnitude of vorticity in the direction of $\vec{\mathrm{r}}$,

Therefore, the Liutex vector can be defined as: $\vec{\mathrm{R}} = \mathrm{Rr} = \left\{\vec{\omega}.\vec{\mathrm{r}} - \sqrt{(\vec{\omega}.\vec{\mathrm{r}})^2 - 4\lambda_{\mathrm{ci}}^2}\right\} r.$

3.6.1 Normalized Rortex/vortex identification method (Ω_R)

Non-dimensional, normalized and case-independent ratio based on definition of Rotex is used in Ω_R method. Based on the idea for Omega method, a new vortex identification criterion, named Ω_R, is proposed for the normalization of Rortex. Ω_R is measures the relative rotation strength on the plane perpendicular to the local rotation axis. Besides, Ω_R is a normalized function from 0 to 1[6]. Ω_R is defined as the ratio of β squared over the sum of β squared and α squared and can be written as:

$$\Omega_R = \frac{\beta^2}{\alpha^2 + \beta^2 + \varepsilon}$$

The small positive parameter ε is introduced in the denominator of Ω_R to remove non-physical noises. Besides, ε is empirically defined as a function of the maximum of the term $\beta^2 - \alpha^2$ proposed as follows:

$$\varepsilon = b \times (\beta^2 - \alpha^2)_{max}$$

Where b is a positive number around $0.001 \sim 0.002$. We pick $b = 0.001$ for all the test cases and all-time steps in this paper. For each case, b is a fixed parameter and the term $(\beta^2 - \alpha^2)_{\text{max}}$ can be easily obtained at each time step and adding ε to avoid diving by zero. We choose the iso-surface of $\Omega_R = 0.52$ can be chosen to visualize vortex structures and to indicate the region where the vorticity overtakes the principle strain rate on the plane normal to local rotation axis.

The new Ω_R method has several advantages:

- Ω_R is able to measure the relation rotation strength on the plane perpendicular to local rotation axis.
- Ω_R is a normalized function from 0 to 1 and can be further used in statistic and correlation analysis as a physical quantity.
- Ω_R can separate the rotation vortices from shear layers, discontinuity structures and other non-physical structures.
- Compared with many vortex identification methods which require case-dependent thresholds to capture the vortex structure, $\Omega_R$is quite robust and be always set as 0.52 to capture vortex structures in different cases and at different time steps.

3.6.2 Modified normalized Rortex/vortex identification method ($\tilde{\Omega}_R, \Omega_R$)

Modified normalized Rortex/vortex identification method, $\tilde{\Omega}_R$ was proposed by Liu and Liu [5] in 2019 to improve and solve bulging phenomenon on iso surfaces of the normalized Rortex/vortex identification method (Ω_R) by Dong et al. [6] from 2018. Furthermore, $\tilde{\Omega}_R$ still maintained all advantages of the original Ω_R method. First, in the other vortex identification methods we have to pick different threshold for each time step to accurately capture vortex structure; on the other hand, $\tilde{\Omega}_R = 0.52$ clearly visualize vortex structures and it is quite robust. Second, $\tilde{\Omega}_R$ is a normalized function with a range of 0 to 1, which is useful for calculating correlation analysis in statistics. Third, $\tilde{\Omega}_R$ can capture precisely both strong and weak vortices simultaneously. However, by using Ω_R vortex structure is shown not that smooth as respected and there is some problem on bulging phenomenon on the iso surfaces. A year later, a new method named modified normalized Rortex/vortex identification method was proposed by Liu and Liu [5] to solve bulging phenomenon problem.

$$\tilde{\Omega}_R = \frac{\beta^2}{\beta^2 + \alpha^2 + \lambda_{cr}^2 + \frac{1}{2}\lambda_r^2 + \varepsilon},$$

For all three methods, $\Omega, \Omega_R \; and \; \tilde{\Omega}_R$ required a parameter greater than 0.5. Moreover, $\tilde{\Omega}_R = 0.52$ was an empirical number that always worked well for most of the cases.

Chapter 4
POD

4.1 Eigenvalue Decomposition

Before understanding POD and SVD, we have to review eigenvalues and eigenvectors of a matrix.

$$Av = \lambda v$$

Where $A\ is\ a\ matrix \in C^{nxn}$,

$v:\ a\ vector \in C^n\ is\ called\ an\ eigenvector\ of\ A$,

λ: $a\ scalar \in C\ is\ called\ an\ eigenvalue\ of\ A$,

If v is an eigenvector of of matrix A, αv is also an eigenvector of matrix A with $\alpha \in C$. The eigenvectors getting from the computer programs are usually normalized, so they have unit magnitude. A spectrum of A is the set of all eigenvalue of A. The magnitude of eigenvalue will decide whether the operation A will increase or decrease the size of original vectors in particular direction. If we multiply A by λ^n and we pick n is a large number ($n \in N$), the result of vector from the compound operations can be showed by the eigenvector having the eigenvalue with the largest magnitude.

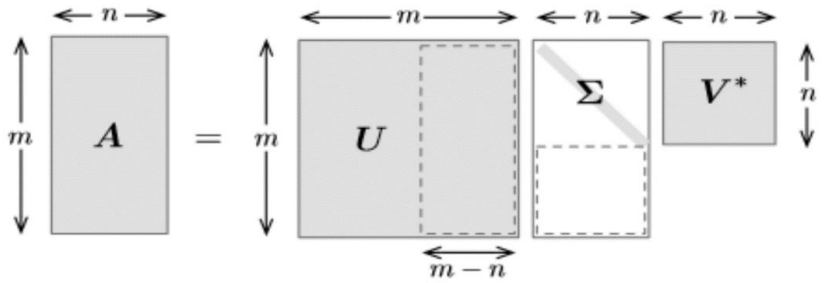

Figure 4. 1 Graphical Singular Value Decomposition [18]

If A has n linearly independent eigenvalues $\lambda_j (j = 1,2,3 \dots, n)$ and $eigenvectors$ v_j,

$$AV = V\Lambda$$

Where $V = [v_1 v_2\ v_3 \dots v_n] \in C^{n\times n} and\ \Lambda = diag(\lambda_1, \lambda_2, \dots, \lambda_n) \in C^{n\times n}$

$$AVV^{-1} = V\Lambda V^{-1}$$

The eigenvalue decomposition to hold, A needs to have a full set of n linearly independent eigenvectors.

$$A = AI = V\Lambda V^{-1}$$

For linear dynamic system:

Let $x(t) \in C^n$ with $x(t) = \exp(At)\, x(0) = Vexp(\Lambda t)V^{-1}x(0)$

With $x(0)$ is the initial condition.

$$x(t) = e^{\lambda t}v$$

$$\dot{x}(t) = Ax(t)$$

$$\lambda e^{\lambda t}v = Ae^{\lambda t}v$$

$$Av = \lambda v$$

The real and imaginary parts of λ_j represent the growth rate and the frequency where the state variable evolves in the direction of eigenvector v_j. If we want to have the stable linear system, all eigenvalues need to be on the left-hand side of the complex plane, i.e., $Re(\lambda_j) \leq 0 \; for \; all \; j$.

4.2 Singular Value Decomposition

The existence and theory of singular value decomposition [48] (SVD) was developed by several mathematicians, including Eugenio Beltrami (1835-1899), Camille Jordan (1838-1921), James Sylvester (1814-1897), Erhard Schmidt (1876-1959), and Hermann Weyl (1885-1955). Thanks to their contribution and due to developing of computer, SVD starts gaining its audients to become one of most powerful tools for minimizing the storage of data and transferring data. In linear algebra, the singular value decomposition is one of the most important factorizations that can reveal important properties of the matrix that otherwise could escape detection. SVD was proposed by Golub and Van Loan (1983) [49]. However, only in late of 20th century, the applications of the technique were used widespread as its algorithms could be developed for its efficient implementation. Besides, SVD is a powerful and numerically stable method of decomposing a data matrix. The SVD is a useful and efficient method for reducing dimension of matrix where it is possible to use the SVD to obtain optimal low-rank matrix approximations. People use the SVD to see how a rectangular matric or operator stretches or rotates a vector. Nowadays, applications of SVD are used in least squares data fitting, image compression, facial

recognition, principal component analysis, numerical rank of matrix and so on [50]. To know more details about proceeding with SVD, we have to understand some properties of arbitrary matrices.

Theorem: Let A be an $m \times n$ matrix.

1. The Rank of A, denoted Rank (A), is the number of linearly independent rows in A.
2. The Nullity of A, denoted Nullity (A), is $n - Rank(A)$ and describes the largest set of linearly independent vectors v in R^n for which $Av = 0$.

The Rank and Nullity of a matrix are playing such an important role to describe the behavior of the matrix. For instant, for the square matrix the matrix is invertible if and only if its Nullity is 0 and its Rank is the same as the size of the matrix.

Theorem: The number of linearly independent rows of an $m \times n$ matrix A is the same as the number of linearly independent columns of A.

For the square matrices, the matrix $A^tA(n \times n) and\ AA^t(m \times m)$

Theorem: Let A be an $m \times n$ matrix.

The matrices $A^tA\ and\ AA^t$ are symmetric.

1. Nullity (A)= Nullity (A^tA)
2. Rank (A)= Rank (A^tA)
3. The eigenvalue of A^tA are real and nonnegative.
4. The nonzero eigenvalues of AA^t are the same as the nonzero eigenvalues of A^tA.

In our research, SVD is used as a powerful tool to help us to reduce dimension of matrix. SVD shows how the stretch and rotation of operation is. For example, let the set of vectors $v_j \in$

R^n of unit length that describe a sphere. Next, we multiply the unit vectors v_j with a rectangular matrix $A \in R^{mxn}$, then we will have an ellipse that represents by the unit vectors $u_j$and magnitudes σ_j. We use the SVD to see how matrix A stretch in the directions of the axes of the ellipse.

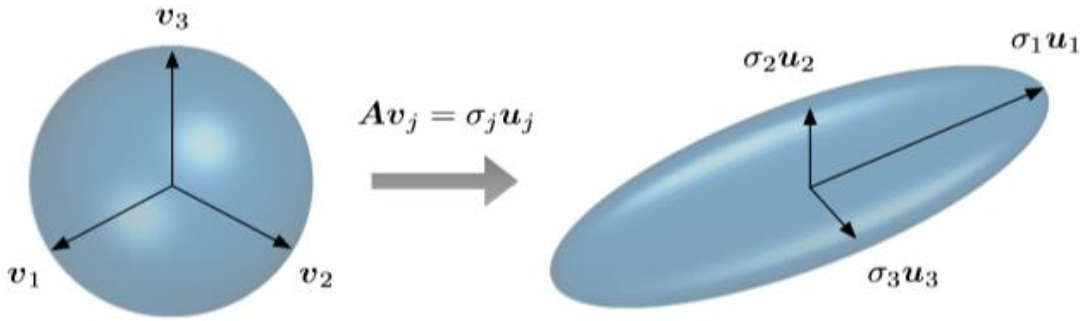

Figure 4. 2 Graphical representation of singular value decomposition transforming a unit radius sphere, described by right singular vectors v_j, to an ellipse (ellipsoid) with semiaxes characterized by the left singular vectors u_j and magnitude captured by the singular values σ_j[18].

$$Av_j = \sigma_j u_j$$

Where $A \in C^{mxn}, v_j \in C^n \; and \; u_j \in C^m$,

In the matrix form, based on the above formula we have

$$AV = U\sum$$

$$AVV^* = U\sum V^*$$

$$AI = U\sum V^*$$

$$A = U\sum V^*$$

Where $V^* = V^{-1}$ with "*" demotes the conjugate transpose.

$U = [u_1\ u_2\ u_3\ \ldots u_m] \in C^{m\times m}\ and\ U$ is an $m \times m$ orthogonal matrix,

$$U^*U = I_m$$

$V = [v_1 v_2\ v_3 \ldots v_n] \in C^{n\times n}\ and\ \ V$ is an $n \times n$ orthogonal matrix,

$$V^*V = I_n$$

Where U, V are a unitary matrices,

$\sum \in R^{mxn}$ is a diagonal matrix with $\sigma_1 \geq \sigma_2 \geq \sigma_3 \geq \cdots \geq \sigma_r \geq 0\ with\ r = \min(m, n)$

The column vectors $u_j\ of\ U, v_j\ of\ V$ are called the left and right singular vectors. The number of nonzero singular values is equal to the rank of the matrix A. The singular value decomposition plays an important role in numerical linear algebra.

$$A = \begin{bmatrix} | & | & | \\ A_1 & A_2 \ldots & A_m \\ | & | & | \end{bmatrix}_{n\times m}$$

$$U = \begin{bmatrix} | & | & | \\ u_1 & u_2 \ldots & u_m \\ | & | & | \end{bmatrix}_{m\times m}$$

$$V = \begin{bmatrix} | & | & | \\ v_1 & v_2 \ldots & v_n \\ | & | & | \end{bmatrix}_{n\times n}$$

$$\sum = \begin{bmatrix} \sigma_1 & 0 & \cdots & 0 \\ 0 & \sigma_2 & \cdots & 0 \\ \vdots & \vdots & \ddots & \vdots \\ 0 & 0 & 0 & \sigma_n \\ 0 & 0 & 0 & 0 \\ \vdots & \vdots & \vdots & \vdots \\ 0 & 0 & 0 & 0 \end{bmatrix}_{m \times n}$$

$$A = U \sum V^*$$

$$A = \begin{bmatrix} | & | & | \\ u_1 & u_2 \ldots & u_m \\ | & | & | \end{bmatrix}_{m \times m} \begin{bmatrix} \sigma_1 & 0 & \cdots & 0 \\ 0 & \sigma_2 & \cdots & 0 \\ \vdots & \vdots & \ddots & \vdots \\ 0 & 0 & 0 & \sigma_n \\ 0 & 0 & 0 & 0 \\ \vdots & \vdots & \vdots & \vdots \\ 0 & 0 & 0 & 0 \end{bmatrix}_{m \times n} \begin{bmatrix} | & | & | \\ v_1 & v_2 \ldots & v_n \\ | & | & | \end{bmatrix}^*_{n \times n}$$

$$A = \sum_{k=1}^{n} \sigma_k u_k v_k^*$$

$$A = \sigma_1 u_1 v_1^* (mode1) + \sigma_2 u_2 v_2^* (mode2) + \sigma_3 u_3 v_3^* (mode3) + \cdots + \sigma_n u_n v_n^* (mode\ n)$$

$$A = \begin{bmatrix} \sigma_1 u_{11} v_{11} & \sigma_1 u_{11} v_{21} & \sigma_1 u_{11} v_{31} & \ldots & \sigma_1 u_{11} v_{n-11} & \sigma_1 u_{11} v_{n1} \\ \sigma_1 u_{21} v_{11} & \sigma_1 u_{21} v_{21} & \sigma_1 u_{21} v_{31} & \ldots & \sigma_1 u_{21} v_{n-11} & \sigma_1 u_{21} v_{n1} \\ \sigma_1 u_{31} v_{11} & \sigma_1 u_{31} v_{21} & \sigma_1 u_{31} v_{31} & \ldots & \sigma_1 u_{31} v_{n-11} & \sigma_1 u_{31} v_{n1} \\ \sigma_1 u_{41} v_{11} & \sigma_1 u_{41} v_{21} & \sigma_1 u_{41} v_{31} & \ldots & \sigma_1 u_{41} v_{n-11} & \sigma_1 u_{41} v_{n1} \\ \vdots & \vdots & \vdots & \ldots & \vdots & \vdots \\ \sigma_1 u_{m1} v_{11} & \sigma_1 u_{m1} v_{21} & \sigma_1 u_{m1} v_{31} & \ldots & \sigma_1 u_{m1} v_{n-11} & \sigma_1 u_{m1} v_{n1} \end{bmatrix}$$

$$+ \begin{bmatrix} \sigma_2 u_{11} v_{11} & \sigma_2 u_{11} v_{21} & \sigma_2 u_{11} v_{31} & \ldots & \sigma_2 u_{11} v_{n-11} & \sigma_2 u_{11} v_{n1} \\ \sigma_2 u_{21} v_{11} & \sigma_2 u_{21} v_{21} & \sigma_2 u_{21} v_{31} & \ldots & \sigma_2 u_{21} v_{n-11} & \sigma_2 u_{21} v_{n1} \\ \sigma_2 u_{31} v_{11} & \sigma_2 u_{31} v_{21} & \sigma_2 u_{31} v_{31} & \ldots & \sigma_2 u_{31} v_{n-11} & \sigma_2 u_{31} v_{n1} \\ \sigma_2 u_{41} v_{11} & \sigma_2 u_{41} v_{21} & \sigma_2 u_{41} v_{31} & \ldots & \sigma_2 u_{41} v_{n-11} & \sigma_2 u_{41} v_{n1} \\ \vdots & \vdots & \vdots & \ldots & \vdots & \vdots \\ \sigma_2 u_{m1} v_{11} & \sigma_2 u_{m1} v_{21} & \sigma_2 u_{m1} v_{31} & \ldots & \sigma_2 u_{m1} v_{n-11} & \sigma_2 u_{m1} v_{n1} \end{bmatrix}$$

$$+\begin{bmatrix} \sigma_3 u_{11} v_{11} & \sigma_3 u_{11} v_{21} & \sigma_3 u_{11} v_{31} & \dots & \sigma_3 u_{11} v_{n-11} & \sigma_3 u_{11} v_{n1} \\ \sigma_3 u_{21} v_{11} & \sigma_3 u_{21} v_{21} & \sigma_3 u_{21} v_{31} & \dots & \sigma_3 u_{21} v_{n-11} & \sigma_3 u_{21} v_{n1} \\ \sigma_3 u_{31} v_{11} & \sigma_3 u_{31} v_{21} & \sigma_3 u_{31} v_{31} & \dots & \sigma_3 u_{31} v_{n-11} & \sigma_3 u_{31} v_{n1} \\ \sigma_3 u_{41} v_{11} & \sigma_3 u_{41} v_{21} & \sigma_3 u_{41} v_{31} & \dots & \sigma_3 u_{41} v_{n-11} & \sigma_3 u_{41} v_{n1} \\ \vdots & \vdots & \vdots & \dots & \vdots & \vdots \\ \sigma_3 u_{m1} v_{11} & \sigma_3 u_{m1} v_{21} & \sigma_3 u_{m1} v_{31} & \dots & \sigma_3 u_{m1} v_{n-11} & \sigma_3 u_{m1} v_{n1} \end{bmatrix}$$

...

$$+\begin{bmatrix} \sigma_r u_{11} v_{11} & \sigma_r u_{11} v_{21} & \sigma_r u_{11} v_{31} & \dots & \sigma_r u_{11} v_{n-11} & \sigma_r u_{11} v_{n1} \\ \sigma_r u_{21} v_{11} & \sigma_r u_{21} v_{21} & \sigma_r u_{21} v_{31} & \dots & \sigma_r u_{21} v_{n-11} & \sigma_r u_{21} v_{n1} \\ \sigma_r u_{31} v_{11} & \sigma_r u_{31} v_{21} & \sigma_r u_{31} v_{31} & \dots & \sigma_r u_{31} v_{n-11} & \sigma_r u_{31} v_{n1} \\ \sigma_r u_{41} v_{11} & \sigma_r u_{41} v_{21} & \sigma_r u_{41} v_{31} & \dots & \sigma_r u_{41} v_{n-11} & \sigma_r u_{41} v_{n1} \\ \vdots & \vdots & \vdots & \dots & \vdots & \vdots \\ \sigma_r u_{m1} v_{11} & \sigma_r u_{m1} v_{21} & \sigma_r u_{m1} v_{31} & \dots & \sigma_r u_{m1} v_{n-11} & \sigma_r u_{m1} v_{n1} \end{bmatrix}$$

$$A \approx \begin{bmatrix} | & | & | \\ u_1 & u_2 \dots & u_r \\ | & | & | \end{bmatrix}_{m \times r} \begin{bmatrix} \sigma_1 & 0 & \dots & 0 \\ 0 & \sigma_2 & \dots & 0 \\ \vdots & \vdots & \ddots & \vdots \\ 0 & 0 & 0 & \sigma_r \end{bmatrix}_{r \times r} \begin{bmatrix} | & | & | \\ v_1 & v_2 \dots & v_r \\ | & | & | \end{bmatrix}^*_{r \times n}$$

$$A = \sum_{k=1}^{r} \sigma_k u_k v_k^*$$

$$A \approx \sigma_1 u_1 v_1^* (mode1) + \sigma_2 u_2 v_2^* (mode2) + \sigma_3 u_3 v_3^* (mode3) + \cdots + \sigma_r u_r v_r^* (mode\ r)$$

$$A \approx \begin{bmatrix} \sigma_1 u_{11} v_{11} & \sigma_1 u_{11} v_{21} & \sigma_1 u_{11} v_{31} & \dots & \sigma_1 u_{11} v_{r-11} & \sigma_1 u_{11} v_{r1} \\ \sigma_1 u_{21} v_{11} & \sigma_1 u_{21} v_{21} & \sigma_1 u_{21} v_{31} & \dots & \sigma_1 u_{21} v_{r-11} & \sigma_1 u_{21} v_{r1} \\ \sigma_1 u_{31} v_{11} & \sigma_1 u_{31} v_{21} & \sigma_1 u_{31} v_{31} & \dots & \sigma_1 u_{31} v_{r-11} & \sigma_1 u_{31} v_{r1} \\ \sigma_1 u_{41} v_{11} & \sigma_1 u_{41} v_{21} & \sigma_1 u_{41} v_{31} & \dots & \sigma_1 u_{41} v_{r-11} & \sigma_1 u_{41} v_{r1} \\ \vdots & \vdots & \vdots & \dots & \vdots & \vdots \\ \sigma_1 u_{m1} v_{11} & \sigma_1 u_{m1} v_{21} & \sigma_1 u_{m1} v_{31} & \dots & \sigma_1 u_{m1} v_{r-11} & \sigma_1 u_{m1} v_{r1} \end{bmatrix}$$

$$+\begin{bmatrix} \sigma_2 u_{11} v_{11} & \sigma_2 u_{11} v_{21} & \sigma_2 u_{11} v_{31} & \dots & \sigma_2 u_{11} v_{r-11} & \sigma_2 u_{11} v_{r1} \\ \sigma_2 u_{21} v_{11} & \sigma_2 u_{21} v_{21} & \sigma_2 u_{21} v_{31} & \dots & \sigma_2 u_{21} v_{r-11} & \sigma_2 u_{21} v_{r1} \\ \sigma_2 u_{31} v_{11} & \sigma_2 u_{31} v_{21} & \sigma_2 u_{31} v_{31} & \dots & \sigma_2 u_{31} v_{r-11} & \sigma_2 u_{31} v_{r1} \\ \sigma_2 u_{41} v_{11} & \sigma_2 u_{41} v_{21} & \sigma_2 u_{41} v_{31} & \dots & \sigma_2 u_{41} v_{r-11} & \sigma_2 u_{41} v_{r1} \\ \vdots & \vdots & \vdots & \dots & \vdots & \vdots \\ \sigma_2 u_{m1} v_{11} & \sigma_2 u_{m1} v_{21} & \sigma_2 u_{m1} v_{31} & \dots & \sigma_2 u_{m1} v_{r-11} & \sigma_2 u_{m1} v_{r1} \end{bmatrix}$$

$$+\begin{bmatrix} \sigma_3 u_{11} v_{11} & \sigma_3 u_{11} v_{21} & \sigma_3 u_{11} v_{31} & \dots & \sigma_3 u_{11} v_{r-11} & \sigma_3 u_{11} v_{r1} \\ \sigma_3 u_{21} v_{11} & \sigma_3 u_{21} v_{21} & \sigma_3 u_{21} v_{31} & \dots & \sigma_3 u_{21} v_{r-11} & \sigma_3 u_{21} v_{r1} \\ \sigma_3 u_{31} v_{11} & \sigma_3 u_{31} v_{21} & \sigma_3 u_{31} v_{31} & \dots & \sigma_3 u_{31} v_{r-11} & \sigma_3 u_{31} v_{r1} \\ \sigma_3 u_{41} v_{11} & \sigma_3 u_{41} v_{21} & \sigma_3 u_{41} v_{31} & \dots & \sigma_3 u_{41} v_{r-11} & \sigma_3 u_{41} v_{r1} \\ \vdots & \vdots & \vdots & \dots & \vdots & \vdots \\ \sigma_3 u_{m1} v_{11} & \sigma_3 u_{m1} v_{21} & \sigma_3 u_{m1} v_{31} & \dots & \sigma_3 u_{m1} v_{r-11} & \sigma_3 u_{m1} v_{r1} \end{bmatrix}$$

…

$$+\begin{bmatrix} \sigma_r u_{11} v_{11} & \sigma_r u_{11} v_{21} & \sigma_r u_{11} v_{31} & \dots & \sigma_r u_{11} v_{r-11} & \sigma_r u_{11} v_{r1} \\ \sigma_r u_{21} v_{11} & \sigma_r u_{21} v_{21} & \sigma_r u_{21} v_{31} & \dots & \sigma_r u_{21} v_{r-11} & \sigma_r u_{21} v_{r1} \\ \sigma_r u_{31} v_{11} & \sigma_r u_{31} v_{21} & \sigma_r u_{31} v_{31} & \dots & \sigma_r u_{31} v_{r-11} & \sigma_r u_{31} v_{r1} \\ \sigma_r u_{41} v_{11} & \sigma_r u_{41} v_{21} & \sigma_r u_{41} v_{31} & \dots & \sigma_r u_{41} v_{r-11} & \sigma_r u_{41} v_{r1} \\ \vdots & \vdots & \vdots & \dots & \vdots & \vdots \\ \sigma_r u_{m1} v_{11} & \sigma_r u_{m1} v_{21} & \sigma_r u_{m1} v_{31} & \dots & \sigma_r u_{m1} v_{r-11} & \sigma_r u_{m1} v_{r1} \end{bmatrix}$$

$$A = U\sum V^*$$

$$A^*A = (U\sum V^*)^* U\sum V^* = V\sum U^* U\sum V^* = V\sum I\sum V^* = V\sum^2 V^*$$

$$(A^*A)V = (V\sum^2 V^*)V = V\sum^2$$

$$AA^* = U\sum V^*(U\sum V^*)^* = U\sum V^* V\sum U^* = U\sum I\sum U^* = U\sum^2 U^*$$

$$AA^*U = (U\sum^2 U^*)U = U\sum^2$$

There are relations between eigenvalue and singular value decompositions A. Besides, the nonzero eigenvalues of $A^*A \; and \; AA^*$ are the square of the nonzero singular values of A. Thus, we can use the eigenvalue decomposition of $A^*A \; and \; AA^*$ to solve for singular vector and singular value of A instead of using SVD. SVD is more efficient and powerful tool to decompose the large square matrix because of the runoff error on formula of $A^*A \; and \; AA^*$ to destroy applicable information. However, to decompose the smaller square matrix and to save the cost the eigenvalue decomposition of $A^*A \; and \; AA^*$ is the best choice for majority researchers.

4.3 POD method

POD is a commonly used technique in data analysis including turbulent flow, that has become very popular as a result of the recent quick growth in computing power [19]. The sum of the product of corresponding temporal coefficient and its modes represents the fluctuation in the actual turbulent flow field $q(\xi, t)$ without mean $\bar{q}(\xi)$ over three dimensions [18]:

$$x(t) = q(\xi, t) - \bar{q}(\xi) = \sum_j a_j(t)\, \phi_j(\xi) \in \mathbb{R}^m \ (t = t_1, t_2, t_3, \dots, t_n),$$

Where $a_j(t)$ represents temporal coefficient of a set of orthogonal modes $\phi_j(\xi)$. Here,

$\phi_j(\xi)$ represents POD's modes and $\xi$is the spatial vector.

$x(t)$ represents a snapshot at time t

Searching for the best basis vector to represent $q(\xi)$ is the priority goal of the POD method in the turbulent flow field. Finding eigenvectors ϕ_j and eigenvalues λ_j to solve this problem.

$$R\phi_j = \lambda_j \phi_j \qquad (j = 1,2,3, \dots, n)$$

$$R = \sum_{i=1}^{m} x(t_i) x^T(t_i) = XX^T \in \mathbb{R}^{m \times m} \ ,$$

where R is the covariance matrix of vector $x(t)$,

X is a matrix form which is stacked of n snapshots into a matrix,

$$X = [x(t_1)\ x(t_2)\ x(t_3)\ \dots\ x(t_n)] \in R^{m \times n},$$

$\phi_j \in \mathbb{R}^m and\ \lambda_j (\lambda_1 \geq \lambda_2 \geq \lambda_3 \geq \cdots \lambda_n \geq 0)$ are the eigenvectors and eigenvalues of covariance matrix of vector $x(t)$ respectably,

In this research, rectangular matrix X will be decomposed directly with the singular-value-decomposition (SVD) method to find left and right singular vectors.

$$\mathrm{X} = \Phi\sum\Psi^{T}$$

$$\begin{bmatrix} | & | & | \\ \mathrm{x}_1 & \mathrm{x}_2 \ldots & \mathrm{x}_\mathrm{n} \\ | & | & | \end{bmatrix}_{\mathrm{m}\times\mathrm{n}} = \begin{bmatrix} | & | & | \\ \phi_1 & \phi_2 \ldots & \phi_m \\ | & | & | \end{bmatrix}_{m\times m} \begin{bmatrix} \sigma_1 & 0 & \cdots & 0 \\ 0 & \sigma_2 & \cdots & 0 \\ \vdots & \vdots & \ddots & \vdots \\ 0 & 0 & 0 & \sigma_n \\ 0 & 0 & 0 & 0 \\ \vdots & \vdots & \vdots & \vdots \\ 0 & 0 & 0 & 0 \end{bmatrix}_{m\times n} \begin{bmatrix} | & | & | \\ \psi_1 & \psi_2 \ldots & \psi_n \\ | & | & | \end{bmatrix}^{T}_{n\times n}$$

Here, m is a number of spatial points, n is a number of snapshot (time step) ($m \gg n$)

$\Phi = [\phi_1\ \phi_2\ \phi_3\ \ldots \phi_m]$ is an $m \times m$ orthogonal matrix and the matrix Φ contains the left singular vectors of X.

$\Psi = [\psi_1\ \psi_2\ \psi_3\ \ldots \psi_n]$ is an $n \times n$ orthogonal matrix and matrix Ψ contains the right singular vectors of X.

$\sum$ is an $m \times n$ diagonal matrix where all elements are zero except for the diagonal elements $\sum_{ii} = \sigma_i \geq 0\ and\ \sigma_1 \geq \sigma_2 \geq \sigma_3 \geq \cdots \sigma_n \geq 0$

$$X = \sum_{k=1}^{n} \sigma_k \phi_k \psi_k^T$$

$$X = \sigma_1\phi_1\psi_1^T(mode1) + \sigma_2\phi_2\psi_2^T(mode2) + \sigma_3\phi_3\psi_3^T(mode3) + \cdots + \sigma_n\phi_n\psi_n^T(mode\ n)$$

$$\mathrm{XX^T} = (\Phi\sum\Psi^{\mathrm{T}})(\Phi\sum\Psi^{\mathrm{T}})^{\mathrm{T}}$$

$$\mathrm{XX^T} = \Phi\sum\Psi^{\mathrm{T}}\Psi\sum\Phi^{\mathrm{T}} = \Phi\sum^2\Phi^{\mathrm{T}}$$

$$\mathrm{XX^T}\Phi = \Phi\sum^2$$

$$X^{T}X = (\Phi\sum\Psi^{T})^{T}(\Phi\sum\Psi^{T})$$

$$X^{T}X = \Psi\sum\Phi^{T}\Phi\sum\Psi^{T} = \Psi\sum^{2}\Psi^{T}$$

$$X^{T}X\Psi = \Psi\sum^{2}$$

Thus, we can conclude that the left and the right singular vectors of X are also the orthogonal eigenvectors of XX^T, X^TX. [18]. Thus, we just consider the singular value decomposition to get the modes.

$$\sum^{2} = \begin{bmatrix} \lambda_1 & 0 & \cdots & 0 \\ 0 & \lambda_2 & \cdots & 0 \\ \vdots & \vdots & \ddots & \vdots \\ 0 & 0 & 0 & \lambda_n \\ 0 & 0 & 0 & 0 \\ \vdots & \vdots & \vdots & \vdots \\ 0 & 0 & 0 & 0 \end{bmatrix}_{m\times n} = \begin{bmatrix} \sigma_1^2 & 0 & \cdots & 0 \\ 0 & \sigma_2^2 & \cdots & 0 \\ \vdots & \vdots & \ddots & \vdots \\ 0 & 0 & 0 & \sigma_n^2 \\ 0 & 0 & 0 & 0 \\ \vdots & \vdots & \vdots & \vdots \\ 0 & 0 & 0 & 0 \end{bmatrix} => \sigma_i = \sqrt{\lambda_i}$$
$$m\times n$$

The relationship between the singular value and the eigenvalue is known as the singular value square is equal to the eigenvalue problem ($\delta_j^2 = \lambda_j$). That mean SVD apply directly on matrix X to find the POD modes Φ. If singular values of POD are ordered from largest to smallest, then POD modes are also arranged from most to least important in capturing the cumulative energy of the turbulent flow field. The value of r below is determined by how many percentages of total cumulative energy that is used to reconstruct correctly the original structures. The new model can represent the flow field after determining r which is the approximate number of modes used for reconstruction.

$$q(\xi, t) - \bar{q}(\xi) \approx \sum_{j=1}^{r} a_j\,(t)\phi_j(\xi)$$

$$X \approx \begin{bmatrix} | & | & | \\ \phi_1 & \phi_2 \dots & \phi_r \\ | & | & | \end{bmatrix}_{m\times r} \begin{bmatrix} \sigma_1 & 0 & \cdots & 0 \\ 0 & \sigma_2 & \cdots & 0 \\ \vdots & \vdots & \ddots & \vdots \\ 0 & 0 & 0 & \sigma_r \end{bmatrix}_{r\times r} \begin{bmatrix} | & | & | \\ \psi_1 & \psi_2 \dots & \psi_n \\ | & | & | \end{bmatrix}^T_{r\times n} \quad r \ll n$$

The cumulative energy of snapshot:

$$0 < \varepsilon(\mathrm{r}) = \frac{\sum_{\mathrm{j}=1}^{\mathrm{r}} \sigma_{\mathrm{j}}^2}{\sum_{\mathrm{j}=1}^{\mathrm{n}} \sigma_{\mathrm{j}}^2} < 1$$

Where $\sum_{j=1}^{r} \sigma_j^2$ is the sum of r singular values square, and $\sum_{j=1}^{n} \sigma_j^2$ is the sum of all singular values square. Utility of POD's singular values can use to determine the amount of r modes needed to express the flow field's fluctuation.

$$X \approx \sum_{k=1}^{r} \sigma_k \phi_k \psi_k^T$$

$$X \approx \sigma_1\phi_1\psi_1^T(mode1) + \sigma_2\phi_2\psi_2^T(mode2) + \sigma_3\phi_3\psi_3^T(mode3) + \cdots + \sigma_r\phi_r\psi_r^T(mode\ r)$$

The temporal coefficient can be defined as:

$$a_j(t) = \langle q(\xi,t) - \bar{q}(\xi), \phi_j(\xi)\rangle = \langle x(t), \phi_j\rangle$$

Where a_j is the time coefficient of each POD mode ϕ_j

4.4 POD for coherent structure after the wake of MVG

4.4.1 Discussion on vortex structure of MVG wake by using velocity as an input

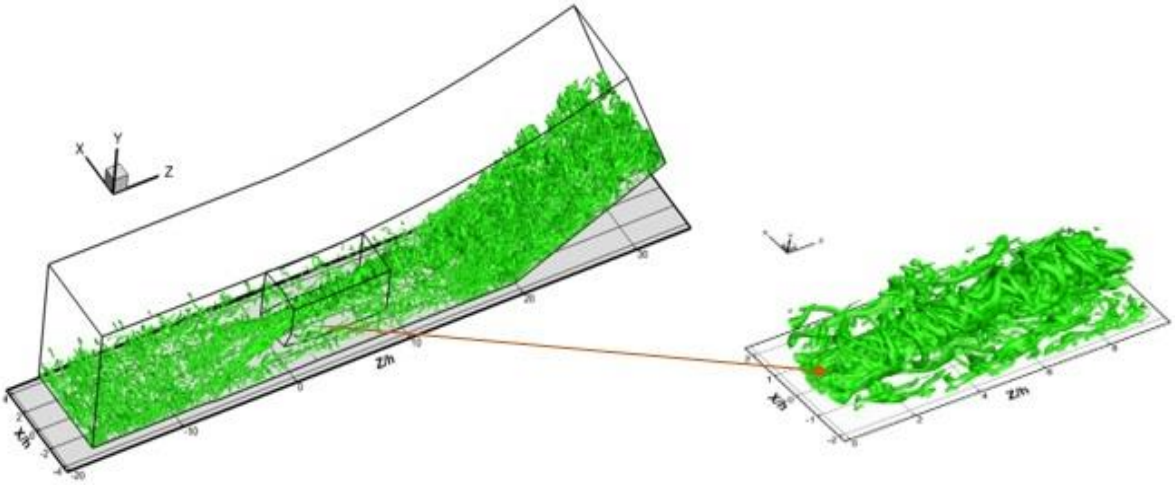

Figure 4. 3 Vortex Structure of $\tilde{\Omega}_R$in (iso-surface of $\tilde{\Omega}_R$ =0.52) in MVG wake

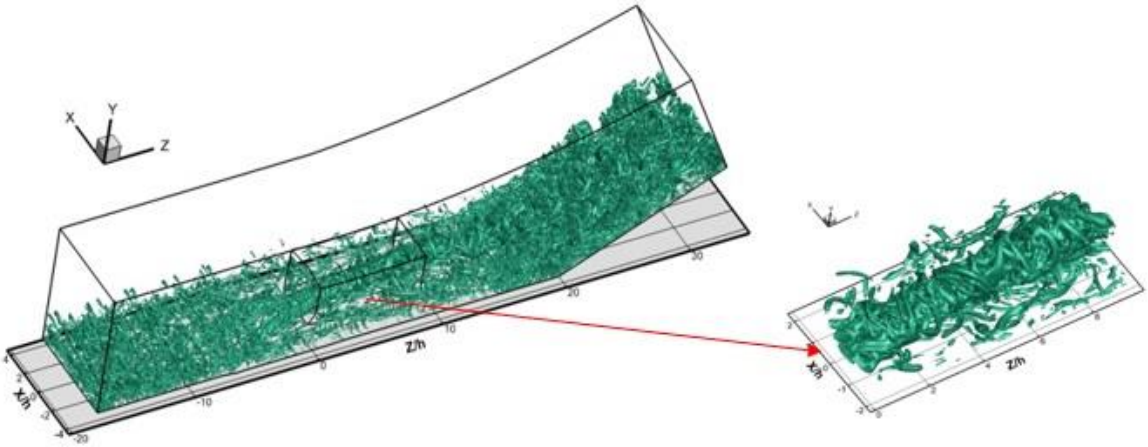

Figure 4. 4 Vortex Structure of Liutex (iso-surface of Liutex=0.05) in MVG wake

The grid size of the subzone is $200 \times 110 \times 71$. The number of snapshots is 120. The physical time step is equal to 4.706×10^{-8} s and the time interval between two successive snapshots is equal to 250 physical time steps. The input variables are fluctuation velocity components which result in a 4686000×120 matrix.

Table 4. 1 Parameters of subzone

	Start location	End location
x/h	-1.99	2.40
y/h	0	3.31
z/h	3.31	9.37

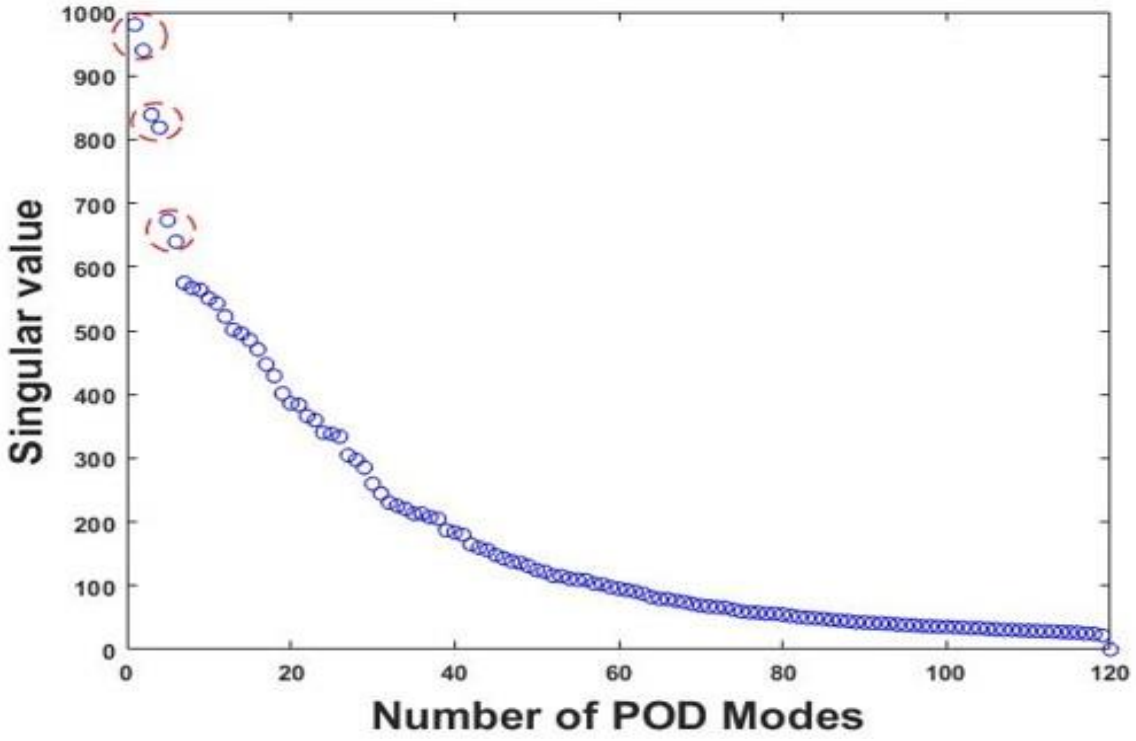

Figure 4. 5 Singular value of matrix X for 120 POD modes using velocity

In figure 4.5, the singular value of matrix X is shown in descending order and there are three pairs of POD modes. Two POD modes with similar singular values as shown in Table 4.2 are paired together. Table 4.3 shows the sum of L-magnitudes of the first 6 POD modes using velocity (u,v,w) as the input. First pair is modes 1-2 with strong primary vortices. Second and third pairs are modes 3-4 and modes 5-6, which are secondary vortices generated by MVG. All three pairs are caused by robust shear layer which generate spanwise vortex rings through K-H type

instability (also called K-H modes). Moreover, the pairing of POD modes is a common case, which is a sign of K-H type instability as theorized by Li and Liu.

Table 4. 2 Singular value of the first 6 POD modes using velocity (u, v, w) as an input

	Mode 1	Mode 2	Mode 3	Mode 4	Mode 5	Mode 6
Singular Value	980.2	939.7	838.7	818.6	637	639.5

Table 4. 3 Sum of Cumulative Energy of the first 6 POD modes using velocity (u, v, w) as an input

	Mode 1	Mode 2	Mode 3	Mode 4	Mode 5	Mode 6
Cumulative Energy	10	9.2	7.32	6.98	4.72	4.26

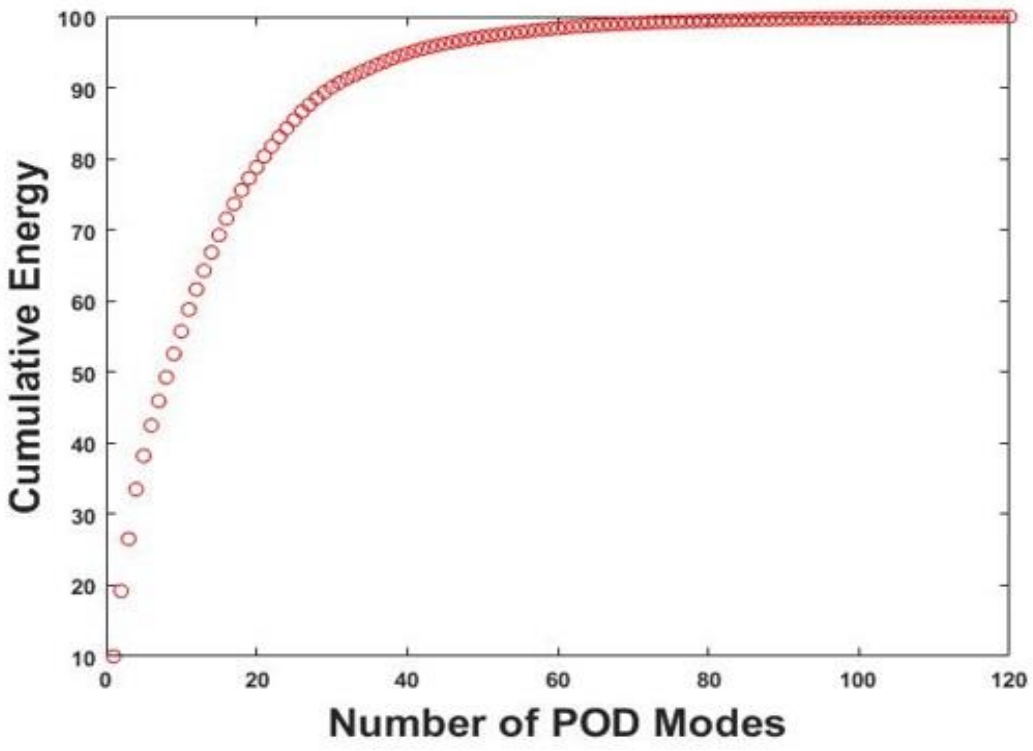

Figure 4. 6 Cumulative Energy for 120 POD modes using velocity

Mode 1 contains 10% of total cumulative L-magnitudes, which is the highest L-magnitudes amount compared to the other POD modes. Figure 4.6 shows that the difference of cumulative L-magnitudes between two consecutives modes is decreasing, which indicates that low order modes have more L-magnitudes than high order modes. As shown in figure 4.7, the structure of mode 1 is smaller than the structure of mode 3 although the L-magnitude of mode 1 is higher than the one of mode 3. Moreover, mode 5 has higher L-magnitude than mode 6, but the structure of mode 5 is smaller than mode 6. Therefore, we can conclude the relative strength of rotation ($\tilde{\Omega}_R$) is not correlated with cumulative L-magnitudes.

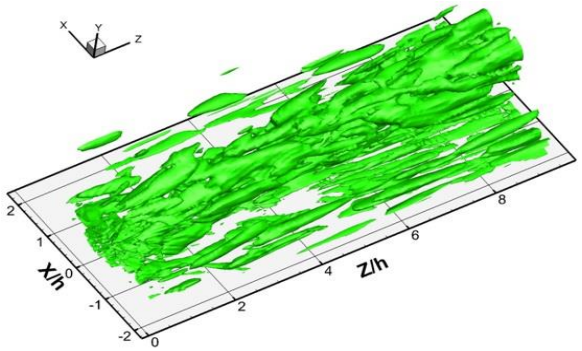

Mode 1

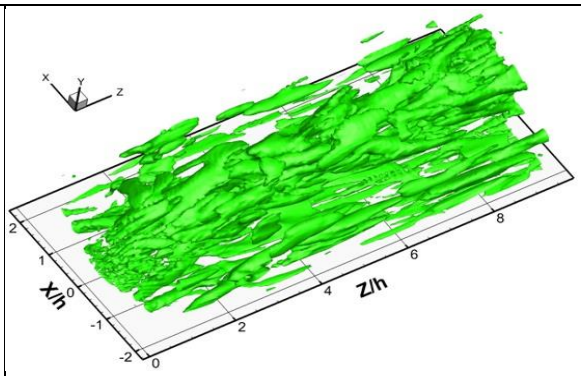

Mode2

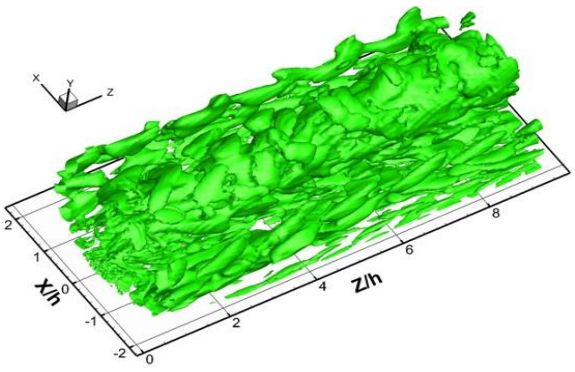

Mode 3

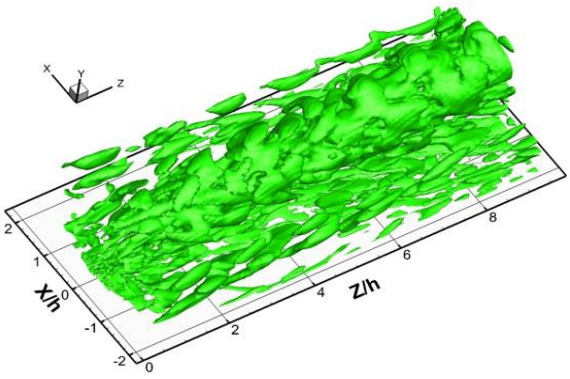

Mode 4

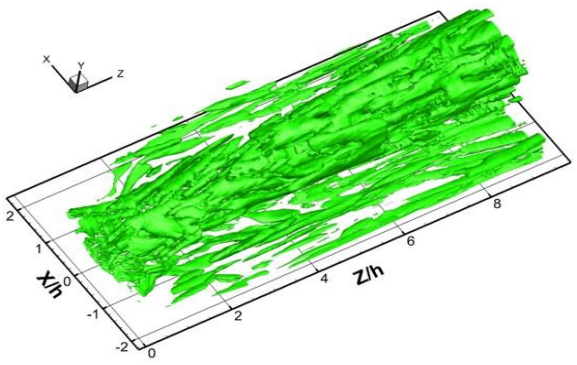

Mode 5

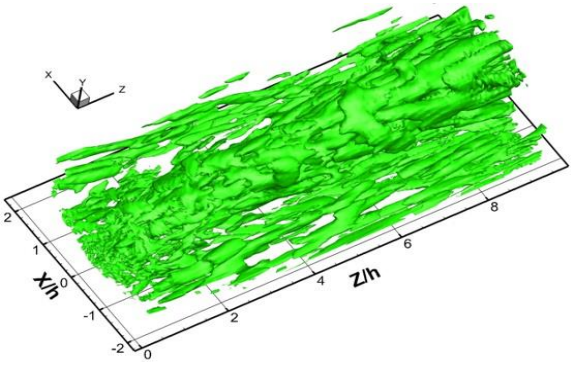

Mode 6

Figure 4. 7 Vortex structures (iso-surface of $\tilde{\Omega}_R$ = 0.52) of the first 6 POD modes in the MVG wake.

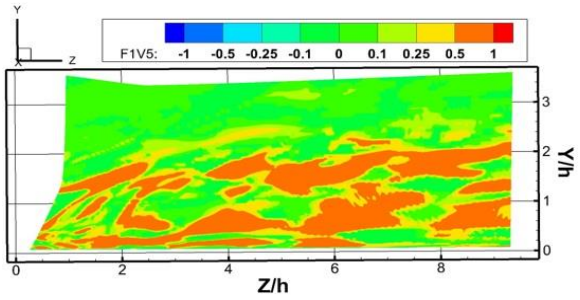

Mode 1

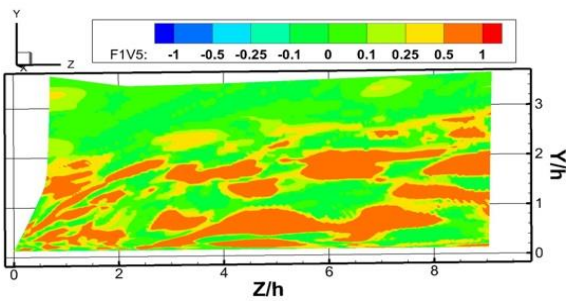

Mode 2

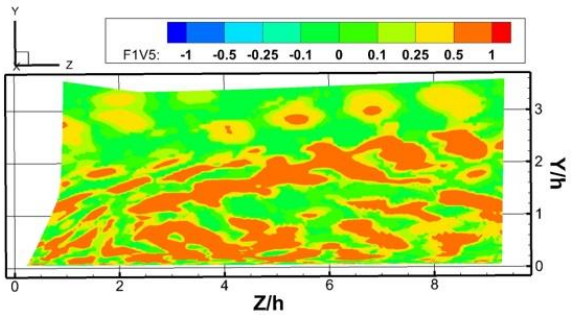

Mode 3

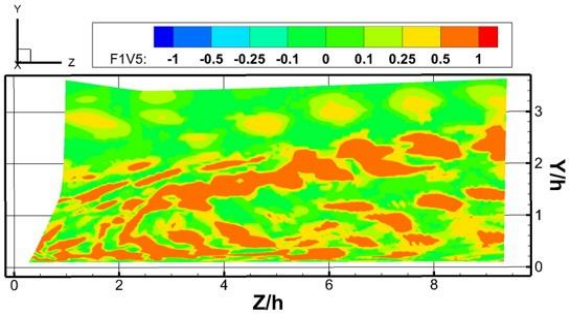

Mode 4

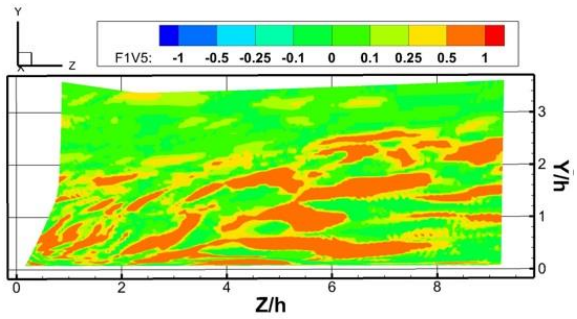

Mode 5

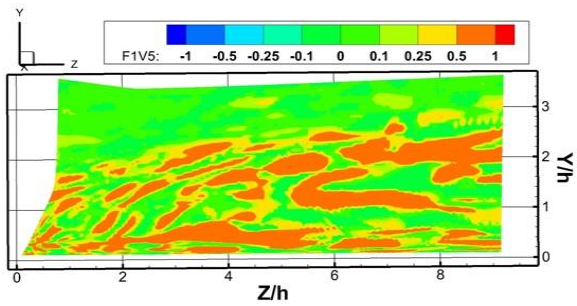

Mode 6

Figure 4. 8 The streamwise $\tilde{\Omega}_R$ vector distribution on the central plane

From Figure 4.8 above, we can see clearly that modes 1-2-5-6 are mainly dominated by streamwise characteristics. However, mode 3-4 have characteristics of spanwise vortex structure. Here, x-, y-, z- axes are defined as the spanwise, normal and streamwise directions, respectively.

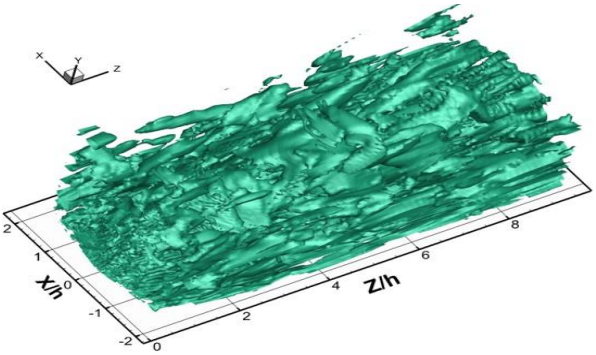

Mode 1

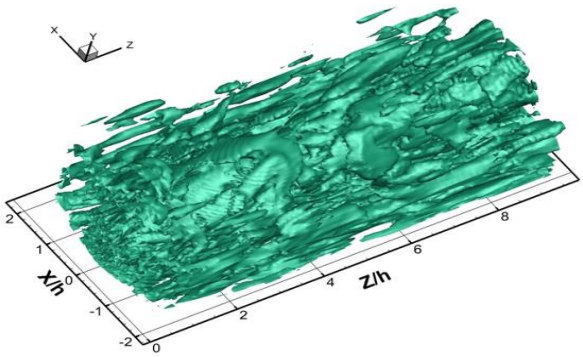

Mode 2

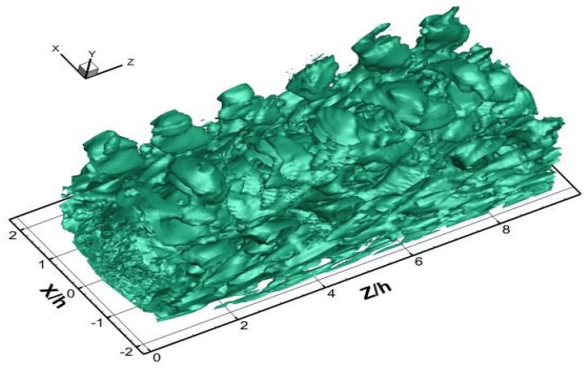

Mode 3

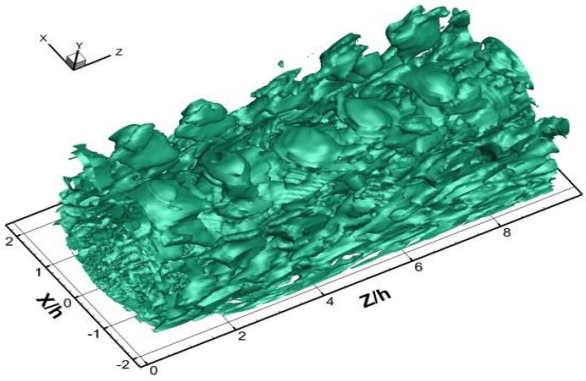

Mode 4

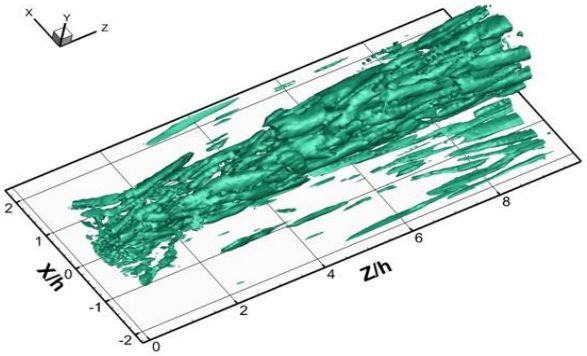

Mode 5

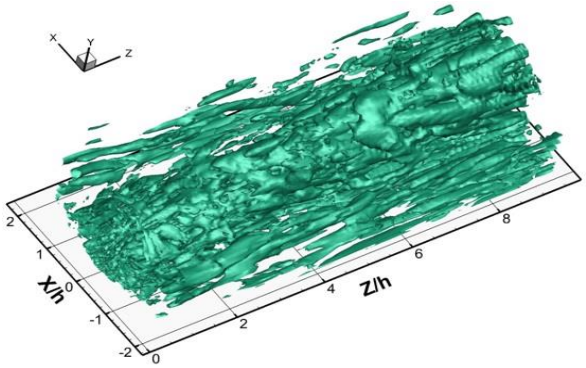

Mode 6

Figure 4. 9 Vortex structures (iso-surface of Liutex=0.05) of the first sixth POD modes in the MVG wake

By choosing iso-surfaces with a threshold Liutex=0.05, we can see the shape of the first 6 POD modes. $\tilde{\Omega}_R$ method is different from Liutex, because the former is contaminated by shear and the latter is not. As shown in figure 4.9, the structure of mode 5 is quite smaller than the structure of mode 6, but mode 5 has more L-magnitude than mode 6 as can be seen in Table 3. Thus, the absolute strength of rotation, or Liutex, is not correlated with cumulative L-magnitudes. Modes 1-2-5-6 are dominated by the fluctuation in the streamwise and mode 3-4 is strongly dominated by spanwise direction as can be seen in figure 4.10.

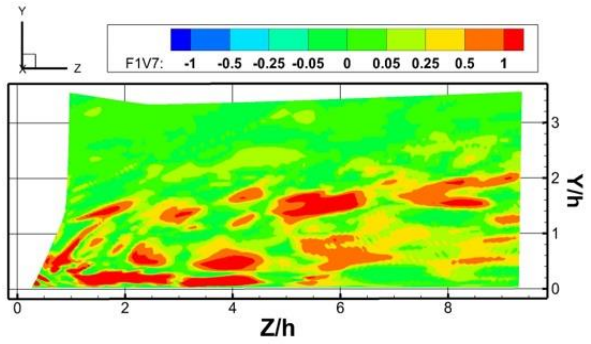

Mode 1

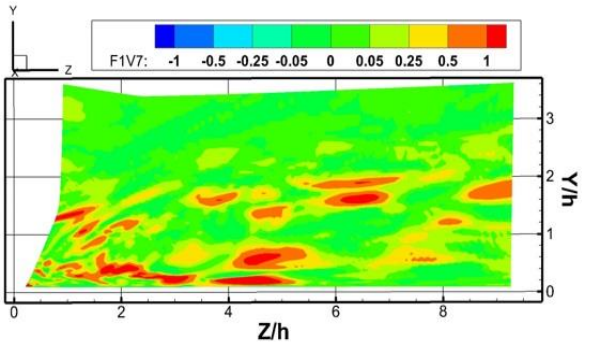

Mode 2

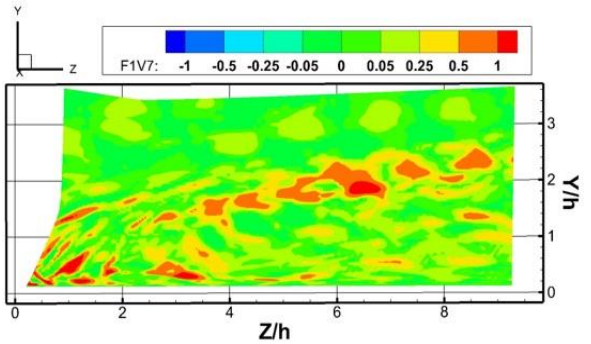

Mode 3

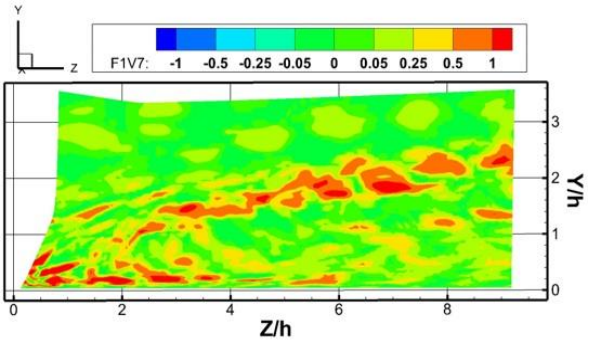

Mode 4

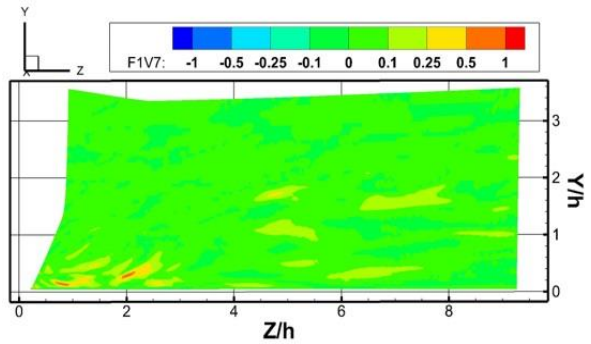

Mode 5

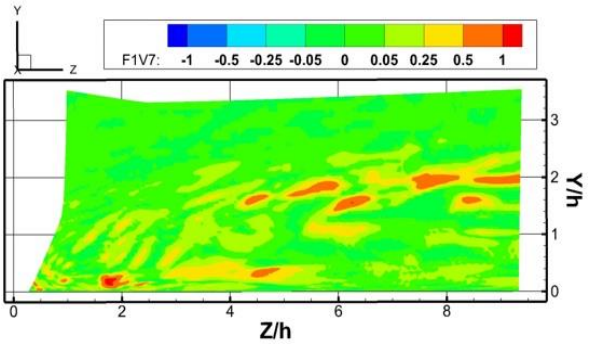

Mode 6

Figure 4. 10 The distribution of z-component of Liutex velocity distribution on the central plane using velocity as an input

In the above study, both the Liutex and $\tilde{\Omega}_R$ methods are used. The Liutex-Omega criterion uses the idea of the Omega method and Liutex to measure the relative rotation strength. So, it is not sensitive to the moderate change of threshold. Liutex is a measurement of the rigid rotation strength without shear and stretching contamination. However, it needs an appropriate threshold. The use of two methods depends on the specific cases. For the case where the strong vortices and weak vortices co-exist, it is recommended to apply modified $\tilde{\Omega}_R$-criterion.

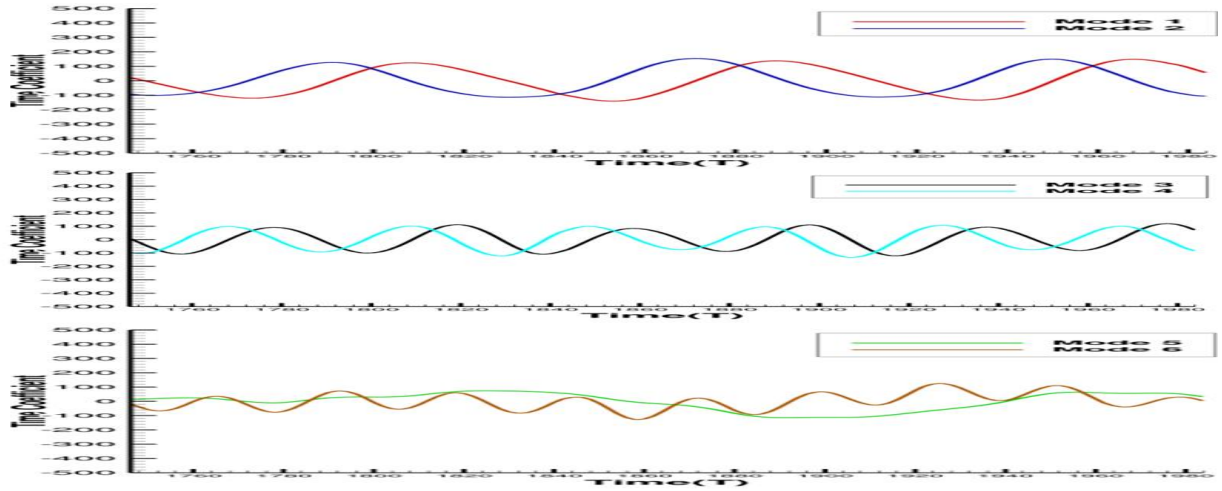

Figure 4. 11 Time coefficient of the first sixth POD modes.

Figure 4.11 shows times coefficient of the first six POD modes over 120 snapshots. Time coefficients of modes 1-2 and modes 3-4 have similar fluctuations. However, time coefficients of modes 5-6 has different fluctuations. Moreover, the period of modes 1-2 are larger than wavelength of modes 3-4 and modes 5-6.

When we use velocity (u, v, w) as an input directly, there is no correlation between either the relative strength $(\tilde{\Omega}_R)$ or absolute strength (Liutex) of rotation, and cumulative L-magnitudes. Now we will try to use $\tilde{\Omega}_R$ and Liutex as an input directly. Since $\tilde{\Omega}_R$ is just a scalar, not a vector, we then cannot load data directly from $\tilde{\Omega}_R$. However, Liutex is a vector, so we use Liutex vector

(L_x, L_y, L_z) as an input to check whether there is a correlation between Liutex and cumulative L-magnitudes.

4.4.2 Discussion on vortex structure of MVG wake by using Liutex vector ($L_x,\ L_y,\ L_z$) as an input directly

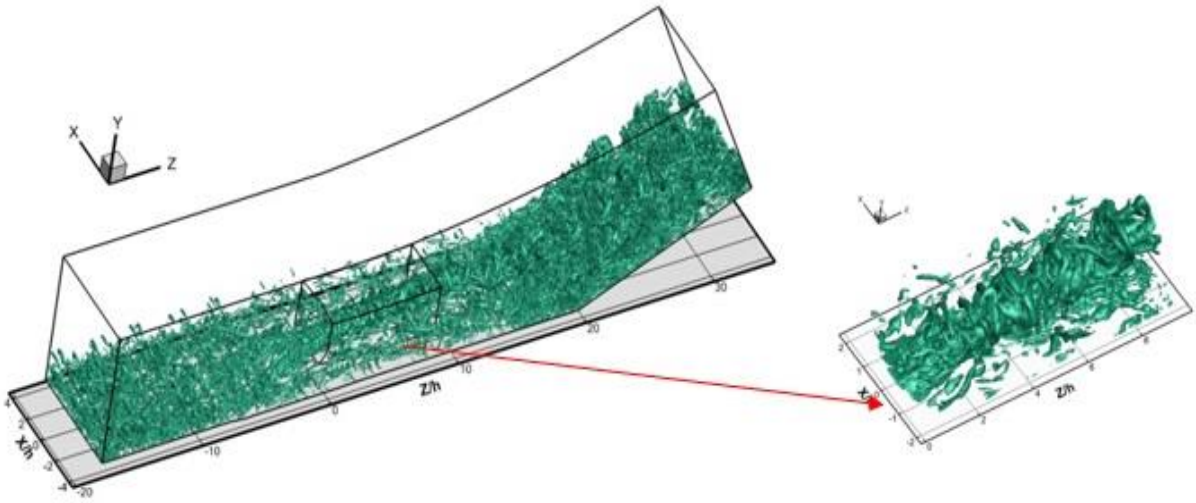

Figure 4. 12 Vortex Structure of Liutex in MVG wake

In this section, the POD method is performed by directly using Liutex vector as input. By definition, the magnitude of Liutex has the dimension of angular velocity. Therefore, as the singular values of POD using velocity stand for the kinetic energy of the turbulent flow field, the singular values of POD using Liutex vector represent angular kinetic energy which is closely related to rotation. The POD modes using velocity present the energy structures from the most dominant to the least dominant. But these obtained structures would not only contain the effect of rotation, but also shear and compression/stretching. By directly using Liutex vector as input, the POD modes would exclusively present the spatial structures of angular kinetic energy from the most dominant to the least dominant, correlated more closely to vortical motion. So, it

provides a new and different view to explore the dominant and coherent structures in the flow field.

Table 4. 4 Parameters of subzone

	Start location	End location
x/h	-1.99	2.40
y/h	0	3.31
z/h	3.31	9.37

The snapshot x_j is defined as,

$$x_j = \begin{pmatrix} L_{x_{571,1,35}}^{(j)} \\ \vdots \\ L_{x_{770,1,35}}^{(j)} \\ L_{x_{571,2,35}}^{(j)} \\ \vdots \\ L_{x_{770,2,35}}^{(j)} \\ \vdots \\ L_{x_{I,J,K}}^{(j)} \\ \vdots \\ L_{x_{771,1,35}}^{(j)} \\ \vdots \\ L_{y_{I,J,K}}^{(j)} \\ \vdots \\ L_{z_{I,J,K}}^{(j)} \\ \vdots \\ L_{z_{770,110,105}}^{(j)} \end{pmatrix} \text{ for } j = 1, \dots, 120$$

where ${L_x}^{(j)}$, ${L_y}^{(j)}$ and ${L_z}^{(j)}$ are fluctuation Liutex vector fields at $t = (1512 + 2j)T$ and $X = (x_1, x_2, x_3, .., x_{120}) \in R^{m \times n}$ $(m = 4686000,\ n = 120,\ 1T = 250)$.

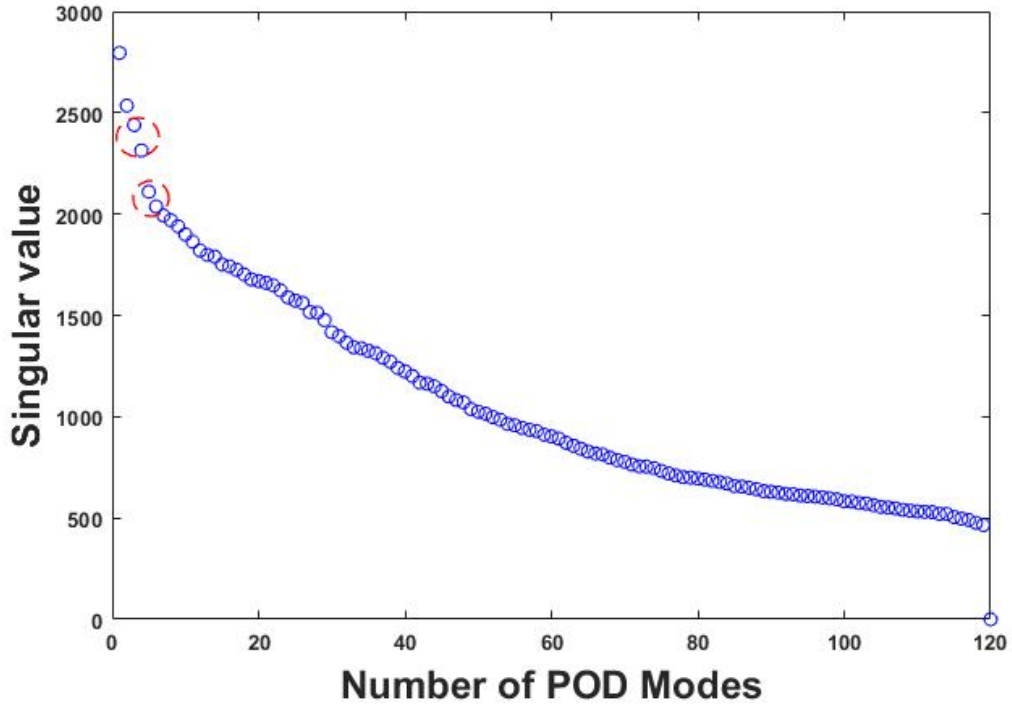

Figure 4. 13 Singular value of matrix X for 120 POD modes using Liutex vector $(L_x,\ L_y,\ L_z)$

From the singular value of matrix X above, there are two pairs of POD modes among the first sixth POD modes. Because of the significant difference between singular value of mode 1 and mode 2 (as shown in Table 4.5), those two modes are not considered a pair. Modes 3-4 and modes 5-6 have instead similar singular values, which are then paired. Modes 3-4 has strong primary vortices and modes 5-6 are secondary vortices. Pairs 3 and 4 are caused by the shear layer instability, which generate spanwise vortex rings through K-H type instability or K-H modes. The pairing of POD modes is a common case, which is a sign of K-H type instability.

Table 4. 5 Singular value of the first 6 POD modes using Liutex vector directly (L_x, L_y, L_z) as an input

	Mode 1	Mode 2	Mode 3	Mode 4	Mode 5	Mode 6
Singular Value	2795	2535	2439	2314	2110	2037

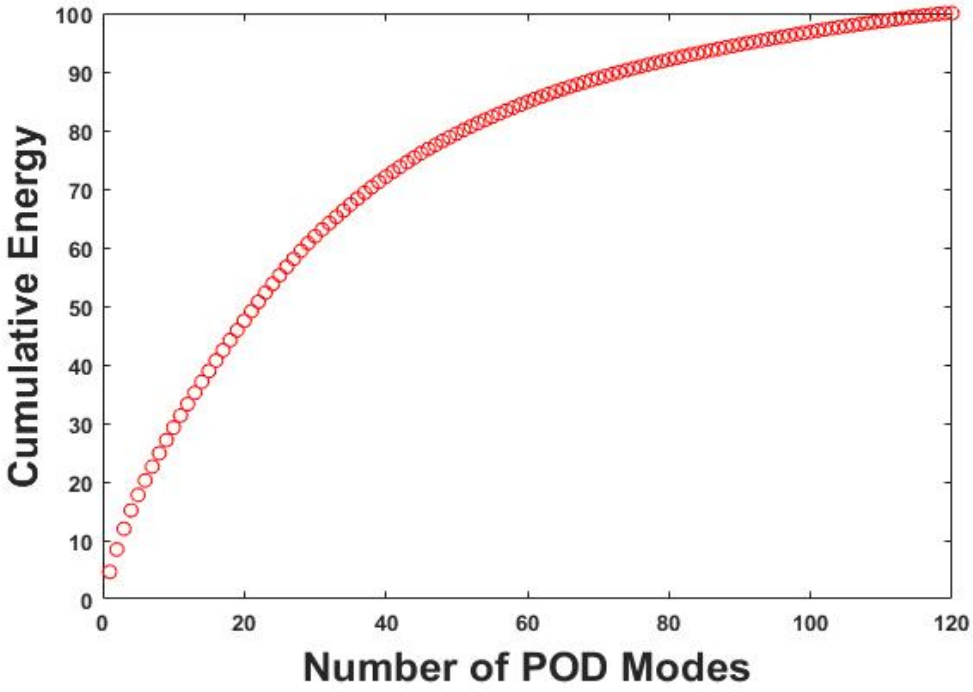

Figure 4. 14 Cumulative L-magnitudes of 120 POD modes using the Liutex vector (L_x, L_y, L_z)

Table 4. 6 Sum of L-magnitudes of the first 6 POD modes using Liutex vector (L_x, L_y, L_z) directly as an input

	Mode 1	Mode 2	Mode 3	Mode 4	Mode 5	Mode 6
L-magnitudes	4.629	3.809	3.523	3.17	2.64	2.46

Mode 1 has the highest L-magnitudes out of all to 120 POD modes. The low order POD modes have higher L-magnitudes than high order ones.

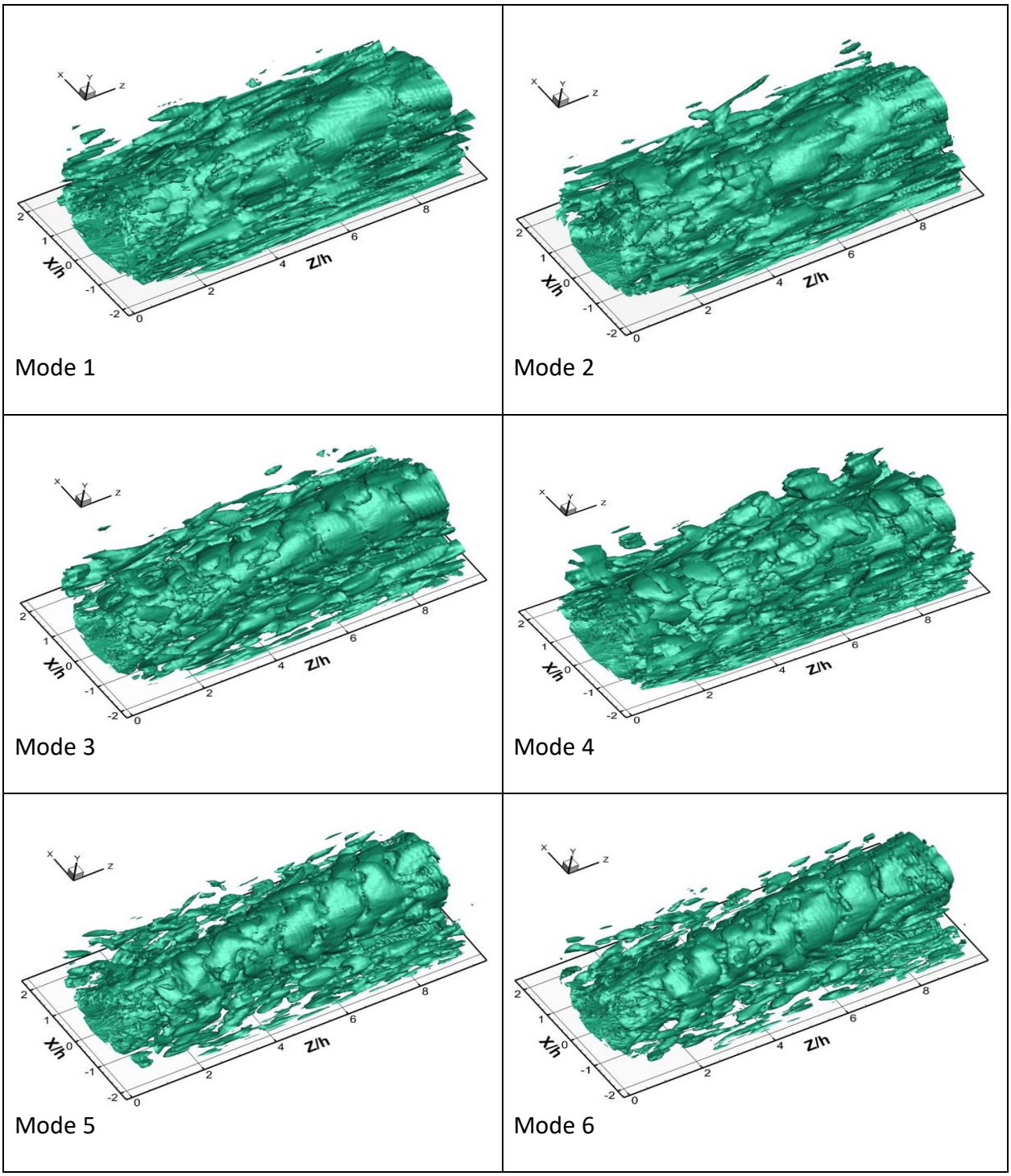

Figure 4. 15 Vortex structures (iso-surface of Liutex =0.05) of the first 6 POD modes in the MVG wake using Liutex as an input.

The shape of the first 6 POD modes was clearly delineated by loading data directly from Liutex vector and by choosing iso-surfaces with a threshold of Liutex = 0.05. The structures of low order modes are larger than the structures of high order modes, which means the mode's amount of L-magnitude is positively correlated to its structure size. For example, mode 1 has the highest L-magnitude (about 4.629% total L-magnitudes) and also has the largest shape compared to modes 2-3-4-5-6. Mode 2 contains about 3.809% of the total L-magnitudes which has the shape bigger than mode 3-4-5-6. The shape of mode 3, which contains approximately 3.523 % of the total L-magnitudes, has larger shape than modes 4-5-6. As the POD mode gets higher, the total L-magnitudes of the POD modes are decreasing and the shape of the POD mode gets smaller. Therefore, we can conclude that the absolute strength of rotation, or Liutex, is correlated with cumulative strength of rotation. The mode L-magnitude is closely correlated with the rotation strength if Liutex is used as the input data [51].

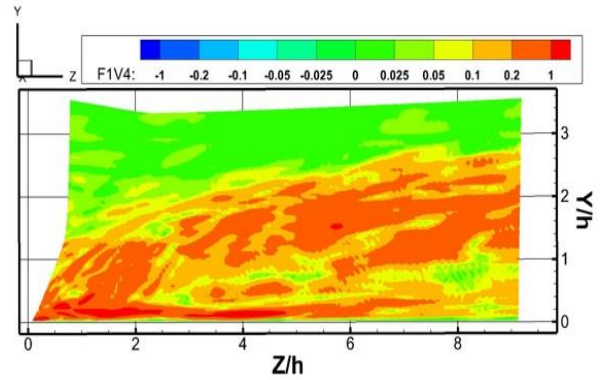

Mode 1

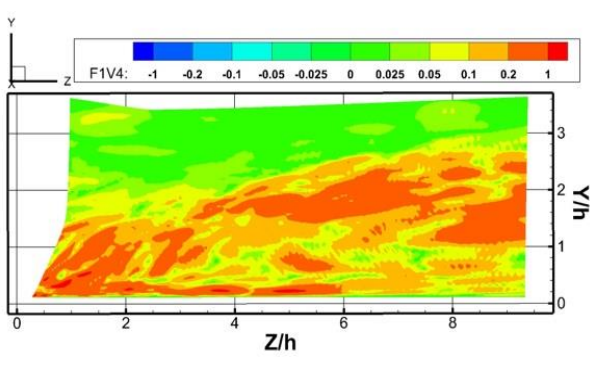

Mode 2

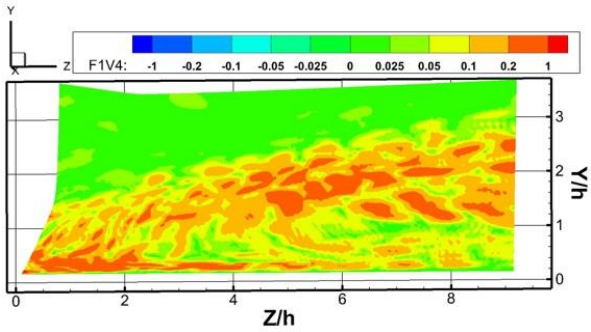

Mode 3

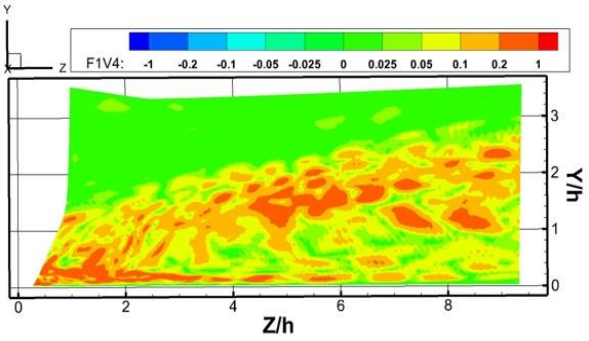

Mode 4

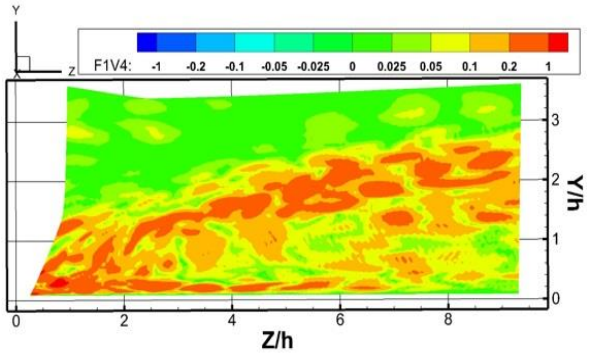

Mode 5

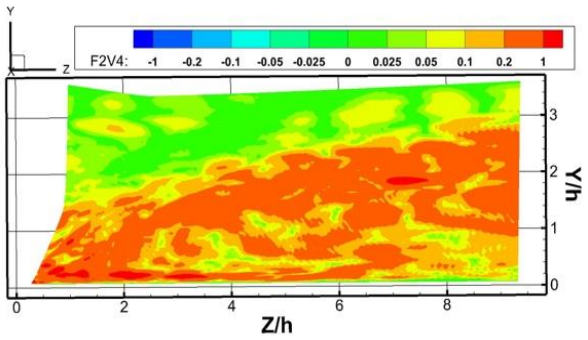

Mode 6

Figure 4. 16 The distribution of z component of Liutex on the central plane using Liutex as an input

From figure above we can clearly observe that modes 1-2 are streamwise vortices while modes 3-4 and modes 5-6 have characteristics of spanwise vortex structure. Modes 3-4 and modes 5-6 display staggered array structure like vortex street rolled from K-H instability, which is caused by the fluctuation motion induced by vortex rings. These findings are similar to the ones shown in the book [18]. There are six-time coefficients of POD modes and two-time coefficients are demonstrated in pairs such as modes 1-2, modes 3-4 and modes 5-6. All the three pairs have different fluctuation as shown in figure 4.17.

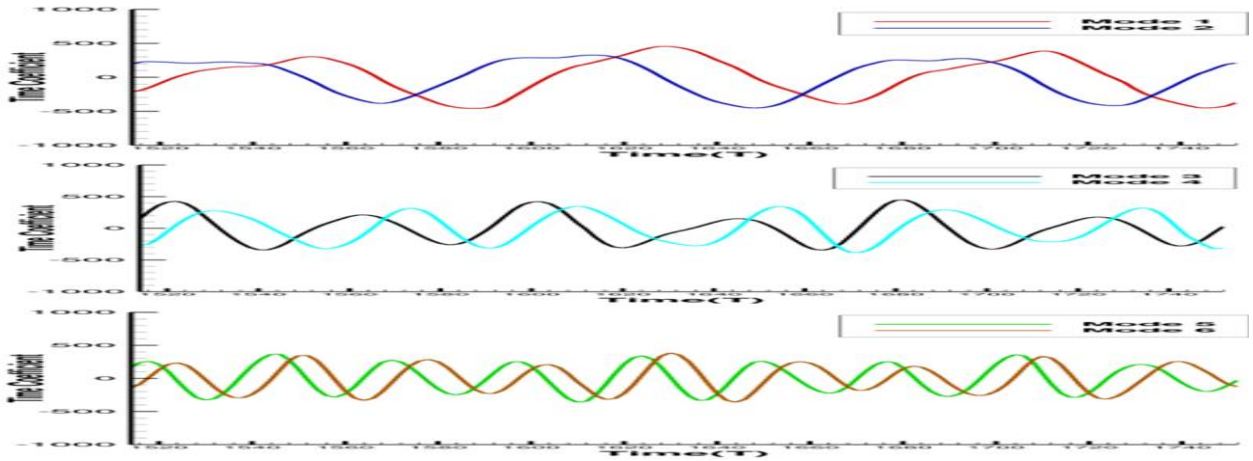

Figure 4. 17 Time coefficient of the first sixth POD modes

4.5 Liutex and proper orthogonal decomposition for coherence structure in the wake of micro vortex generator

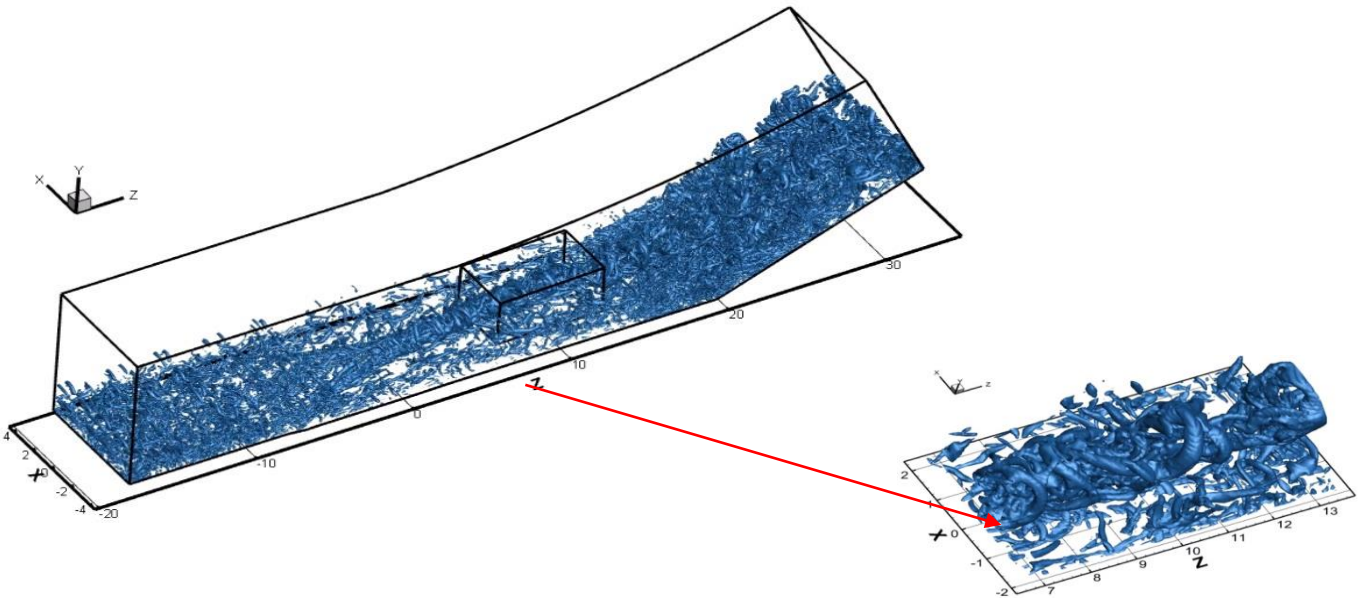

Figure 4. 18 Vortex Structure of Liutex in MVG wake

Table 4. 7 Parameters of subzone

	Start location	End location
x/h	-1.99	2.40
y/h	0	3.31
z/h	6.70	14.61

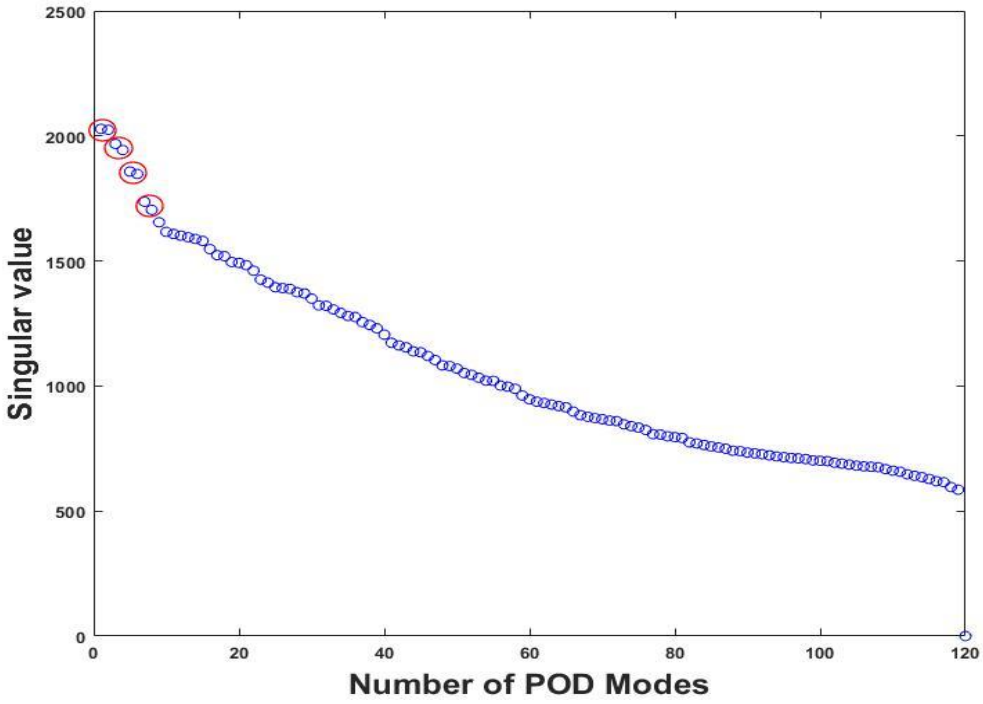

Figure 4. 19 Singular value of matrix X for 120 POD modes using Liutex vector $(L_x,\ L_y,\ L_z)$

The singular value of matrix X in figure 4.19 is shown in descending order and there are clearly four pairs of POD modes. Two POD modes with similar singular values as shown in table 2 are paired together. The first pair of POD modes is modes 1-2 with strong primary vortices. Second, third and fourth pairs of POD modes are modes 3-4, modes 5-6 and modes7-8, which are

secondary vortices generated by MVG. Pairing of the first 8 POD modes is obviously found, which is the sign of Kevin-Helmholtz instability. The observation of the mode pairing strongly supports the new mechanism of MVG for reduction of flow separation, which is the spanwise vortex ring generation by K-H instability.

Table 4. 8 Singular value of the first 8 POD modes using Liutex vector directly $(L_x,\ L_y,\ L_z)$ as an input

	Mode 1	Mode 2	Mode 3	Mode 4	Mode 5	Mode 6	Mode 7	Mode 8
Singular Value	2028	2024	1968	1943	1858	1848	1737	1704

Table 4. 9 Sum of L-magnitudes of the first 8 POD modes using Liutex vector directly $(L_x,\ L_y,\ L_z)$ as an input

	Mode 1	Mode 2	Mode 3	Mode 4	Mode 5	Mode 6	Mode 7	Mode 8
L-magnitudes	2.725	2.715	2.566	2.504	2.28	2.27	1.99	1.93

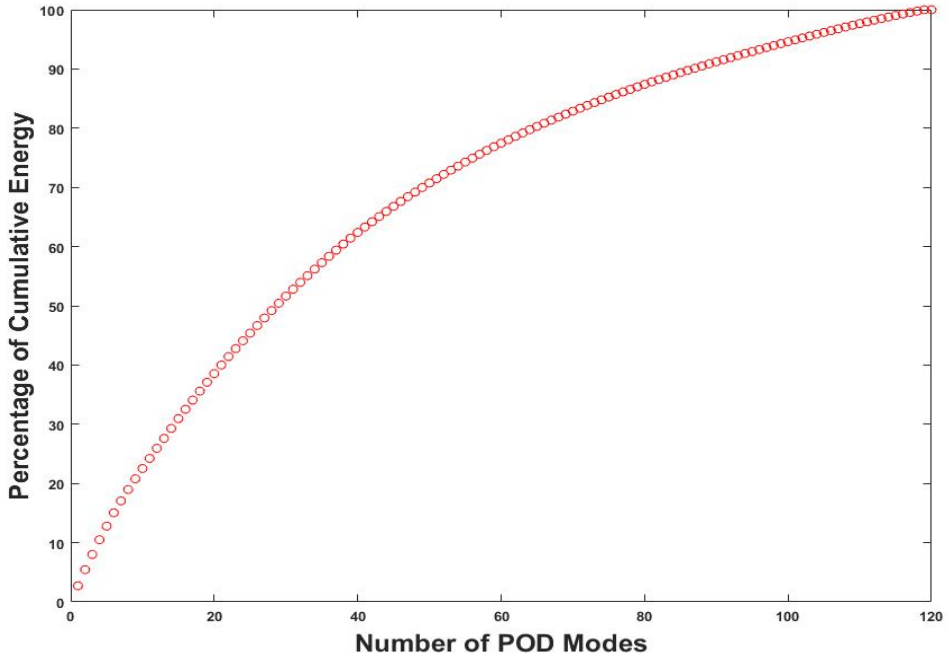

Figure 4. 20 Cumulative L-magnitudes of 120 POD modes using the Liutex vector $(L_x,\ L_y,\ L_z)$

In figure 4.20, mode 1 contains approximately 3% of total cumulative L-magnitudes, which is the highest L-magnitudes amount among all POD modes. The delta in percentage cumulative L-magnitudes between two consecutive POD modes is decreasing, which indicates that low order POD modes have more L-magnitudes than high order POD modes. The L-magnitudes of the first 8 POD modes is showed as table 4.9. It is showed in figure 4.21 that modes 1-2 and modes 5-6 are dominated by spanwise characteristics. Modes 3-4 and modes 7-8 are instead dominated by streamwise characteristics.

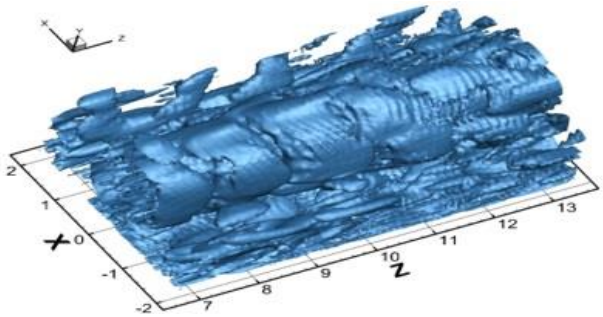

Mode 1

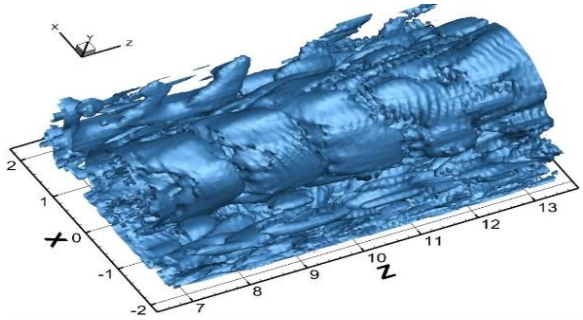

Mode 2

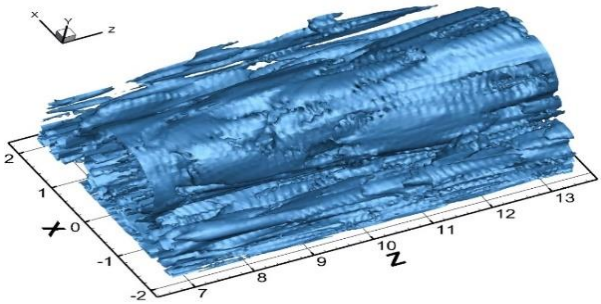

Mode 3

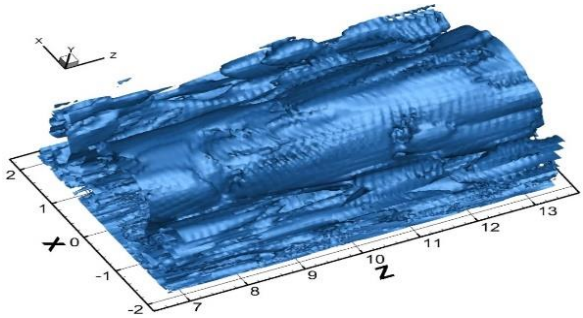

Mode 4

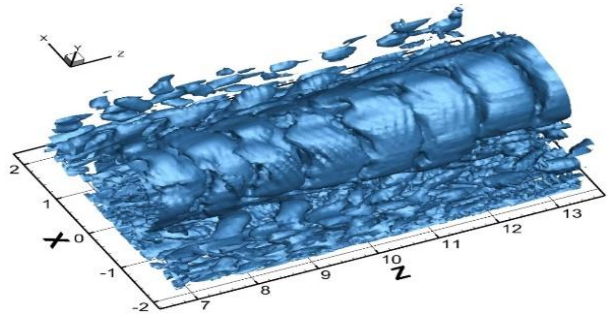

Mode 5

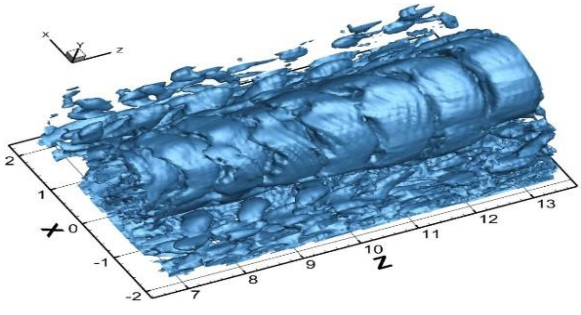

Mode 6

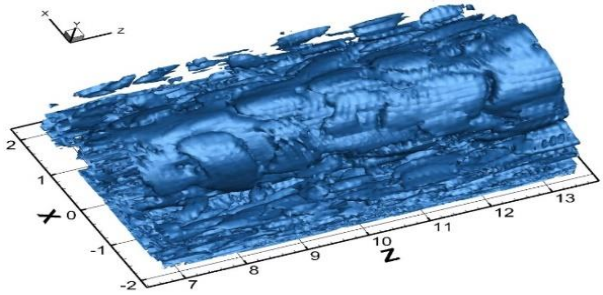

Mode 7

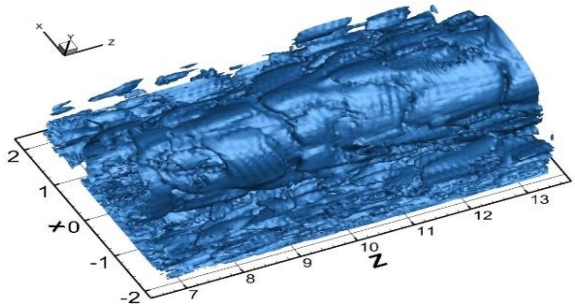

Mode 8

Figure 4. 21 Vortex structures (iso-surface of Liutex =0.05) of the first eight POD modes in the MVG wake

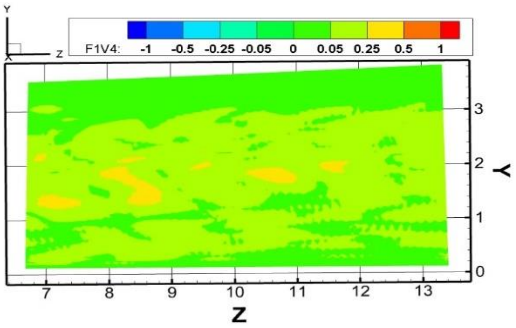

Mode 1

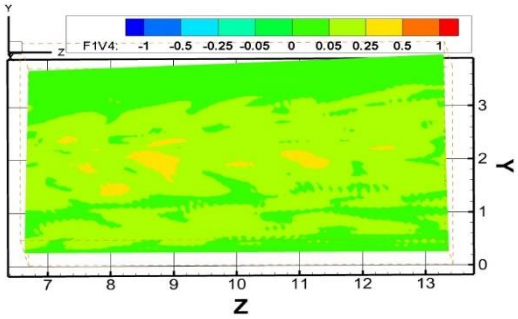

Mode 2

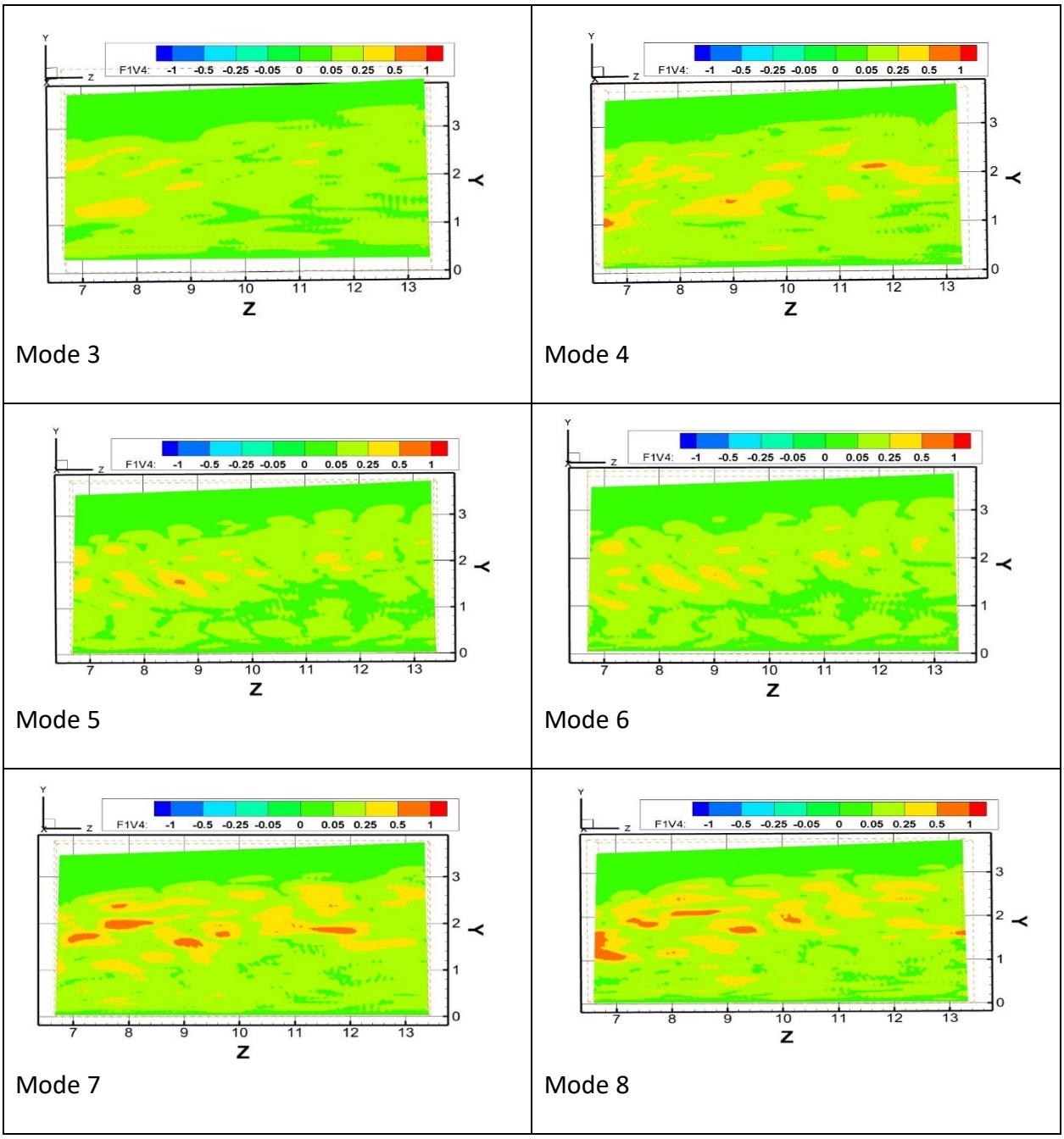

Figure 4. 22 The distribution of z component of Liutex on the central plane using Liutex as an input

In figure 4.22, modes 3-4-7-8 with characteristics of streamwise vortex structure have stronger vortex structures than modes 1-2-5-6, which are mainly dominated by spanwise vortex structures. Furthermore, modes 5-6 display staggered array structure like vortex street rolled

from K-H instability, which is caused by the fluctuation motion induced by vortex rings [9]. Figure 4.23 is shown clearly four pairs of time coefficient of POD modes. Modes 1-2, modes 3-4, modes 5-6 and modes 7-8 are paired in time coefficient. All four pairs of POD modes have different fluctuations.

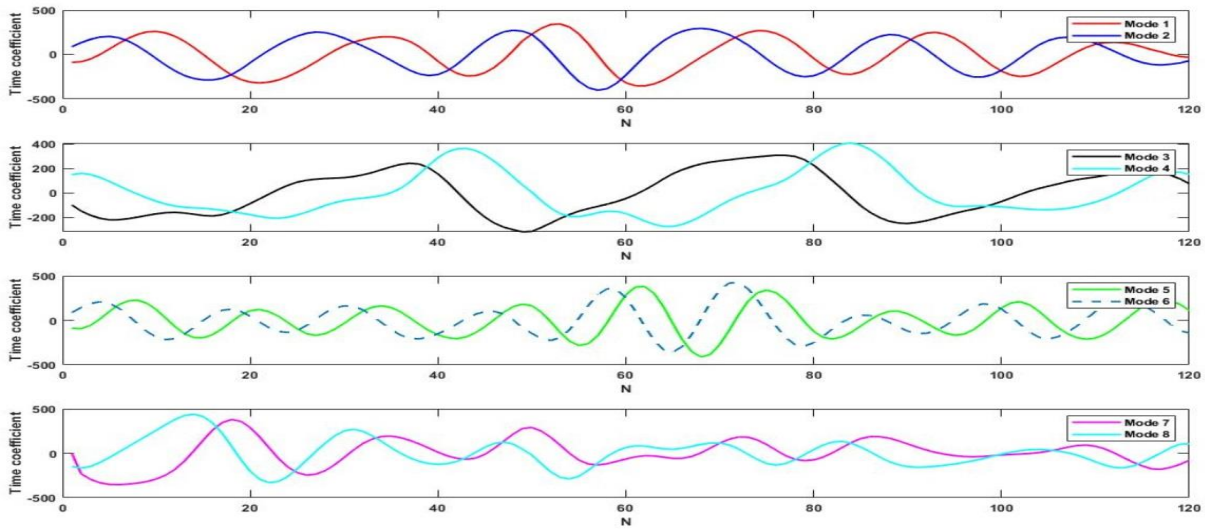

Figure 4. 23 Time coefficient of the first eight POD modes

Chapter 5
DMD

We collecting data for DMD architecture from a dynamic system:

$$\frac{d}{dt}x(t) = f(x(t), t; \mu) \tag{5.1}$$

Where $x(t) \in R^n$ is a vector representing the state of the dynamic system at time t,

μ contains parameter of system,

$f(.)$ Represents the dynamics,

Continuous time dynamics from (5.1) may induce a corresponding discrete-time dynamic:

$$\frac{x_{k+1}-x_k}{\Delta t} \approx f(x(t), t; \mu) \tag{5.2}$$

$$x_{k+1} = f(x(t), t; \mu) * \Delta t + \Delta t = F(x_k) \tag{5.3}$$

In most cases, it seems impossible to construct the solution of the governing nonlinear development (5.1). Due to technology's evolution, numerical solutions will help to solve that problem. We have $f(x(t), t; \mu)$ is unknown (5.1), so we use DMD framework to take equation-free perspective. The data measurement from this system is not used to estimate the dynamic but also to predict the future state. The DMD process is to build the locally representative linear dynamic system:

$$\frac{dx}{dt} = \mathcal{A}x \tag{5.4}$$

Where $\mathcal{A}$: the matrix in the continue time dynamics

$$\mathcal{A} = \Phi\Omega\Phi^{-1} \tag{5.5}$$

From (5.4) +(5.5)

$$\frac{dx}{dt} = \mathcal{A}x = \Phi\Omega\Phi^{-1}x \tag{5.6}$$

$$\Phi^{-1}\frac{dx}{dt} = \Phi^{-1}\Phi\Omega\Phi^{-1}x \tag{5.7}$$

$$\Phi^{-1}\frac{dx}{dt} = \Omega\Phi^{-1}x \tag{5.8}$$

$$\frac{d(\Phi^{-1}x)}{dt} = \Omega\Phi^{-1}x \tag{5.9}$$

We assume $$h = \Phi^{-1}x \tag{5.10}$$

From (5.9) + (5.10) $$\frac{dh}{dt} = \Omega h \tag{5.11}$$

From (5.11) we can get $$h_k = b_k e^{\omega_k t} \tag{5.12}$$

$$=> h = be^{\Omega t} = \Phi^{-1} x \tag{5.13}$$

$$=> b = \Phi^{-1} x(0) \tag{5.14}$$

$$=> x = \Phi e^{\Omega t} b = \Phi e^{\Omega t} \Phi^{-1} x(0) \tag{5.15}$$

$$x(t) = \sum_{k=1}^{n} \Phi_k e^{\omega_k t} b_k = \Phi e^{\Omega t} b \tag{5.16}$$

Where Φ_k:the eigenvectors of matrix $\mathcal{A}$

ω_k: the eigenvalues of matrix $\mathcal{A}$

b_k: the coefficient corresponding to coordinate of $x(0)$ in eigenvector basis.

We have $t_{k+1} = t_k + \Delta t$

$$x_{k+1} = \Phi e^{\Omega t_{k+1}} \Phi^{-1} x(0) \tag{5.17}$$

$$\Phi^{-1} x_{k+1} = \Phi^{-1} \Phi e^{\Omega t_{k+1}} \Phi^{-1} x(0)$$

$$\Phi^{-1} x_{k+1} = e^{\Omega t_{k+1}} \Phi^{-1} x(0)$$

$$e^{-\Omega t_{k+1}} \Phi^{-1} x_{k+1} = e^{-\Omega t_{k+1}} e^{\Omega t_{k+1}} \Phi^{-1} x(0)$$

$$=> e^{-\Omega t_{k+1}} \Phi^{-1} x_{k+1} = \Phi^{-1} x(0) \tag{5.18}$$

$$x_k = \Phi e^{\Omega t_k} \Phi^{-1} x(0) \tag{5.19}$$

$$\Phi^{-1} x_k = \Phi^{-1} \Phi e^{\Omega t_k} \Phi^{-1} x(0)$$

$$\Phi^{-1} x_k = e^{\Omega t_k} \Phi^{-1} x(0)$$

$$e^{-\Omega t_k} \Phi^{-1} x_k = e^{-\Omega t_k} e^{\Omega t_k} \Phi^{-1} x(0)$$

$$=> e^{-\Omega t_k} \Phi^{-1} x_k = \Phi^{-1} x(0) \tag{5.20}$$

From (5.16) $$=> x_{k+1} = \Phi e^{\Omega (t_k + \Delta t)} \Phi^{-1} x(0) \tag{5.21}$$

$$=> x_{k+1} = \Phi e^{\Omega t_k} e^{\Omega \Delta t} \Phi^{-1} x(0)$$

From (5.17) +(5.19) $$=> e^{-\Omega t_{k+1}} \Phi^{-1} x_{k+1} = e^{-\Omega t_k} \Phi^{-1} x_k = \Phi^{-1} x(0) \tag{5.22}$$

$$e^{-\Omega t_k} e^{-\Omega \Delta t} \Phi^{-1} x_{k+1} = e^{-\Omega t_k} \Phi^{-1} x_k \tag{5.23}$$

$$e^{\Omega t_k} e^{-\Omega t_k} e^{-\Omega \Delta t} \Phi^{-1} x_{k+1} = e^{\Omega t_k} e^{-\Omega t_k} \Phi^{-1} x_k$$

$$e^{-\Omega \Delta t} \Phi^{-1} x_{k+1} = \Phi^{-1} x_k$$

$$e^{\Omega \Delta t} e^{-\Omega \Delta t} \Phi^{-1} x_{k+1} = e^{\Omega \Delta t} \Phi^{-1} x_k$$

$$\Phi^{-1} x_{k+1} = e^{\Omega \Delta t} \Phi^{-1} x_k$$

$$\Phi \Phi^{-1} x_{k+1} = \Phi e^{\Omega \Delta t} \Phi^{-1} x_k$$

$$x_{k+1} = \Phi e^{\Omega \Delta t} \Phi^{-1} x_k \tag{5.24}$$

From (5.5) we have $\mathcal{A} = \Phi \Omega \Phi^{-1}$

$$=> e^{\mathcal{A} \Delta t} = \Phi e^{\Omega \Delta t} \Phi^{-1} \tag{5.25}$$

From (5.24) +(5.25) $$x_{k+1} = \Phi e^{\Omega \Delta t} \Phi^{-1} x_k = e^{\mathcal{A} \Delta t} x_k \tag{5.26}$$

We can use discrete time system to describe equation (5.4)

$$x_{k+1} = A x_k \tag{5.27}$$

Where $A = e^{\mathcal{A} \Delta t}$

We can use eigenvalue λ_k and eigenvector Φ_k of discrete time map A as the solution of this system:

$$x_k = \sum_{j=1}^{r} \Phi_j \lambda_j^k b_j = \Phi \Lambda^k b \tag{5.28}$$

Where b: the coefficients of the initial condition x_1 in eigenvector basis

$$=> x_1 = \Phi b \tag{5.29}$$

$$\|x_{k+1} - A x_k\|_2 \tag{5.30}$$

We will use two matrices with n-1 snapshots to minimize the error in equation (5.30)

$$X = \begin{bmatrix} | & | & | \\ x_1 & x_2 \dots & x_{m-1} \\ | & | & | \end{bmatrix}_{m \times (n-1)} \tag{5.31}$$

$$X' = \begin{bmatrix} | & | & | \\ x_2 & x_3 \dots & x_m \\ | & | & | \end{bmatrix}_{m \times (n-1)} \tag{5.32}$$

Instead of solving the linear approximation from equation (5.27), we will use data matrices to solve the problem:

$$X' \approx AX \tag{5.33}$$

Definition of Dynamic mode decomposition by Tu [52]

Suppose we have a dynamic system (5.1) and two sets of data,

$$X = \begin{bmatrix} | & | & | \\ x_1 & x_2 \dots & x_{m-1} \\ | & | & | \end{bmatrix}_{m \times (n-1)}, \tag{5.34}$$

$$X' = \begin{bmatrix} | & | & | \\ x'_1 & x'_2 \dots & x'_{m-1} \\ | & | & | \end{bmatrix}_{m\times(n-1)} , \quad (5.35)$$

So that $x'_k = F(x_k)$ where F is the map in (5.3) corresponding to the evolution of (5.1) for time Δt. DMD computes the leading eigen decomposition of the best-fit linear operator A relating the data $X' \approx AX$:

$$A = X'X^+ \quad (5.36)$$

The DMD modes, also called dynamic modes, are the eigenvectors of A, and each DMD mode corresponds to a particular eigenvalue of A.

First, we apply the singular value decomposition of X that we already proved preceding to find matrix $U, \sum, V$.

$$X \approx U\sum V^*$$

Where $U \in C^{m\times r}$: orthogonal matrix with $U^*U = I$

The left singular vectors U are POD modes

$V \in C^{n\times r}$: orthogonal matrix with $V^*V = I$

$\sum \in C^{r\times r}$: diagonal matrix with $\sigma_1 \geq \sigma_2 \geq \sigma_3 \geq \cdots \geq \sigma_r \geq 0$

r: the rank of the reduced SVD approximation to X, $r = \min(m, n)$

$*$: denotes the conjugate transpose

Second, we use equation (5.36) $A = X'X^+$ and equation (5.37) $X \approx U\sum V^*$ to get matrix A

$$X^+ = V\sum U^* \quad (5.38)$$

$$A = X'X^+ = X'V\sum{}^{-1}U^* \quad (5.39)$$

Where A is an $m \times m$ matrix which is too large matrix to compute. However, we will use $\tilde{A}$ is an $r \times r$ matrix which is the projection of the full matrix A onto POD modes:

From equation (5.33) $X' \approx AX$ and equation (5.37) $X \approx U\sum V^*$

$$X' \approx AX \approx AU\sum V^* \quad (5.40)$$

$$X'V \approx AU\sum V^* \ V$$

$$X'V \approx AU\sum I = AU\sum$$

$$X'V\sum{}^{-1} \approx AU\sum = AU\sum\sum{}^{-1}$$

$$X'V\sum{}^{-1} \approx AU\sum = AU\sum\sum{}^{-1} = AUI = AU$$

$$U^*X'V\sum{}^{-1} \approx U^*AU \quad (5.41)$$

We let $\widetilde{A} = U^{*}X'V\sum^{-1}$

$$\widetilde{A} = U^{*}AU \tag{5.42}$$

Where $\widetilde{A}(r \times r)$matrix is similar to matrix $A(m \times m)$, so $\widetilde{A}$ has the same eigenvalue of A.

We know $x_{k+1} = Ax_k(5.27)$, so the matrix $\widetilde{A}$ will define as a low dimension linear mode of the dynamic system on POD coordinate:

$$\tilde{x}_{k+1} = \widetilde{A}\tilde{x}_k \tag{5.43}$$

We can reconstruct easily the left singular vectors U of POD modes with high dimensional state:

$$x_k = U\tilde{x}_k \tag{5.44}$$

Third, we can find eigenvalue of $\widetilde{A}$:

$$\widetilde{A}W = W\Lambda \tag{5.45}$$

$$W = \begin{bmatrix} | & | & | \\ w_1 & w_2 \dots & w_m \\ | & | & | \end{bmatrix}_{r\times r},$$

Where W is a matrix eigenvectore of $\widetilde{A}$

$$\Lambda = \begin{bmatrix} \lambda_1 & 0 & \cdots & 0 \\ 0 & \lambda_1 & \dots & 0 \\ \vdots & \vdots & \ddots & \vdots \\ 0 & 0 & 0 & \lambda_r \end{bmatrix}_{r\times r},$$

Where Λ is a diagonal matrix which contains all the eigenvalues λ_i of matrix A and matrix $\widetilde{A}$

$$i = \{1,2,3 \dots, r\}$$

We can Λ and W to reconstruct the eigendecomposition of A.

In particular, Λ, Φ are eigenvalues and eigenvectors of A, respectively.

$$\Phi = X'V\sum^{-1}W \tag{5.46}$$

$$\Phi = \begin{bmatrix} | & | & | \\ \varphi_1 & \varphi_2 \dots & \varphi_m \\ | & | & | \end{bmatrix}_{m\times r}$$

Where φ_i are eigenvector of Φ, which are called DMD modes.

The Matrix reconstruction for DMD:

$$X \approx \Phi BC$$

$$X \approx \begin{bmatrix} | & | & | \\ \varphi_1 & \varphi_2 \cdots & \varphi_m \\ | & | & | \end{bmatrix}_{m\times r} \begin{bmatrix} b_1 & 0 & \cdots & 0 \\ 0 & b_2 & \cdots & 0 \\ \vdots & \vdots & \ddots & \vdots \\ 0 & 0 & 0 & b_r \end{bmatrix}_{r\times r} \begin{bmatrix} 1 & \lambda_1 & \lambda_1^2 \cdots & \lambda_1^{n-1} \\ 1 & \lambda_2 & \lambda_2^2 \cdots & \lambda_2^{n-1} \\ & \vdots & \vdots & \ddots & \vdots \\ 1 & \lambda_r & \lambda_r^2 & \lambda_r^{n-1} \end{bmatrix}_{r\times n}$$

Linear combination of DMD mode:

$$A\Phi = \Phi\Lambda$$

$$A\Phi\Phi^{-1} = \Phi\Lambda\Phi^{-1}$$

$$A = \Phi\Lambda\Phi^{-1}$$

$$x_{k+1} = \Phi\Lambda\Phi^{-1}x_k$$

$$x_{k+1} = \Phi\Lambda\Phi^{-1}\Phi\Lambda\Phi^{-1}x_{k-1} \quad (\Phi^{-1}\Phi = \Phi\Phi^{-1} = I)$$

$$x_{k+1} = \Phi\Lambda^2\Phi^{-1}x_{k-1}$$

$$x_{k+1} = \Phi\Lambda^2\Phi^{-1}\Phi\Lambda\Phi^{-1}x_{k-2}$$

$$x_{k+1} = \Phi\Lambda^3\Phi^{-1}x_{k-2}$$

$$\dots$$

$$x_{k+1} = \Phi\Lambda^k\Phi^{-1}x_1$$

$$x_{k+1} = (\Phi\Lambda\Phi^{-1})^k x_1$$

$$x_{k+1} = \Phi\Lambda^k\Phi^{-1}x_1$$

$$x_{k+1} = \Phi\Lambda^k b$$

Where $b = \Phi^{-1}x_1$ is called the initial DMD amplitude, x_1 is the first column of matrix X.

$$x_{k+1} \approx \sum_{k=1}^{r} \varphi_j \lambda_j^k b_j$$

$$x_{k+1} \approx \varphi_1\lambda_1^k b_1(mode1) + \varphi_2\lambda_2^k b_2(mode2) + \varphi_3\lambda_3^k b_3(mode3) + \cdots + \varphi_r\lambda_r^k b_r(mode\ r)$$

Where $\lambda_i = e^{\omega_i}$ with ω_i is a complex frequency in terms of pulsation,

Diagnostic from eigenvalues and eigenvectors of A:

a. We can predict the oscillation by plotting the real and imaginary part of eigenvalues of A with unit circle. Where the x-axis is the real part and y-axis is the imaginary part of eigenvalues λ_i.

- If the component is inside the unit circle: the mode decays.
- If the component is on the unit circle: the mode does not decay and does not grow.
- If the component is outside the unit circle: the mode is growing.

b. Growth rate: $\alpha_i = \log(|\lambda_i|)$

c. Frequency: Each mode has a unit frequency $\omega_i = \frac{arc(\lambda_i)}{2\pi}$

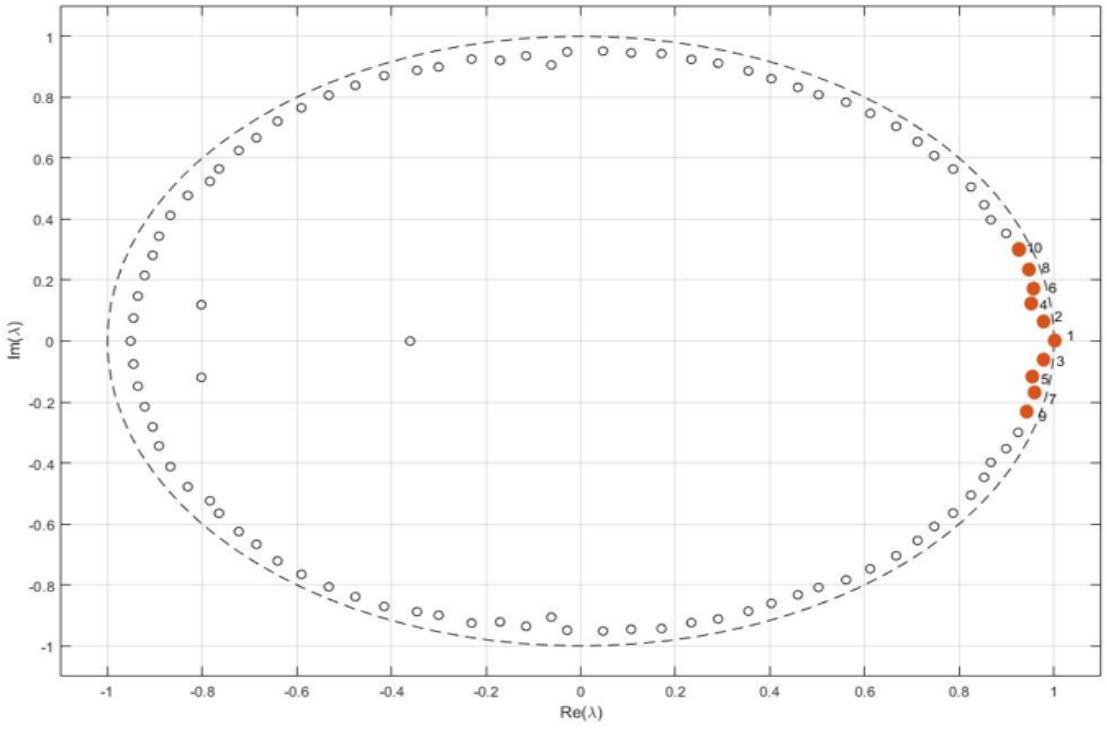

Figure 5. 1 DMD eigenvalues for all temporal modes in unit circle.

DMD mode 1	0.999679006912093 + 0.00000000000000i

DMD mode 2	0.979984567868930 + 0.0654720878552602i
DMD mode 3	0.979984567868930 - 0.0654720878552602i
DMD mode 4	0.954425053716561 + 0.122952093628034i
DMD mode 5	0.954425053716561 - 0.122952093628034i
DMD mode 6	0.955738474786543 + 0.164612622909996i
DMD mode 7	0.955738474786543 - 0.164612622909996i
DMD mode 8	0.945014806108991 + 0.234660477042197i
DMD mode 9	0.945014806108991 - 0.234660477042197i
DMD mode 10	0.924434019527715 + 0.299782658670692i

From the figure above, the unit circle is showed the real and imaginary part $\left(Re(\lambda_i), Im(\lambda_i)\right)$ of the first tenth eigenvalues. There is only mode 1 lying on the unit circle which shows it is kind of stable. The rest of the points lying inside the circle which show slow decay rates.

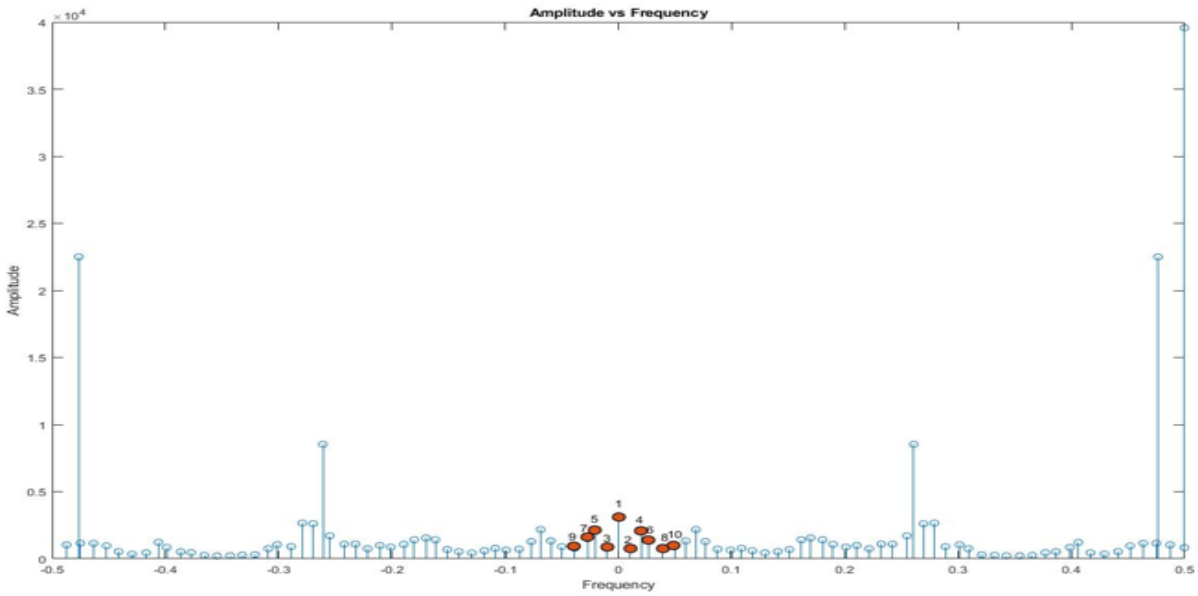

Figure 5. 2 Amplitude and frequency in each DMD mode

The positive and negative frequencies are shown in figure. Since mode 1 just has the real value and no imaginary value, mode 1 has zero frequency. Modes 3, 5,7,9 have the negative frequency which are computed from the complex conjugate of modes 2,4,6,8. Modes 3,5,7,9 have the same frequencies with modes 2,4,6,8, but they lie in opposite signs.

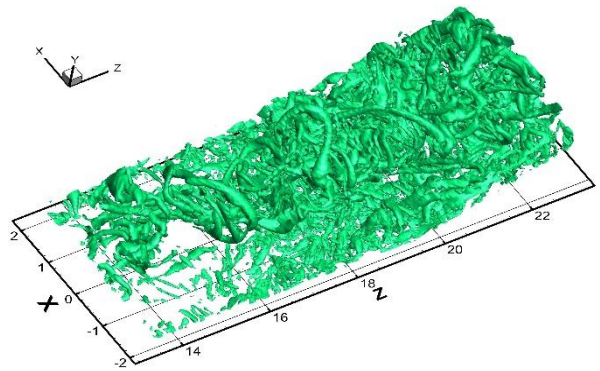

Mode 1

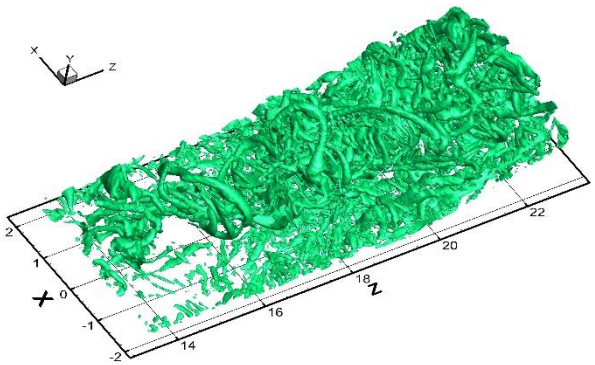

Mode 2

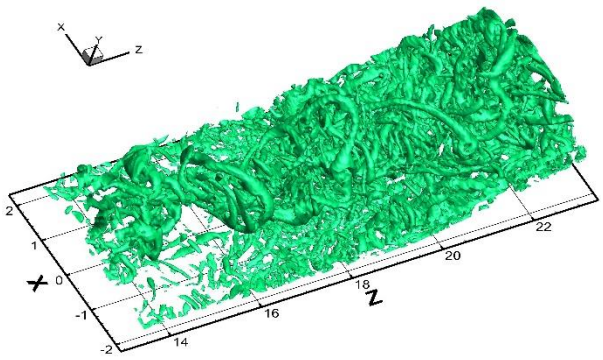

Mode 3

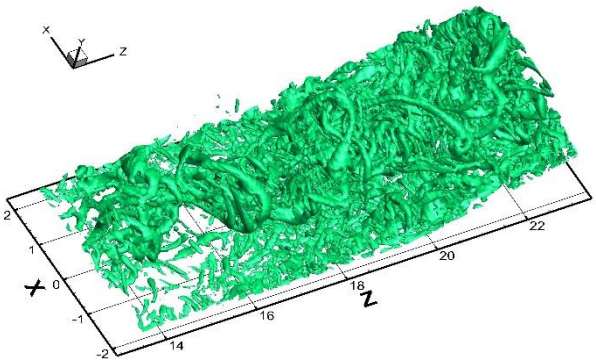

Mode 4

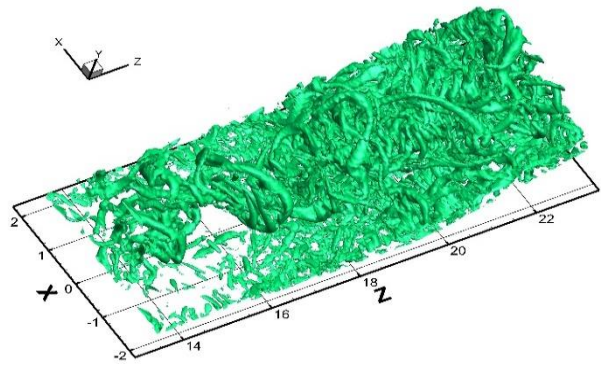

Mode 5

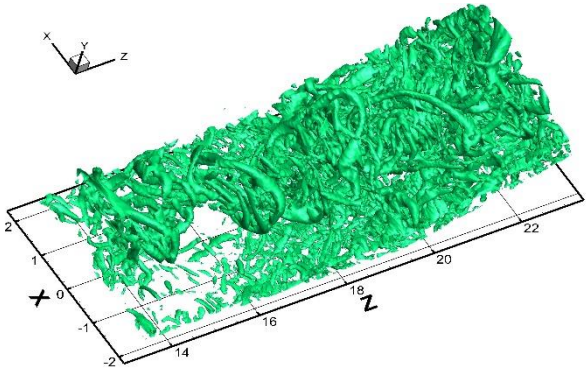

Mode 6

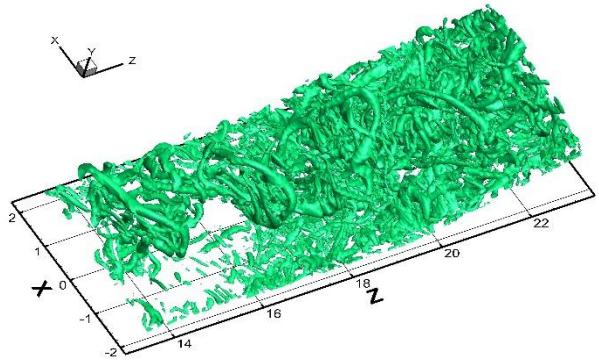

Mode 7

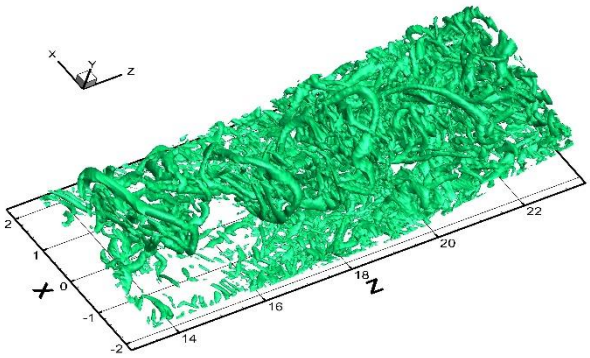

Mode 8

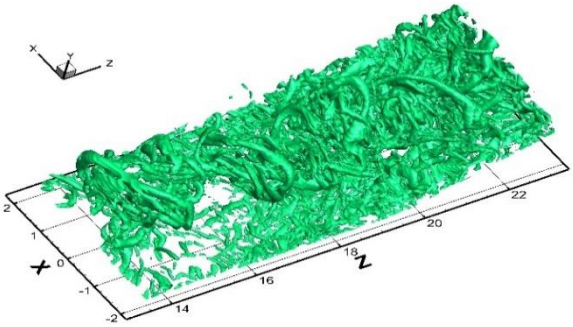

Mode 9

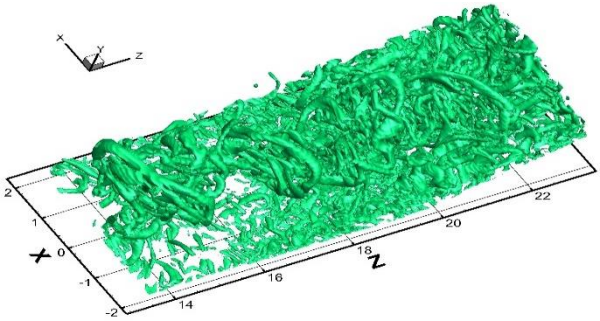

Mode 10

Figure 5. 3 Vortex structures (iso-surface of Liutex=0.05) of the first tenth DMD modes using Liutex as an input.

The DMD spatial modes are visualized by Liutex magnitudes which is showed in figures. Mode 1 has the smallest scale structure among the first ten modes and mode 10 has the largest

scale structure one. Structures of the mode are getting a little larger as the mode increasing. (The higher mode has larger scale structures than the lower one.)

Chapter 6
Conclusion

POD for coherent structure after the wake of MVG:

In conclusion, the POD method is applied to compare the results from loading data directly from Liutex vector (L_x, L_y, L_z) and loading from velocity (u, v, w) by using $\tilde{\Omega}_R$ method and Liutex iso-surface show that there are pairs of the first 6 POD modes over 120 snapshots, which is a strong sign of K-H type instability. This supports Li and Liu's theory discovered through numerical simulations that the mechanism of vortex ring generation should be K-H type instability and MVG generates vortex rings to destroy the shock. Although Babinsky's theory (the velocity profile getting fuller after applying MVG found through experimental method) has been well-known and his result was reconfirmed by many researchers, the theory that vortex after MVG is generated by the K-H type instability may provide a new perspective for further research. They may be two sides of one fact.

Besides, there are several results shown in table below by using velocity (u, v, w) as an input and using Liutex vector ($L_x,\ L_y,\ L_z$) as an input. The paring of the first 6 POD modes can be observed in both cases by the POD method and Liutex iso-surface.

1) Traditional POD decomposition with velocity input may meet difficulties in the case of low energy because the modes are ranked by fluid energy.
2) Since Liutex is a vector field featured to represent local fluid rotation, In the POD decomposition with Liutex input, the modes are ranked by the strength of fluid rotation.
3) POD using Input of Liutex vector can clearly show the main vortex structure after MVG.

4) Ranked by Liutex strength, the paring in strong modes is not found (Modes 1-2 are not paired), but the spanwise modes are clearly paired. Modes 1-2 look like mixture of streamwise and spanwise vortices.
5) Ranked by energy, the strong modes are all paired and dominant by streamwise vortices (Modes 1-2 in Figure 4.9).
6) Ranked by Liutex strength, although the streamwise modes are still strong like modes 1-2 which are dominant by the streamwise structure, the other modes like modes 3-4 and 5-6 are all spanwise structure dominant (Figure 4.15) and clearly paired.

Using Velocity (u, v, w) for $\tilde{\Omega}_R$/ Liutex as an Input	Using Liutex vector (L_x, L_y, L_z) as an Input
Mode 1 has the highest L-magnitudes among other POD modes. There are 3 pairs of POD modes: modes 1-2, modes 3-4 and modes 5-6. Moreover, pairing of POD modes is a common case, which is a sign of K-H type instability. Modes 1-2-5-6 are dominated by streamwise direction. However, modes 3-4 are mainly dominated by spanwise direction. There is no correlation between either the relative strength ($\tilde{\Omega}_R$) or absolute strength	Mode 1 has the highest L-magnitudes among other POD modes. There are 2 pairs of POD modes: modes 3-4 and modes 5-6. Moreover, pairing of POD modes is a common case, which is a sign of K-H type instability. Modes 1-2 are dominated by streamwise direction. However, modes 3-4-5-6 are strongly dominated by spanwise direction. The absolute strength of rotation, or Liutex, is correlated with cumulative L-magnitudes (of rotation).

(Liutex) of rotation, and cumulative L-magnitudes.	

POD for coherent structure in the wake of MVG:

There are eight pairs of POD modes found in an area of 120 snapshots by using Liutex vector (L_x, L_y, L_z) as an input, which is the sign of Kevin-Helmholtz instability. Mode 1 has the most energy compared to other POD modes. Modes 1-2 and modes 5-6 are mainly dominated by spanwise characteristics; on the other hand, modes 3-4 and modes 7-8 are dominated by streamwise characteristics. Pairing of POD modes strongly indicates the new mechanism of MVG for reduction of flow separation, which is due to the interaction between shocks and the spanwise vortex rings generated by K-H instability.

Further research compares the frequency at the shock area closed to the wall with and without MVG by applying DMD method. Thus, the mechanism of MVG for separation reduction by Li and Liu [32] is reconfirmed.

APPENDIX

MATLAB CODES for POD

```
filename = 'snapshotMatrix.txt';
A=load(filename);
save Asnapshots.mat A;
A=importdata('Asnapshots.mat');
perWant=input('How many percents you want(e.g. 89% you should input 89): ');
SumColumnA=sum(A,2);
Mean=SumColumnA/size(A,2);
 A_Without_Mean=zeros(size(A,1), size(A,2));
for i=1: size(A,2)
    A_Without_Mean(:,i)=A(:,i)-Mean;
end
[Ur,Sr,Vr]=svd(A_Without_Mean,'econ');
s=diag(Sr);
cumSa=cumsum(s);
cumS = cumSa/cumSa(end)*100;
cumSa2=cumsum(s.*s);
cumS2 = cumSa2/cumSa2(end)*100;
index=find(cumS>=perWant);
index2=find(cumS2>=perWant);
r=index(1);

figure (1)
plot(1:length(s),s,'bo','color', 'b')
xlabel('Number of POD Modes','color', 'r','FontSize', 18)
ylabel('Singular Value','color', 'r','FontSize', 18)
figure(2)
semilogy(1:length(s),s,'bo','color', 'b')
xlabel('Mode number','color', 'r','FontSize', 18)
ylabel('Singular value, log(\sigma_{j})','color', 'r','FontSize', 18)
figure(3)
plot(1:length(cumS2),cumS2,'ro','color', 'b')
hold on
plot(index2(1),cumS2(index2(1)),'d', 'markerfacecolor', [ 1, 0, 0 ] );
text(index2(1)+0.5,cumS2(index2(1)),['\leftarrow Tot. ' num2str(index2(1)) ':
' num2str(cumS2(index2(1))) '%'] );
hold off
figure(4)
plot(1:length(cumS),cumS,'ro','color', 'b')
hold on
plot(index(1),cumS(index(1)),'d', 'markerfacecolor', [ 1, 0, 0 ] );
text(index(1)+0.5,cumS(index(1)),['\leftarrow Tot. ' num2str(index(1)) ': '
num2str(cumS(index(1))) '%'] );
title('Cumulative \sigma','color', 'r','FontSize', 20)
xlabel('Number of POD Modes','color', 'r','FontSize', 18)
ylabel('Cumulative \sigma','color', 'r','FontSize', 18)
hold off
```

References

[1] H. Helmholtz, Über Integrale der hydrodynamischen Gleichungen, welche den Wirbelbewegungen entsprechen, Journal fur die reine und angewandte Mathematik. 55 (1858) 25-55.

[2] C. Liu, Y. Gao, X. Dong et al., Third generation of vortex identification methods: Omega and liutex/rortex based systems, J. Hydrodyn. 31 (2019) 205.

[3] C. Liu, Y. Gao, S. Tian et al., Rortex-A new vortex vector definition and vorticity tensor and vector decompositions, P. Fluids. 30(3) (2018) 035103.

[4] C. Liu, Y. Wang, Y. Yang et al., New omega vortex identification method, Science China Physics, Mechanics and Astronomy. 59(8) (2016) 684711.

[5] J. Liu, C. Liu., Modified normalized Rortex/vortex identification method, P. Fluid, 31(6), (2019) 061704.

[6] X. Dong, Y. Gao, C. Liu., New normalized Rortex/vortex identification method, P. Fluid. 31(1) (2019) 011701.

[7] Y. Gao, C. Liu., Rortex and comparison with eigenvalue-based vortex identification criteria, P. Fluid, 30, (2018) 085107.

[8] Y. Wang, Y. Gao, J. Liu, C.Liu, Explicit formula for the Liutex vector and Physical meaning of vorticity based on the Liutex-shear decomposition, J. Hydrodynamics. 31 (3) (2019) 464-474.

[9] C. Liu, Q. Li, Y. Yan, Y. Yan, G Yang, X. Dong, High order large eddy simulation for shock-boundary layer interaction control by a micro-ramp vortex generation, Frontier in Aerospace Science. 2 (2018).

[10] J. L. Lumley (1967). The structure of inhomogeneous turbulent flows. In Atmospheric Turbulence and Radio Wave Propagation (A.M. Yaglom and V.I. Takarski, eds.), pp. 166–178. Moscow: Nauka.

[11] C. Liu, Y. Gao, X. Dong et al., Third generation of vortex identification methods: Omega and liutex/rortex based systems, J. Hydrodyn. 31 (2019) 205.

[12] M. Love, Probabifity Theory, Van Nostrand, Princeton, NJ, (1955).

[13] LT. Jolliffe, Principle Component Analysis, Springer-Verlag, New York, (1986).

[14] R.C. Gonzalez and P.A. Wintz, Digital Image Processing, Addison-Wesley, Reading, MA, (1987).

[15] Y. C. Liang, W. Z. Lin, H. P. Lee, S. P. Lim, K. H. Lee, and H. Sun, 'Proper orthogonal decomposition and its applications, Part II: Model reduction for MEMS dynamical analysis', Journal of Sound and Vibration 256, 2002, 515– 532.

[16] Y. C. Liang, H. P. Lee, S. P. Lim, W. Z. Lin, K. H. Lee, and C. G. Wu, 'Proper orthogonal decomposition and its applications, Part I: Theory', Journal of Sound and Vibration 252, 2002, 527–544.

[17] C. G. Wu, Y. C. Liang, W. Z. Lin, H. P. Lee, and S. P. Lim, A note on equivalence of proper orthogonal decomposition methods, J. Sound and Vibration 265 (2003) 1103–1110.

[18] K. Taira, Proper orthogonal decomposition in fluid flow analysis: 1. Introduction, J. Japan Soc. Fluid Mech. (Nagare). 30 (2011) 115–123.

[19] G. Kerschen, J.C. Golinval, A.F. Vakakis, L.A. Bergman, The method of proper orthogonal decomposition for dynamical characterization and order reduction of mechanical systems: an overview, Nonlinear Dynamics 41 (2005) 147–170 (Section 7.4)

[20] W. Brewis, M. Garcia-Villalba, Shallow-flow visualization analysis by proper orthogonal decomposition, J. Hydraul Research. 49(5), 2011, 586-594.

[21] H. Chen, L.D. Reuss, LS. D. Hung and V. Sick V, A practical guide for using proper orthogonal decomposition in engine research, International Journal of Engine Research. 14(4) (2012) 307–319.

[22] G. Riches, R. Martinuzzi, and C. Morton, Proper orthogonal decomposition analysis of a circular cylinder undergoing vortex-induced vibrations, Physic of Fluids 30, 105103 (2018).

[23] P. Zhao, Y. Chen, G. Dong et al., Proper orthogonal decomposition analysis on longitudinal streaks in channel flow laden with micro-bubbles, The Japan Society of Fluid Mechanics. 51(2019).

[24] P. Schmid, O. Pust, Applications of the dynamic mode decomposition, Theoretical and Computational Fluid Dynamics. 25(1):249-259

[25] A. Seena, H.J.Sung, Dynamic mode decomposition of turbulent cavity flows for self-sustained oscillations. Int. J. Heat Fluid Flow 32(2011) 1098-1110.

[26] J. Sesterhenn, A.Shahirpour, A characteristic dynamic mode decomposition, Theoretical and Computational Fluid Dynamics. (2019) 33:281–305

[27] H. Babinsky, Y. Li, and C. W. P. Ford, Microramp control of supersonic oblique shock-wave/boundary-layer interactions, AIAA J. 47 (3) (2009) 668–675.

[28] S. Ghosh, J.I. Choi, and J. R. Edwards, Numerical simulation of effects of micro vortex generators using immersed-boundary method, AIAA J. 48 (1) (2010) 92-103.

[29] S. Lee, E. Loth, N. J. Georgiadis, J. R. DeBonis, Effect of Mach number on flow past microramps, AIAA J. 49 (1) 97-110.

[30] B. Wang, W. Liu, Y. Zhao, X. Fan, C. Wang, Experimental investigation of the micro-ramp-based shock wave and turbulent boundary layer interaction control, J. Fluid. 24 (2012) 055110.

[31] Q. Li, C. Liu, LES for supersonic ramp flow control flow using MVG at M=2.5 and Re_θ=1440, AIAA Paper 2010-0592, 2010.

[32] Q. Li, C. Liu, Implicit LES for supersonic microramp vortex generator: new discoveries and new mechanisms, Modeling and Simulation in Engineering. 10 (1155) (2011) 934982.

[33] F. Lu, Q. Li, and C. Liu, Micro Vortex Generators in High-Speed Flow, J. Progress in Aerospace Science. 53 (2012) 30–45.

[34] Y. Yan, Q. Li, C. Liu, F. K. Lu, Numerical, experimental and theoretical studies on mechanism of K-H instability and ring generation behind supersonic MVG, AIAA Paper 2011-676, 2011.

[35] Y. Yan, C. Chen, X. Wang, C. Liu, LES and analysis on the vortex structure behind supersonic MVG with turbulent inflow, Applied Math. Modelling. 38 (2014) 196-211.

[36] Z. Sun, Micro Vortex Generators for Boundary Layer Control: Principles and Applications, International J. Flow Control. 7 (2015) 67–86.

[37] Q. Li, P. Lu, C. Liu, A. Pierce and F. P. Lu, Numerical discovery and experimental validation of vortex ring generation by microramp vortex generator, The 28th International Symposium on Shock Waves, Springer Berlin Heidelberg. 403-408, 2012.

[38] B. Wang, W. Liu, Y. Zhao, X. Fan, C. Wang, Experimental investigation of the micro-ramp based shock wave and turbulent boundary layer interaction control, J. Fluid. 24 (2012) 055110.

[39] A. Vujinovic, J. Rakovec, Kelvin-Helmholtz Instability, Univerza v Ljubljani Fakulteta za Matematiko in Fiziko, (2015)

[40] Z. Sun, F.F.J. Schrijer, B.W.Van Oudheusden, The three-dimensional flow organization past a micro-ramp in a supersonic boundary layer, P. Fluid. 24 (2012) 055105

[41] J. C. Lin, Review of Research on Low-Profile Vortex Generators to Control Boundary-Layer Separation, Progress in Aerospace Sciences, Vol. 38, No. 4–5, (2002), 389–420.

[42] J. Delery, Shock Wave/Turbulent Boundary Layer Interaction and its Control, Progress in Aerospace Sciences. 22 (4) (1985) 209–280.

[43] D. C. McCormick, Shock/Boundary-Layer Interaction Control with Vortex Generators and Passive Cavity, AIAA J. 31 (1) (1993) 91–96.

[44] J. C. R. Hunt, A. A. Wray, P. Moin. Eddies, stream, and convergence zones in turbulent flows. Center for Turbulent Research Report CTR-S88, 1988, 193-208.

[45] M. S. Chong, A. E. Perry. A general classification of threedimensional flow fields. Physics of Fluids A, 1990, 2(5): 765-777.

[46] J. Zhou, R. Adrian, S. Balachandar. et al. Mechanisms for generating coherent packets of hairpin vortices in channel flow [J]. Journal of Fluid Mechanics, 1999, 387: 353-396.

[47] J. Jeong, F. Hussain. On the identification of a vortex [J]. Journal of Fluid Mechanics, 1995, 285: 69-94.

[48] G. W. Steward, Early history of singular value decomposition, SIAM Review, volume 35, 1993, 551-566

[49] G. H. Golub, C. F. V. Loan, Matrix Computations (Fourth Edition), 2013

[50] J. P. Meijaard, Computer methods in applied mechanics and engineering, volume 101, 1993, 161-173

[51] X. Trieu, Y. Yan, and C. Liu, “Liutex and proper orthogonal decomposition for coherence structure in the wake of micro vortex generator,” Liutex and Third Generation of Vortex Definition and Identification, edited by C. Liu and Y. Wang, CHAOS2020, 227.

[52] J. H. Tu, C. W. Rowley, D. M. Luchtenburg, S.L. Brunton, and J.N. KutzOn Dynamic Mode Decomposition: Theory and applications, Jounal of Computational Dynamics, 1(2): 391-421-2014.

Biographical Information

Xuan Trieu was born in Ho Chi Minh City, Vietnam. She used to work as a volunteer tutor at TCC Southeast campus in 2012 and at St. Ignatius of Loyola College Preparatory School in 2013. Xuan was awarded the Phi Theta Kappa Scholarship from 2011 to 2013, the Outstanding Transfer Scholar from 2011 to 2014 and the Pi Mu Epsilon from 2018 to present. In 2014, she obtained her B.S. in Mathematics and Education at University of Texas at Arlington. She later acquired a M.S. in Statistics at University of Texas at Arlington in 2019. Her research interests are in statistics, its applications to stock markets, computational mathematics, numerical method, and its applications to Computational Fluid Dynamics (CFD).